

**MECHANOCHEMICAL SYNTHESIS OF ZINC FERRITE AS A  
FUNCTION OF BALL TO POWDER RATIO (BPR)**

By

**Jari Cabarcas Bolivar**

A thesis submitted in partial fulfillment of the requirements for the degree of

**MASTER OF SCIENCE**

In

**Physics**

**UNIVERSITY OF PUERTORICO  
MAYAGÜEZ CAMPUS  
2013**

Approved by:

\_\_\_\_\_  
Oswald Uwakweh, Ph D  
President of the graduate Committee

\_\_\_\_\_  
Date

\_\_\_\_\_  
Henri Radovan, Ph D  
Member of the graduate Committee

\_\_\_\_\_  
Date

\_\_\_\_\_  
Jun-Qiang Lu, PhD  
Member of the graduate Committee

\_\_\_\_\_  
Date

\_\_\_\_\_  
Dorial Castellanos, PhD  
Header of Physics Department

\_\_\_\_\_  
Date

\_\_\_\_\_  
Ana Carmen González, M.s.  
Representative of the Office of Graduate Studies

\_\_\_\_\_  
Date

© Copyright by Jari R. Cabarcas Bolivar, 2013  
All Rights Reserved.

## ***ABSTRACT***

Mechanochemical reactions of ZnO, NiO, and  $\alpha$ -Fe<sub>2</sub>O<sub>3</sub> were carried out in a planetary mill to produce zinc ferrite (ZnFe<sub>2</sub>O<sub>4</sub>) and Ni<sub>x</sub>Zn<sub>1-x</sub>Fe<sub>2</sub>O<sub>4</sub> nanocrystallites. All measurement were made at room temperature under identical processing conditions entailing initial addition of 0.6 mL of acetone as surfactant with hardened stainless steel grinding materials. The average crystal sizes of the particles as determined from X-ray diffraction measurements decreased as a function of milling time, with values between 4.49 and 6.73nm. Specific Saturation Magnetization determined from Vibrating Sample magnetometer measurements varied with the milling time and reached a maximum value of 70.58 Am<sup>2</sup>/Kg (70.58 emu/g). From 2 mT, the coercivity displayed tendency to increase with increasing milling time for the end-member zinc ferrites phases (ZnFe<sub>2</sub>O<sub>4</sub>) for the three ball to powder ratios (BPR) used. Similar behavior was observed for the  $x = 0.25$  and  $0.75$  compositions corresponding to the general Ni<sub>x</sub>Zn<sub>1-x</sub> Fe<sub>2</sub>O<sub>4</sub> ferrites. Room temperature Mössbauer spectra of all samples exhibited non-magnetic peaks, which evolved from the sextets associated with the precursor hematite phase, and ultimately a total collapse of the sextets due to the relaxation effects linked to the superparamagnetic effect. The rate of the mechanochemical syntheses process depended on the BPR used. For all the compositions milled, the time to achieve the ZnFe<sub>2</sub>O<sub>4</sub> phase (for  $x = 0$ ) with BPR = 40:1 was shorter, in comparison to same composition ball milled with BPR of 20:1, and 10:1, respectively. However, for  $x = 0.25$ , the time to achieve the superparamagnetic behavior was shorter in comparison to the cases for  $x = 0.75$  and  $x = 0$  (end member) with BPR = 20:1. The superparamagnetic behavior was observed for all the ball milled compositions, for crystal sizes less than 10 nm.

## *Resumen*

Reacciones mecanoquímicas de ZnO, NiO y  $\alpha$ -Fe<sub>2</sub>O<sub>3</sub> fueron llevados a cabo en un molino planetario para producir nanocristales de ferrita de zinc (ZnFe<sub>2</sub>O<sub>4</sub>) y de Nickel-zinc (Ni<sub>x</sub>Zn<sub>1-x</sub>Fe<sub>2</sub>O<sub>4</sub>). Todas las medidas fueron hechas a temperatura ambiente bajo idénticas condiciones de procesamiento que implicaban la adición inicial de 0.6 ml de acetona como agente surfactante con materiales de molienda de acero inoxidable templado. Los tamaños de cristales medios de las partículas, tal como fueron determinados de las mediciones de difracción de rayos X disminuyeron en función del tiempo de molienda con valores entre 4.49 y 6.73 nm. La magnetización específica de saturación determinada de las medidas del Magnetómetro de Muestra Vibrante (VSM) varió con el tiempo de molienda y alcanzó un valor máximo de 70.58 Am<sup>2</sup>/Kg (70.58 emu/g). A partir de 2 mT, la coercitividad mostró una tendencia a incrementar con el incremento en el tiempo de molienda para las fases de ferritas de zinc del miembro final (ZnFe<sub>2</sub>O<sub>4</sub>) para las tres razones de bolas a polvo (BPR) usados. Comportamientos similares fueron observados para las composiciones  $x = 0.25$  and  $x = 0.75$  correspondiente a las ferritas generales **Ni<sub>x</sub>Zn<sub>1-x</sub>Fe<sub>2</sub>O<sub>4</sub>**. Los espectros de Mössbauer de todas las muestras exhibieron picos no magnéticos, los cuales evolucionaron a partir de los sextetos asociados a la fase precursora de hematite, y en última instancia a un colapso total de los sextetos debido a los efectos de relajación relacionados con el efecto superparamagnetico. La velocidad del proceso de las síntesis mecanoquímicas dependió del BPR usado. Para todas las composiciones molidas por bolas, el tiempo para alcanzar la fase de ZnFe<sub>2</sub>O<sub>4</sub> (para  $x = 0$ ) con BPR = 40:1 fue más corto en comparación a las mismas composiciones molidas por bolas con BPR de 20:1, y 10:1, respectivamente. Sin embargo, para  $x = 0.25$ , el tiempo para alcanzar el comportamiento superparamagnetico fue más corto en comparación con los casos  $x = 0.75$  y  $x = 0$  (miembro

extremo), ambos con BPR = 20:1. El comportamiento superparamagnético fue observado para todas las composiciones molidas por bolas, para tamaños de cristales menores a 10 nm.

## ***Dedication***

To my daughter ***Sharimar*** given that in course of realizing this accomplishment, I was not available to observe your developmental stages in the womb of your mother, and your first year early growth. It has been a hard time for me even as I write these words of acknowledgment because, I simply cannot stop thinking about how much I love you, and how much I miss you: I miss you darling daughter!

To Karen by take care in the first years of life of Sharimar, our beautiful daughter. I only hope that someday you can understand all my effort.

To my parents: ***Fanny*** and ***Rafael*** for their unconditional support, inspiration and love.

To my Brothers ***Yovanny***, ***Bladimir***, and my sister ***Katherine*** in staying together despite the distance and the adversities

To my nephew ***Bleidumar***, and my niece ***Ashley***

## *Acknowledgements*

First, I want to thank to **God** for his love and the grace He granted me to achieve this milestone in life.

I want to give thanks to the University of Puerto Rico, Mayagüez campus, in granting me the opportunity for graduate studies in Solid State Physics.

Thank you to my advisor, **Dr. Oswald N. C. Uwakweh**, for his advices and motivation, who was always willing to guide me along the entire process in addition to all the things, that taught me a great lesson in life.

Dr. Jun-Qiang Lu for the correction in the redaction of this work.

**Dr. Henri Radovan**, who in the time shared as his student, showed me that he is a good professor and a great person.

**Dr. Oscar Perales**, for granting me the opportunity to work in his laboratory. I also would like to thank Mr. **Boris Renteria** for his valuable collaboration in respect to both VSM and XRD measurements.

To Marcia Balaguera Gelves for her unconditional support.

To my friend and research partner **Ermides Chavez Baldovino** for his help and in forming a large research team.

To the families Palacio Gutierrez, Acosta Palacio, Escobar Palacio, for help me to reach this goal, and their unconditional support

To my aunts Aydee, and Belen and all my family.

## *Table of content*

<i>ABSTRACT</i> .....	iii
<i>Resumen</i> .....	iv
<i>Acknowledgements</i> .....	vii
<i>Table of content</i> .....	viii
1. INTRODUCTION .....	1
• Ferrofluids:.....	3
• Biomedical applications:.....	4
• Catalyst: .....	5
1.1. Aim of study.....	7
1.2. Literature Review .....	7
2. THEORETICAL BACKGROUND .....	13
2.1. Magnetism and Magnetic materials .....	13
2.1.2. Paramagnetism .....	14
2.1.3. Ferromagnetism and Antiferromagnetism .....	17
2.1.4. Ferrimagnetism .....	21
2.2. Magnetic domains .....	23
2.3. Anisotropy energy .....	24
2.4. Single domains .....	26
2.4.1. Origin of single domains.....	27
2.5. Saturation Magnetization .....	28
2.6. Coercivity .....	29
2.7. Ferrites.....	33

2.7.1.	Structure of cubic ferrites.....	34
2.8.	Superparamagnetism .....	37
3.	EXPERIMENTAL PROCEDURES.....	39
3.1.	Sample preparation.....	39
3.2.	High Energy Ball Milling (HEBM) .....	40
3.3.	X-Ray Diffractometry .....	42
3.3.1.	Bragg's Law .....	43
3.3.2.	Crystal size.....	44
3.4.	Vibrating Sample Magnetometry (VSM) .....	46
3.5.	Mössbauer spectroscopy .....	48
3.5.1.	Natural Line Width .....	49
3.5.2.	Recoil Energy Loss .....	50
3.5.3.	Resonance and Resonance Fluorescence .....	51
3.5.4.	Doppler Broadening.....	53
3.5.5.	Recoil-free Emission of gamma ray .....	54
3.5.6.	Isomer shift .....	56
3.5.7.	Nuclear Zeeman Effect .....	56
3.5.8.	Quadrupole splitting.....	57
4.	MECHANOCHEMICAL SYNTHESIS OF ZnFe <sub>2</sub> O <sub>4</sub> AS A FUNCTION OF “BALL TO POWDER RATIO” (BPR) .....	58
4.1.	Mechanochemical synthesis of Zinc ferrite BPR=10:1 .....	58
4.1.1.	XRD measurements .....	58
4.1.2.	VSM measurements .....	64
4.1.3.	Mössbauer measurements .....	68

4.2.	Mechanochemical synthesis of Zinc ferrite BPR=20:1 .....	70
4.2.1.	XRD measurements .....	70
4.2.2.	VSM measurements to ZnFe <sub>2</sub> O <sub>4</sub> with BPR 20:1 .....	77
4.2.3.	Mössbauer measurements to ZnFe <sub>2</sub> O <sub>4</sub> with BPR 20:1 .....	80
4.3.	Mechanochemical synthesis of Zinc ferrite BPR = 40:1 .....	84
4.3.1.	XRD measurements .....	84
4.3.2.	VSM measurements .....	90
4.3.3.	Mössbauer measurements to ZnFe <sub>2</sub> O <sub>4</sub> .....	92
5.	Comparative study of the synthesis Ni <sub>x</sub> Zn <sub>1-x</sub> Fe <sub>2</sub> O <sub>4</sub> for x = 0.25, 0.75 and x = 0 (End member) .....	100
5.1.	Synthesis of Ni <sub>x</sub> Zn <sub>1-x</sub> Fe <sub>2</sub> O <sub>4</sub> for x = 0.25 .....	100
5.1.1.	XRD measurements .....	100
5.1.2.	VSM measurements .....	105
5.1.3.	Mössbauer measurements .....	108
5.2.	Synthesis of Ni <sub>x</sub> Zn <sub>1-x</sub> Fe <sub>2</sub> O <sub>4</sub> for x = 0.75 .....	111
5.2.1.	XRD measurements .....	111
5.2.2.	VSM measurements .....	115
5.2.3.	Mössbauer measurements .....	118
5.3.	General discussion .....	124
5.3.1.	XRD measurements .....	124
5.3.2.	VSM measurements .....	127
5.3.3.	Mössbauer measurements .....	129
6.	Conclusions .....	133
	References .....	135

## *Table lists*

Table 1: Crystallographic parameters of some spinel ferrites. N: Normal, I: Inverse and M: Intermediate [73]	36
Table 2: Parameter for the two decays from the first excited to the ground state in two isotopes of iron [86]	55
Table 3: Crystal size, strain and lattice parameter of zinc ferrite synthesized by HEBM with BPR=10:1	64
Table 4: Values for coercivity and magnetization as a function of milling time for zinc ferrite with BPR=10:1	67
Table 5: Crystal size, strain and lattice parameter of zinc ferrite synthesized by HEBM with BPR=20:1.	77
Table 6: Values for coercivity and magnetization as a function of milling time for zinc ferrite with BPR = 20:1	79
Table 7: Crystal size, strain and lattice parameter of zinc ferrite synthesized by HEBM with BPR=40:1.	89
Table 8: Values for coercivity and magnetization as a function of milling time for the synthesis of $ZnFe_2O_4$ with BPR = 40:1.	91
Table 9: Comparison of crystallite sizes obtained for $ZnFe_2O_4$ for different synthesis methods.	99
Table 10: Average lattice parameter “ $a$ ”, crystal size “ $d$ ” and average strain for $Ni_xZn_{1-x}Fe_2O_4$ with $x=0.25$ and BPR= 20:1	104
Table 11: Values for coercivity and magnetization as a function of milling time for the synthesis of $Ni_xZn_{1-x}Fe_2O_4$ with $x = 0.25$ and BPR= 20:1	107
Table 12: Average lattice parameter “ $a$ ”, crystal size “ $d$ ” and average strain for $Ni_xZn_{1-x}Fe_2O_4$ with $x=0.75$ and BPR = 20:1.	115
Table 13: Values for coercivity and magnetization as a function of milling time for $Ni_xZn_{1-x}Fe_2O_4$ with $x = 0.25$ and BPR = 20:1.	118
Table 14: Comparison of crystallite sizes obtained for $Ni_xZn_{1-x}Fe_2O_4$ for different synthesis methods	132

## *List of figures*

Figure 1: Mössbauer spectra of nanosize $ZnFe_2O_4$ particles at various temperatures. ....	11
Figure 2: (A) Energy level splitting for one electron in a magnetic field directed along the positive z axis. (B) Fractional populations of a two-level system in thermal equilibrium at temperature T in a magnetic field B [65].....	15
Figure 3: Different types of magnetic behaviors [32].....	20
Figure 4: Temperature dependence of magnetic properties of a typical ferrimagnetic ( $NiO \cdot Fe_2O_3$ ). Figure 4 (A) shows the fractional saturation magnetization per unit mass in the ferrimagnetic region and figure 4(B) shows the reciprocal susceptibility (per mole) in the paramagnetic region. The dashed curve in the left –hand figure is the corresponding data for metallic iron [73].....	22
Figure 5: Spin arrangements in a magnetite, $FeO \cdot Fe_2O_3$ showing how the moments of the $Fe^{3+}$ ions cancel out, leading only the moments of $Fe^{2+}$ [65]. ....	23
Figure 6: Schematic representation of magnetization process explained by magnetic domain [78] .....	24
Figure 7: Asymmetry of the overlap of electron distributions on neighboring ions provides one mechanism of magnetocrystalline anisotropy. The asymmetry is tied to the direction of the spin, so that a rotation of spin directions relative to the crystal axes changes the exchange energy and also changes the electrostatic interaction energy of the charge distribution on pairs of atoms, giving rise to anisotropy energy. In the figure, the energy in (A) is not the same as the energy of (B) [65].....	25
Figure 8: The structure of the Block wall separating domains. In iron the thickness of the transition region is about 300 lattice constants [65]. ....	26
Figure 9: Representation of Origin of domains [65].....	27
Figure 10: Representative magnetization curve, showing the dominant magnetization process in the different regions of the curve [65]. ....	31
Figure 11: Hysteresis loop, where $H$ is the magnetic field strength (Oe), and $M$ is the magnetization of the material ( $emu/g$ ) [32]. ....	31
Figure 12: surface magnetic free poles and resulting demagnetizing field [65].....	32
Figure 13: Environments crystallographic of A sites and B sites [65]. ....	34

Figure 14: Cation site preference energy for various transition metal ions in A or B sites [84] ..	35
Figure 15:( A) Fritch Pulverisette-4 with the two special made brasses cans . (B) Milling ball action on grinding [83].....	41
Figure 16: Ball-powder-ball collision of powder mixture during mechanical alloying [29].....	42
Figure 17 : Diffraction of X-rays from the planes in a crystal [84].....	43
Figure 18: Siemens D500 diffractometer, taking of [81].....	46
Figure 19: vibrating sample magnetometer (VSM) [78] .....	47
Figure 20: lakeshore 7400 series Vibrating Sample Magnetometer (VSM) taken from [81]. ....	48
Figure 21: scheme of resonance absorption[34] .....	52
Figure 22: relation of line width, transition energy and recoil energy. (A) Overlap (schematic) of emission and absorption lines in optical transitions. (B) Absence of overlap of emission and absorption lines in nuclear transitions involving atoms free to recoil [75].....	53
Figure 23: This Figure shows of left to right the energy levels diagram of the 14.4 KeV $3/2 \ 1/2$ iron-57 transition, split by the Zeeman effect, altered by the electric quadrupole interaction. Taken of [33].....	57
Figure 24: X-ray diffraction spectra of synthesis of $ZnFe_2O_4$ by ball milling of ZnO and $\alpha-Fe_2O_3$ as a function of time using a BPR of 10:1. ....	60
Figure 25: (A) Crystal size and lattice parameter of $ZnFe_2O_4$ formed as a function of time during the ball milling of NiO, ZnO and $\alpha-Fe_2O_3$ powder mixtures using a BPR of 10:1. (B) Evolution of crystal size of ZnO and $\alpha-Fe_2O_3$ as function of milling time during Zinc ferrite formation. ...	61
Figure 26: Strain as function of milling time to zinc ferrite synthesized by HEBM. ....	63
Figure 27: Hysteresis loop for the synthesis of Zinc ferrite with BPR=10:1. ....	66
Figure 28: Coercivity size and Specific magnetization as function of milling time to $Ni_xZn_{1-x}Fe_2O_4$ with $x=0$ , synthesized by HEBM and BPR=10:1. ....	67
Figure 29: Room temperature Mossbauer spectrum to zinc ferrite with BPR =10:1 .....	69
Figure 30: Relative abundance of hematite as a function of milling time during the synthesis of $ZnFe_2O_4$ using a BPR of 10:1 .....	70

Figure 31 : X-ray diffraction spectra of synthesis of $ZnFe_2O_4$ by ball milling of $ZnO$ and $\alpha-Fe_2O_3$ as a function of time using a BPR of 20:1. ....	72
Figure 32: (A) Crystal size and lattice parameter as function of milling time to zinc ferrite synthesized by HEBM and BPR=20:1. (B) Evolution of the crystal size for the precursors $ZnO$ , $\alpha-Fe_2O_3$ , and $ZnFe_2O_4$ as function of milling time. ....	75
Figure 33: Strain as function of milling time to zinc ferrite with BPR=20:1 and synthesized by HEBM. ....	76
Figure 34 : Hysteresis loop for synthesis of $ZnFe_2O_4$ with BPR= 20:1. ....	78
Figure 35: Coercivity size and Specific Magnetization as function of milling time for $Ni_xZn_{1-x}Fe_2O_4$ with $x=0$ , synthesized by HEBM and BPR=20:1 .....	79
Figure 36: Mössbauer spectra of $ZnFe_2O_4$ ball-milled $ZnO-\alpha-Fe_2O_3$ mixture to BPR=20:1 .....	82
Figure 37: Relative abundance of hematite as a function of milling time during the synthesis of $ZnFe_2O_4$ using a BPR of 20:1 .....	83
Figure 38: : X-ray diffraction spectra of synthesis of $ZnFe_2O_4$ by ball milling of $ZnO$ and $\alpha-Fe_2O_3$ as a function of time using a BPR of 40:1. ....	85
Figure 39: XRD spectrums for spinel phase. The time represent the hour of milling time necessary to reach the spinel phase. This fact is corroborated with Mossbauer measurement. ...	86
Figure 40: Evolution in the crystal size for Zinc ferrite for the different BPR: 10:1, 20:1 and 40:1 .....	88
Figure 41: Crystal size and lattice constant as function of milling time to zinc ferrite synthesized by HEBM and BPR = 40:1. ....	88
Figure 42: Strain as function of milling time for Zinc Ferrite with BPR = 40:1 and synthesized by HEBM. ....	89
Figure 43: Hysteresis loop for the synthesis of $ZnFe_2O_4$ with BPR= 40:1 .....	90
Figure 44: Coercivity size and magnetization as function of milling time for the synthesis of $Ni_xZn_{1-x}Fe_2O_4$ with $x=0$ ( $ZnFe_2O_4$ ), synthesized by HEBM and BPR = 40:1. ....	91
Figure 45: Mössbauer spectra of $ZnFe_2O_4$ ball-milled $ZnO-\alpha-Fe_2O_3$ mixture to BPR = 40:1 .....	95
Figure 46: Relative abundance of hematite as a function of milling time during the synthesis of $ZnFe_2O_4$ using a BPR of 40:1 .....	96

Figure 47: Mössbauer spectra for Zinc ferrite. Each doublet corresponds to synthesis with a distinct BPR, and, the time to obtain corresponding superparamagnetic state.....	98
Figure 48: XRD spectral measurements of mechano-chemical synthesis of $Ni_xZn_{1-x}Fe_2O_4$ , $x = 0.25$ and BPR = 20:1 in the range of 5-35h of milling time. ....	102
Figure 49: Crystal size and lattice parameter as function of milling time for the synthesis of $Ni_xZn_{1-x}Fe_2O_4$ with $x = 0.25$ and BPR = 20:1.....	103
Figure 50: Strain as function of milling time for $Ni_xZn_{1-x}Fe_2O_4$ with $x=0.25$ and BPR: 20:1 ...	104
Figure 51: Hysteresis loop for the synthesis of $Ni_xZn_{1-x}Fe_2O_4$ with $x = 0.25$ synthesized by HEBM and BPR=20:1. ....	106
Figure 52: Coercivity and Magnetization as function of milling time for $Ni_xZn_{1-x}Fe_2O_4$ with $x=0.25$ synthesized by HEBM and BPR=20:1 .....	107
Figure 53: Mössbauer measurements for $Ni_xZn_{1-x}Fe_2O_4$ with $x = 0.25$ synthesized by HEBM and BPR = 20:1.....	109
Figure 54: Relative abundance of hematite as a function of milling time during the synthesis of the solid solution of $Ni_xZn_{1-x}Fe_2O_4$ with $x = 0.25$ , using a BPR of 20:1 .....	110
Figure 55: XRD spectra for $Ni_xZn_{1-x}Fe_2O_4$ with $x = 0.75$ synthesized by HEBM with BPR=20:1 .....	112
Figure 56: Crystal size and lattice constant as function of milling time during the synthesis of the solid solution $Ni_xZn_{1-x}Fe_2O_4$ with $x=0.75$ synthesized by HEBM and BPR=20:1.....	113
Figure 57: Average strain as a function of milling time for $Ni_xZn_{1-x}Fe_2O_4$ with $x=0.75$ and BPR=20:1.....	114
Figure 58: Hysteresis loops associated with the synthesis of $Ni_xZn_{1-x}Fe_2O_4$ with $x = 0.75$ by HEBM using BPR = 20:1 .....	116
Figure 59: Coercivity and saturation magnetization as a function of milling time for $Ni_xZn_{1-x}Fe_2O_4$ with $x = 0.75$ synthesized by HEBM and BPR = 20:1. ....	117
Figure 60: Mössbauer spectra of $Ni_xZn_{1-x}Fe_2O_4$ with $x = 0.75$ , ball-milled ZnO- $\alpha$ - $Fe_2O_3$ mixture with BPR=20:1. ....	122
Figure 61: Relative abundance of hematite as a function of milling time during the synthesis of the solid solution of $Ni_xZn_{1-x}Fe_2O_4$ with $x = 0.75$ , using a BPR of 20:1 .....	123

Figure 62: XRD patterns for  $\text{Ni}_x\text{Zn}_{1-x}\text{Fe}_2\text{O}_4$ , BPR = 20:1 and  $x = 0$ ,  $x = 0.25$  and  $x = 0.75$ . ..... 125

Figure 63: The fig shows both, (A). Crystal as a function of milling time and, (B) Strain for the different concentrations, namely,  $x = 0$ , 0.25, and, 0.75 for the syntheses of  $\text{Ni}_x\text{Zn}_{1-x}\text{Fe}_2\text{O}_4$  and BPR=20:1..... 126

Figure 64: Coercivity variation as a function of milling time for composition of  $x = 0$ , 0.25 and 0.75, and BPR = 20:1 ..... 129

Figure 65: Mössbauer measurements at room temperatures for  $\text{Ni}_x\text{Zn}_{1-x}\text{Fe}_2\text{O}_4$  series, BPR=20:1 and concentrations of  $x=0$ ,  $x=0.25$  and  $x=0.75$ ..... 130

## 1. INTRODUCTION

Ferrites or ferros spinels are ceramic magnetic materials with the general formula  $MFe_2O_4$  (M: divalent metal cation) that are generally synthesized by using high temperature to achieve a chemical reaction between mixtures of oxide ( $\alpha\text{-Fe}_2\text{O}_3$ ) known as hematite, and other compounds such as carbonates or oxides that provide the divalent cation. The use of thoroughly mixed powdered materials that are fired at temperatures higher than  $500^\circ\text{C}$  under oxygen rich environments is what is typically known as sintering or high temperature ceramic synthesis method. The thoroughly mixed powdered materials are sometimes pressed into desired shapes before the high temperature firing to obtain magnets of desired shapes. The magnetizations obtained from the ferrites can be high enough to be of a commercial value, even though their magnetic saturations are not as high as those of ferromagnetic materials. The spinel structured ferrites or ferros spinel are therefore known as soft ferrites due to the fact that they exhibit low coercive force and correspondingly narrow hysteresis loops, and, other properties, such as high resistivity that, combined with the above characteristics, make them ideally suited for high-frequency applications in electronic equipment [1],[2] [64]. In general, soft ferrites exhibit Ferrimagnetic behavior because, there is a net magnetic moment due to two distinct magnetic sites, which have opposite and unequal moments.

There are different methods used in the synthesis of ferros spinel materials apart from the traditional ceramic route which entails the sintering of premixed precursor powder materials. Some notable examples of syntheses routes are: Hydrothermal [3], Sol-gel [4], Co-precipitation [5], [6],[7], Reverse Micelle [8], [9],[10], Combustion synthesis [11], Mechanochemical synthesis by mechanical milling or high energy ball milling [12] [13], [14],[15] Micro-emulsion and others [16], [17], [18], [19].

All the above methods have been used to synthesize different nanosized ferrites with well tuned physical and magnetic properties. Like any other synthesis process, there exist advantages and disadvantages for each type of synthesis route used in producing the nanoparticles. Side effects such as contamination effects, either from the precursor materials, or arising from partial or incomplete precursor material transformation during synthesis, can lead to loss of property or non-optimized properties of the materials. In the literature there exist a variety of experimental studies using high energy ball milling of appropriate precursor materials in a mechano-chemical synthesis process resulting in the production of nanoparticles of tin, cobalt, magnesium, nickel and zinc ferrites materials[20], [15], [21], [22], [12], [23]. In all cases, appropriate precursor materials were mixed together with or without chemicals, such as ethanol, toluene, (otherwise known as processing agents chemicals) that serve to facilitate the intricate mixing of the powdered materials during the milling process.

Within this group of ferrites known as ferrosphenel we find zinc ferrite, which is of interest in the fields of basic researches in magnetism and industries. Some applications in the field of industry are for gas sensor, absorbent material for hot-gas, desulphurization, and semiconductor photo catalyst applications. As all these applications depend on particle size, appropriate parameters and methods are chosen to get better or optimum results of relevant importance. We get zinc ferrite by mechanical-chemical synthesis; that is the general name given to the process of the milling of metal powders involving chemical reactions occurring during milling. The advantage of this technique is its feasibility for large-scale production as well as its simplicity and low cost. Although much work has been focused on this technique, few of them are directed towards synthesis of zinc ferrite nanoparticles[24], [25–28]. Below, we are going to see three of the most important applications of the ferrites, namely, ferrofluids, biosciences and catalysis.

- **Ferrofluids:**

A magnetic colloid, also known as a ferrofluid (FF), is a colloidal suspension of single-domain magnetic particles, with typical dimensions of about 10 nm, dispersed in a liquid carrier. The liquid carrier can be polar or non polar. Since the nineteen sixties, when these materials were initially synthesized, their technological applications did not stop to increase. There are essentially two methods used to prepare these nanoparticles, notably, by size reduction and chemical precipitation respectively. In the size reduction method, a magnetic powder of micron size is mixed with a solvent and a dispersant in a ball mill in order to grind for a period of several weeks [88]. In the chemical precipitation method, this is probably the most used method to prepare magnetic nanoparticles nowadays, co-precipitation which occurs with the mixture of appropriate compounds, followed by subjecting the system to different procedures such as peptization, magnetic separation, filtration, and finally dilution actions [88].

- **Surfacted ferrofluid:**

Surfacted ferrofluids are formed by magnetic nanoparticles particles (usually magnetite,  $\text{Fe}_3\text{O}_4$ ) coated with surfactant agents in order to prevent their aggregation. Steric repulsion between particles acts as a physical barrier that keeps grains in the solution and stabilizes the colloid. Surfacted ferrofluids are widely used in technological devices, being commercially available [88].

- **Ionic ferrofluids:**

In ionic ferrofluids, nanoparticles are electrically charged to keep the colloidal system stable. Magnetic particles (usually maghemite,  $\gamma\text{-Fe}_2\text{O}_3$ , and different ferrites,  $\text{MFe}_2\text{O}_4$ , where  $\text{M} = \text{Mn}, \text{Co}, \text{Zn}, \text{Cu}, \text{Ni}$ ) are obtained through a chemical precipitation method, and an acid-alkaline reaction between particles and the bulk keeps their surface electrically charged.

- **Biomedical applications:**

Magnetic materials in the form of nanoparticles, mainly magnetite ( $\text{Fe}_3\text{O}_4$ ), are present in various living organisms and can be used in a number of applications. Magnetic nanoparticles can, of course, be prepared in the laboratory by means of the well-known methods; however, magnetic biogenic particles have better properties than synthetic ones: they have a definite size range and width/length ratio and high chemical purity. They are almost perfect crystallographically, and sometimes they possess unusual crystallographic morphologies. Extracellular production of nanometer magnetite particles by various types of bacteria has been described. In many cases, the biogenic particles retain a lipid layer which makes them very stable and easily biocompatible.

Many biotechnological applications have been developed based on biogenic and synthetic magnetic micro- and nanoparticles [87]. Magnetic nanoparticles have been used to guide radionuclides to specific tissues. An approach has been developed to directly label a radioisotope with ferrite particles in in vivo liver tissue in rats. Therapeutic applications are feasible by further conjugation with other medicals.

In magnetic resonance imaging (MRI), magnetite superparamagnetic particles are selectively associated with healthy regions of some tissues (liver, for instance); since these particles change the rate of proton decay from the excited to the ground state (which is the basis of MRI), a different, darker contrast is obtained from these healthy regions of tissue.

Thermal energy from hysteresis loss of ferrites can be used in hyperthermia, that is, the heating of specific tissues or organs for treatment of cancer. The temperature in tumor tissues rises and becomes more sensitive to radio- or chemotherapy. In addition of magnetite, several spinel ferrites (M-Zn, with  $M = \text{Mn}, \text{Co}, \text{Fe}^{2+}$ , and  $\text{Fe}^{2+}\text{-Mn}$ ) are under investigation as well as hexaferrites.

Enzymes, oligonucleotides, antibodies, and other biologically active compounds can be immobilized, as an important technique used in biotechnology. Such immobilized compounds can be targeted to a specific place or can be removed from the system by using an external magnetic field. The compounds can exert their activity on the specific place or tissue or can be used as affinity ligands to trap the cells or target molecules [87]. Magnetic nanoparticles can also be used in a variety of applications: modification, detection, isolation, and study of cells, and isolation of biologically active compounds, for instance.

- **Catalyst:**

Oxidative dehydrogenation of hydrocarbons is commonly catalyzed with a transition metal oxide; for example hematite, which is very active for transforming butane, and ethylbenzene; its selectivity for converting butene into butadiene, however, is low. To increase its selectivity for this reaction, Zn (Mg, Ni or Co) oxide is added to it, giving rise to a ferrite characterized by having the spinel crystalline structure.

For 1-butene oxidative dehydrogenation, the catalytic activity of a ferrite strongly depends on the cation distribution in lattice. For instance, the  $\text{MgFe}_2\text{O}_4$  and the  $\gamma\text{-Fe}_2\text{O}_3$  ferrites, which have an inverted spinel structure (magnesium and iron can occupy octahedral and tetrahedral positions), have similar catalytic activity but higher than the one of stoichiometric  $\text{ZnFe}_2\text{O}_4$  ferrite, whose crystalline structure is non-inverted. These results suggest that the distribution of iron in the tetrahedral and octahedral sites of a ferrite could determine this catalytic activity. Therefore, it is necessary to study in detail the atomic distribution in  $\text{ZnFe}_2\text{O}_4$  ferrite. The cation distribution is responsible of the number of vacancies and the non-stoichiometric, altering bulk and surface properties of the corresponding system, which is of special interest for catalysis.

The ball milling process entailed the use of spherical balls (WC balls, or hardened Steel or stainless steel balls of different sizes) in a hardened steel vials (or WC-lined jars) where the chemical reaction leading to the formation of the desired product phase (magnetic nanoparticles) is achieved as a function of milling time. In addition, ball milling entails a series of variables to achieve the desired product phase and microstructure. Some of these variable parameters are types of mill, milling containers, milling speed, milling time, type, size, and size distribution of the grinding medium, ball-to-powder weight ratio, commonly referred to as BPR, and others [29]. Although previous reports have shown important results which highlight the importance of these parameters, no such report shows a systematic study as a function of BPR for the synthesis of  $\text{ZnFe}_2\text{O}_4$  and by extension, solid solution of solid solution of  $\text{Ni}_x\text{Zn}_{1-x}\text{Fe}_2\text{O}_4$ .

In this study, we undertook the systematic evaluation of the mechano-chemical syntheses of  $\text{ZnFe}_2\text{O}_4$  and the corresponding solid solution  $\text{Ni}_x\text{Zn}_{1-x}\text{Fe}_2\text{O}_4$  materials under identical / comparable conditions as a function of ball milling time. This approach to the study permits the realization of kinetics associated with the mechano-chemical reaction during ball milling. The BPR utilized for this work were 10:1, 20:1 and 40:1. This allows us to analyze changes in the structural and magnetic properties for each synthesis, as well as, investigate the phenomenon related with superparamagnetic behavior. This phenomenon is common types of magnetic behavior which occurs when particles are too small to constitute “domains”, exhibiting positive “exchanges effect” between dipoles. In this state the susceptibility is positive and large ( $1000 \times 10^{-6}$ ) and it increases with field and “saturation” is difficult [69]. Coincidentally, the Mössbauer spectroscopy technique permits unambiguous identification of the phenomenon at varying temperatures. In our case, the room temperature Mössbauer was undertaken in order to

probe if there exist other relationships to superparamagnetic behavior such as cationic distribution which occurs with mechano-chemical synthesis.

### **1.1. Aim of study**

The aim of the present work was to synthesize  $\text{ZnFe}_2\text{O}_4$  by mechano-synthesis, and to study structural properties such as lattice parameter and crystal size with X-ray diffraction (XRD) measurements. Also magnetic properties are to be studied, such as coercivity, saturation magnetization ( $M_s$ ) with vibrating sample magnetometry (VSM) measurement and properties, and cation distribution, quadrupole splitting and isomer shift by Mossbauer spectroscopy. The synthesis was carried out as a function of Ball to Powder Ratio (BPR) in order to study the properties mentioned above.

### **1.2. Literature Review**

Verdier et al. [26] performed a mechanosynthesis of zinc ferrite in hardened steels vials. Milling was performed under air in high-energy planetary mills (Vario-mill, Fritsch) using tempered steel vials (80 ml) and steel balls. The initial powders were hematite ( $\alpha\text{-Fe}_2\text{O}_3$ ) and zincite (ZnO) obtained from Alfa Aesar (99% purity or better). Their crystallite size ranges were between 150-500 nm for zincite and between 100 and 300 nm for hematite. Five new balls of 15mm of diameter were used for each milling and a total of 3.455g of powder mixture. The BPR utilized was 20:1. In their work X-ray diffraction pattern showed a decrease in the peak intensities of ZnO and  $\alpha\text{-Fe}_2\text{O}_3$  after 3h of grinding. After 6h of grinding, the peaks of hematite had almost

disappeared and the spinel phase was observed together with a new phase identified as: a cubic Wüstite-type phase. At 9h of grinding the spinel phase becomes prominent, and one peak of metallic iron whose origin was attributed to the abrasion of the balls and vials made of tempered steel. The authors said that based on the only X-ray diffraction results, it was “hazardous” to conclude to an inversion phenomenon because other authors such as Sepelak and Ermakov [26] had reported that the effect of the high-energy ball milling on zinc ferrite is a change in its structure (normal to inverse) and that this phenomenon was related to contraction of the crystal lattice, while Li et al.[26] had determined an inversion parameter by Mössbauer spectroscopy without observing any decrease in the cell parameter. Mössbauer spectrum of milled  $\text{ZnFe}_2\text{O}_4$  consisted in a broadened doublet which does not allow detect the presence of Fe (II). The broadening of the doublet is usually attributed to a change in the ions location, associated with zinc leaving progressively tetrahedral sites to go into octahedral sites during the milling and, to the inter sublattice interaction of the  $\text{Fe}^{3+}[\text{B}]-\text{O}_2-\text{Fe}^{3+}[\text{B}]$  allowed by the deformation of bond angles induced by milling [26]. The spinel compound obtained after milling hematite and zincite was not a zinc ferrite containing only  $\text{Fe}^{3+}$  cations, but it was a zinc substituted magnetite [26]. The presence of Fe (II) allowed explaining the shape of the Mössbauer spectrum which is unusual for this type of milling. The appearance of this Fe(II)-containing phase was explained by a contamination due to iron from vials and balls, and by a redox reaction between iron and Fe(III) of hematite where this reaction only occurs in the presence of ZnO by the intermediate formation of a Wüstite-type phase solid solution between ZnO and FeO.

Jean and Nachbaur [28] studied the mechano-synthesis of Zinc ferrite in WC vials. They determined the milling parameters to obtain  $\text{ZnFe}_2\text{O}_4$  in an efficient way. The milling parameters included rotational speeds of main disc and vials. The purpose was to obtain a pure zinc ferrite

phase. The experiments were performed under air atmosphere in a high-energy planetary mill (Vario-planetary Mill pulverisette 4, Fritsch), using tungsten carbide vials and balls. The BPR was 20:1 and 10 balls of 10 mm of diameter were used. Six pairs of velocities were chosen, by adjusting the velocities of the main disk and the planets. They were represented for the pair  $(\Omega, \omega)$  respectively. The values of the milling modes were B = (500, -500), C = (500, -900), F = (250, -900), A = (500, -250), D = (250, -250), E = (250, -500) rpm. The authors classified the modes as efficient, low, and high, based on the X-ray diffraction results analyses. For example, A and D modes were classified as not efficient milling because, in this case, no spinel phase was synthesized, i.e., observed in XRD analyses. Mode E was classified as low efficient milling because, in this case, a spinel phase was obtained, but initial oxides still remained. The B, C and F modes were denoted as high efficient milling because, in these cases, a pure spinel phase was formed in less time than in the previous modes.

For milling mode B, after 12h of milling, the peaks of hematite had almost disappeared, but ZnO was not visible. In this case only spinel phase was present after 18 and 24h. For the C mode, the spinel phase was observed after 12h of milling. In the F mode, the spinel phase appeared before 12h of milling, but in this case the milling had to be prolonged up 36h to obtain a pure phase with no hematite. For the case of milling modes A and D, the predominant phases were the initial oxides, even for an 18h milling, obtaining a reduction in the particle size of hematite from 100 nm to 40 nm in both cases. Finally, for milling mode E, a broadening in the peaks of the initial oxides and a small amount of spinel phase was formed after 18h of milling was observed. The Mössbauer spectra reported by the authors showed a central doublet for B, C and F modes, with milling times of 18, 12 and 36h, thus showing greater efficiency, of C mode. The paramagnetic doublet is attributed to Fe atoms located only in octahedral sites. Moreover, Mössbauer spectra

of B, C and F modes showed broadened doublets that related to an inversion of the cation distribution commonly observed in ferrites obtained by mechanochemical synthesis. They concluded that by varying main disk and vials velocities, several milling modes may be reached presenting several degrees of efficiency which may be linked to the value of injected power and to the friction of the ball on the vial wall. In addition, they found that a high injected power and high friction component are conducive to obtaining pure zinc ferrite in a relatively short time; in this case, for the C milling mode described earlier.

Yang et al. [30] worked on zinc ferrite nanocrystals by a Mechanochemical reaction. The precursor materials used were AR-grade ZnO and hematite ( $\alpha$ -Fe<sub>2</sub>O<sub>3</sub>). The powders were dried at 150°C in air for 12h prior to use. Dried ZnO and  $\alpha$ -Fe<sub>2</sub>O<sub>3</sub> were mixed with a molar ratio of 1:1 to form the mixture. Mechanochemical milling was performed with a KM-10 type planetary mill for 0 – 8h at 600 rpm using a ball-to-powder mass ratio of 10:1. The as-milled powder was dried in air at 100 °C to produce the nanoparticle precursor. The precursor was subsequently calcined at 600°C in air in a porcelain crucible for 1h to obtain ZnFe<sub>2</sub>O<sub>4</sub> nanocrystallites. Among the conclusions reached in this investigation is that the nanocrystals can be synthesized by heating the precursor obtained by the mechanochemical reaction of ZnO and  $\alpha$ -Fe<sub>2</sub>O<sub>3</sub>. Also, it was found that the crystal size was easily affected by the calcinations temperatures ranging from 19 nm to 35 nm at 550 - 800°C.

Ahn et al. [31] worked on “Magnetization and Mossbauer study of nanosize ZnFe<sub>2</sub>O<sub>4</sub> Particles Synthesized by Using a Micro-emulsion Method”. Zinc-Iron Hydroxide carbonate synthesized in aerosol OT/water /iso-octane inverse micro- emulsion systems was used. The precipitate, zinc-iron hydroxide carbonate particles were achieved by mixing two micro-emulsions; one

containing Fe(III)/Zn(II) and the other  $\text{Na}_2\text{CO}_3$ . The precipitate was washed with solvent and dried at about  $100\text{ }^\circ\text{C}$ . The nanophase precursor particles were readily calcinated at about  $330\text{ }^\circ\text{C}$  into metal oxide. XRD patterns of the sample were obtained with  $\text{Cu-K}\alpha$ , and the particle size and the size distribution were examined by TEM. Magnetization measurements were performed in a SQUID between 5 and 300K in fields up to 50 KOe. Besides, a Mössbauer spectroscopy measurement was also carried out. This study concluded that the sample had a cubic structure with a spinel lattice constant of  $8.43\text{ \AA}$ . It showed that the asymmetric broadening and the large linewidths of the Mössbauer spectral lines arose from the different temperature dependence on the basis of the magnetic hyperfine fields due to the distribution of  $\text{Fe}^{3+}$  ions at both tetrahedral (A) sites and octahedral (B) sites. In the Fig. 1 we can observe the Mössbauer spectra for different temperatures.

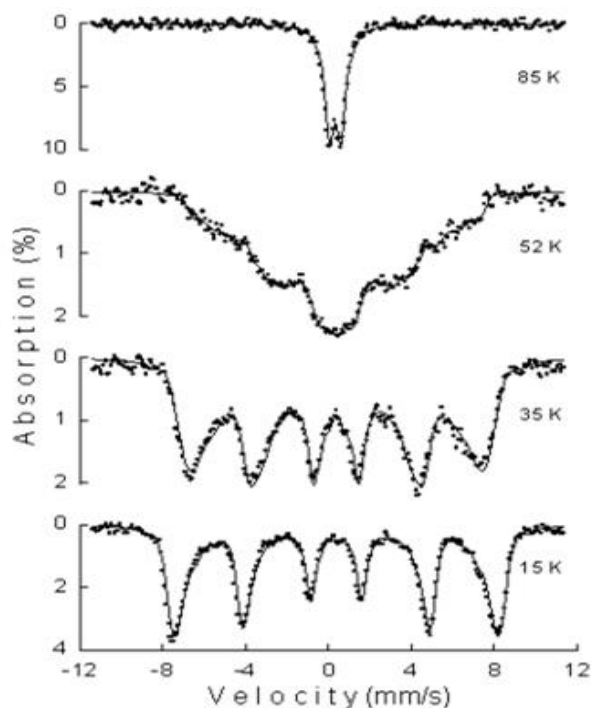


**Figure 1: Mössbauer spectra of nanosize  $\text{ZnFe}_2\text{O}_4$  particles at various temperatures.**

Bid and Pradhan [21] synthesized nanocrystalline zinc ferrite at room temperature by high-energy ball milling with stoichiometric (1:1 %) mixture of ZnO and  $\alpha$ -Fe<sub>2</sub>O<sub>3</sub>. This synthesis was conducted in a planetary ball mill (Model P5) where a disk carrying vials rotated in opposite direction. The rotation speed of the disk was 325 rpm and that of the vials was about 475 rpm. Milling of powder was done at room temperature in hardened chrome steel (Fe- 1 wt. % Cr) vials (volume 80 ml), and, 30 hardened chrome steel balls of 10 mm of diameter each were used at BPR = 40:1 with variations in the milling time from 30 min to 10h. In this work the authors adopted the Rietveld's powder structure refinement analysis of X-ray powder diffraction to obtain the refined structural parameters, such as atomic coordinates, occupancies, lattice parameters, etc and microstructural parameters, such as particle size and *rms* lattice strain. The crystal size for zinc ferrite varied from 18.9 until 12.8 nm in the interval time of 0.5 h to 10h, and the lattice parameter ranged from 8.4183 until 8.4274 for the same interval of time mentioned above. It can be seen that while the crystal size decreased as the milling time evolved, the lattice parameter shown an increase in its value. [21]. Compared with Verdier et al.'s work, the spinel Phase in the Bid's work is reached in a lesser time, and this fact can be due to a several factors, as velocities of main disks and jars, and the BPR utilized by them. For example, the velocities for main disk and jars utilized by Bid and Pradhan were higher than those utilized by Verdier et al. Moreover, Verdier et al., used a BPR of 20:1, Bid and Pradhan utilized a BPR of 40:1. These differences in the BPRs allowed get different times to complete the reactions. It can be seen that velocities of main disk and jars, and also milling parameters affect the velocities of the reaction of the syntheses.

## **2. THEORETICAL BACKGROUND**

### **2.1. Magnetism and Magnetic materials**

Materials are classified by their response to an externally applied magnetic field. Descriptions of the orientations of the magnetic moments in a material help to identify different forms of magnetism observed in nature. When an externally applied magnetic field is applied, the atomic current loop created by the orbital motion of electrons responds to oppose the applied field. According to this response, we can describe five basic types of magnetism, namely: diamagnetism, paramagnetism, ferromagnetism, antiferromagnetism and ferrimagnetism.

#### **2.1.1. Diamagnetism**

Diamagnetism is present in all matter but is often obscured by paramagnetism or ferromagnetism. It does not require that the atoms have orbital moment or unpaired spin; it occurs for filled or partially filled orbitals, and it is associated with the tendency of electrical charges to partially shield the interior of a body from an applied magnetic field. According to this, diamagnetism is seen simply as a manifestation of Lenz's law: moving charges (screening currents), respond to a change in field by changing their motion so as to set up a field (response) that opposes the initial change. However, quantum mechanics gives certain stability to the screening currents, resulting in a tendency, usually very weak, for all matter to exclude applied fields. This weak diamagnetism, called Landau diamagnetism of normal metals contrast sharply with the situation in superconductor [80].

### 2.1.2. Paramagnetism

Paramagnetism is the trend of the magnetic moments in a material to align with external magnetic field causing a net magnetization in the substance [65]. The electronic paramagnetism occurs in atoms, molecules, and lattice defects possessing an odd number of electrons, as in this case the total spin of the system cannot be zero. Moreover, paramagnetism is found in free atoms and ions with a partly filled inner shell such as in transition elements, rare earths and actinides elements, a few compounds with an even number of electrons, and in metals. The origin of paramagnetism is based on the sources of the magnetic moment of a free atom, which are: the spin with which electrons are endowed, their orbital angular momentum about the nucleus and the change in the orbital moment induced by an applied magnetic field. The first effects give paramagnetic contributions to the magnetization, while the third gives diamagnetic contribution.

The magnetic moment of an atom or ion in free space is given by:

$$\boldsymbol{\mu} = \gamma \hbar \mathbf{J} = -g \boldsymbol{\mu}_B \quad (1)$$

where the total angular momentum  $\hbar \mathbf{J}$  is the sum of the orbital  $\hbar \mathbf{L}$  and spin  $\hbar \mathbf{S}$  angular momenta.

The constant  $\gamma$  is called the **gyromagnetic ratio** or **magnetogyric ratio**. For electronic systems a quantity  $g$  called the  $g$  factor or the spectroscopic splitting factor is defined by

$$-\gamma \hbar = g \boldsymbol{\mu}_B \quad (2)$$

For a free atom the  $g$  factor is given by the Landé equation

$$\mathbf{g} = \mathbf{1} + \frac{J(J+1)+S(S+1)-L(L+1)}{2J(J+1)} \quad (3)$$

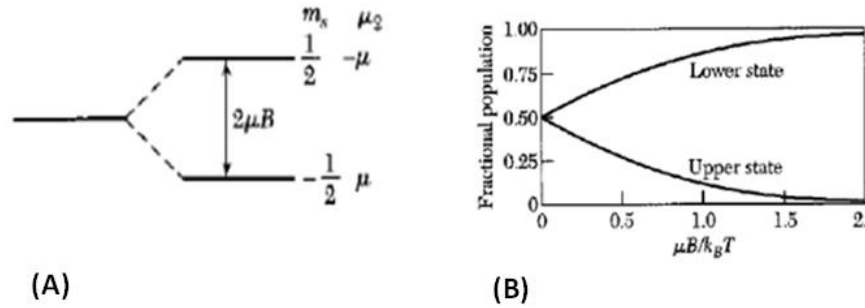


Figure 2: (A) Energy level splitting for one electron in a magnetic field directed along the positive z axis. (B) Fractional populations of a two-level system in thermal equilibrium at temperature T in a magnetic field B [65].

The Bohr magneton  $\mu_B$  is defined as  $e\hbar/2m$  in SI and it is closely equal to the spin magnetic moment of a free electron.

The energy levels of the system in a magnetic field are obtained from the following expression:

$$U = -\boldsymbol{\mu} \cdot \mathbf{B} = m_j g \mu_B B \quad (4)$$

where  $m_j$  is the azimuthal quantum number and has the values  $J, J-1, \dots, -J$ . For a single spin withno orbital moment we have  $m_j = \pm 1/2$  and  $g=2$ , whence

$$U = \pm\mu_B B \quad (5)$$

This splitting was shown in figure 2.

If a system has only two levels the equilibrium populations are, with  $\tau = k_B T$ ,

$$\frac{N_1}{N} = \frac{\exp\left(\frac{\mu_B B}{\tau}\right)}{\exp\left(\frac{\mu_B B}{\tau}\right) + \exp\left(-\frac{\mu_B B}{\tau}\right)} \quad (6)$$

$$\frac{N_2}{N} = \frac{\exp\left(-\frac{\mu_B B}{\tau}\right)}{\exp\left(\frac{\mu_B B}{\tau}\right) + \exp\left(-\frac{\mu_B B}{\tau}\right)} \quad (7)$$

Here  $N_1, N_2$  are the populations of the lower and upper levels, and  $N = N_1 + N_2$ , is the total number of atoms. The fractional populations are shown in the Fig. 2B). The projection of the magnetic moment of the upper state along the field direction is  $-\mu$  and the lower state is  $\mu$ . The resultant magnetization for  $N$  atoms per unit volume is:

$$M = (N_1 - N_2) \mu = N \mu \tanh x \quad (8)$$

with  $x = \mu_B B / k_B T$

In a magnetic field an atom with angular momentum quantum number  $J$  has  $2J+1$  equally spaced energy levels. The magnetization is given by

$$M = NgJ\mu_B B_J(x) \quad (9)$$

with  $x = gJ\mu_B B/\mu_B T$  and  $B_J(x)$  is the Brillouin function. The last equation is known as the Curie-Brillouin function law. [65]

### **2.1.3. Ferromagnetism and Antiferromagnetism**

#### ***2.1.3.1. Ferromagnetic order***

A ferromagnet has a spontaneous magnetic moment even in zero applied magnetic field. The existence of a spontaneous moment suggests that electron spins and magnetic moments are arranged in a regular manner.

#### ***2.1.3.2. Curie point and the exchange integral***

Consider a paramagnet with a concentration of  $N$  ions and spin  $S$ . If there is an internal interaction tending to line up the magnetic moments parallel to each other, we shall have a ferromagnet. This interaction is called exchange field and also called the molecular field or the Weiss field, after Pierre Weiss who was the first to imagine such field [65]. The orienting effect of the exchange field is opposed by thermal agitation, and at elevated temperatures the spin order is destroyed. We treat the exchange field as equivalent to a magnetic field  $\mathbf{B}_E$ . We assume that  $\mathbf{B}_E$  is proportional to magnetization  $\mathbf{M}$ . If domains are present, the magnetization refers to the

value within a domain. In the **mean-field approximation** we assume each magnetic atom experiences a field proportional to the magnetization:

$$\mathbf{B}_E = \lambda \mathbf{M} \quad (10)$$

where  $\lambda$  is a constant, independent of temperature. According to the last equation, each spin sees the average magnetization of all the other spins. There is a temperature above which the spontaneous magnetization vanishes. This temperature is called Curie temperature  $T_c$  and it separates the disordered paramagnetic phase at  $T > T_c$  from the ordered ferromagnetic phase at  $T < T_c$  (See eq. 12.). At this temperature,  $T_c$ , (and below) there exist a spontaneous magnetization, because if  $\chi$  is infinite we have a finite  $M$  for zero applied field ( $B_a$ ).

In the paramagnetic phase, an applied field  $B_a$  will cause a finite magnetization and this in turn will cause a finite exchange field  $B_E$ . If  $\chi_p$  is the paramagnetic susceptibility,

$$\mu_0 M = \chi_p (B_a + B_E) \quad (11)$$

The paramagnetic susceptibility is given by the Curie law  $\chi_p = C/T$ , where  $C$  is the Curie constant. If we utilize this law and the last equation, we get:

$$\chi = \frac{M}{B_a} = \frac{C}{T - C\lambda} \quad (12)$$

The last equation shows that the susceptibility has a singularity at  $T = C\lambda$ . The last equation describe fairly well the observed susceptibility variation in the paramagnetic region above the Curie point and is known as **Curie-Weiss law** with  $T_c = C\lambda$ .

### 2.1.3.3. *Antiferromagnetism*

In an antiferromagnet the spins are ordered in an antiparallel arrangement with zero net moment at temperatures below the ordering or Neel temperature  $T_N$ . When  $T = T_N$ , the susceptibility is not infinite, it has a weak cusp. Contrary to a ferromagnetic material, in an antiferromagnetic material, the exchange energy is large and negative so that the lowest-energy state is that in which neighboring dipoles have antiparallel alignment, as shown in the figure 3. It means that the material would not show any spontaneous magnetization [71]. The arrangement of atoms in an antiferromagnetic material can be visualized as consisting of two interpenetrating sub-lattices in either one of which the spins are aligned parallel, where these sub-lattices have opposite spins orientations. This division in two sub-lattices is the basis of Neel's theory [71]. Denoting these sub-lattices as A, and, B, we assume that a spin in lattice A, would be subject to the combination of an applied field  $H$ , and a field due to magnetization,  $M_B$ , of sub-lattice B. This assumes that the antiferromagnetic exchange interaction between atoms on lattice A, and those on lattices B, is so large that all other interactions may be neglected compared with it. Similarly, a spin in lattice B is subject to  $H$  and  $M_A$  such that the effective fields will therefore be given as:

acting on A  $H_A = H - \lambda M_B$  (13)

and acting on B

$$H_B = H - \lambda M_A \quad (14)$$

where  $\lambda$  is a Weiss molecular field constant, and the negative sign arises from negative exchange interaction. Each sub-lattice obeys Curie's law and shows paramagnetic behavior at high temperature. The susceptibility is given by:

$$\chi = \frac{M}{\mu H} = \frac{C}{T + \frac{1}{2} \mu \lambda C} = \frac{C}{T + \theta_N} \quad (15)$$

where  $\theta_N$  has just half the value of the Weiss constant of equation 10 , and is of the opposite sign.

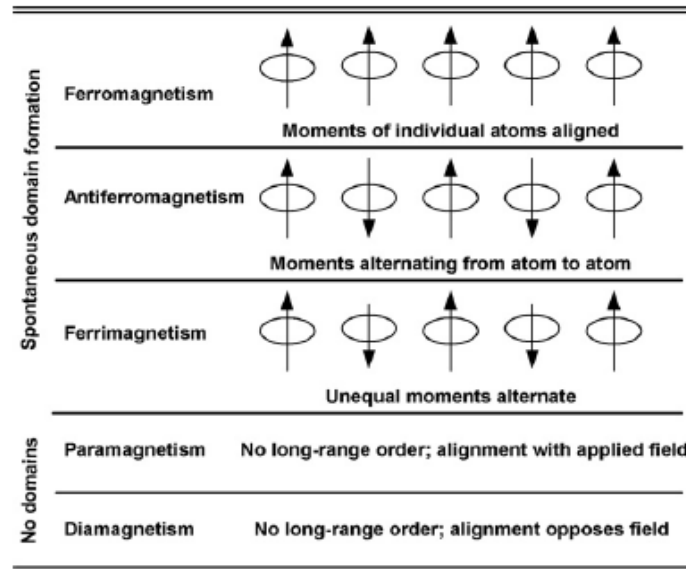
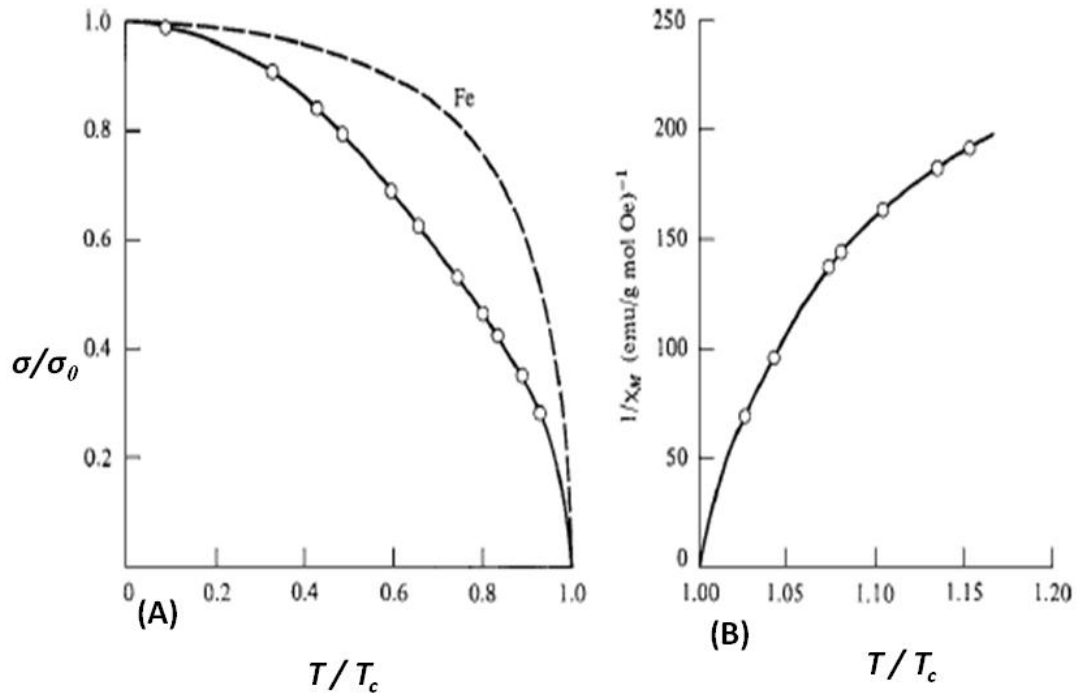


Figure 3: Different types of magnetic behaviors [32].

#### 2.1.4. Ferrimagnetism

Ferrimagnetic substances exhibit a substantial spontaneous magnetization at room temperature, just like ferromagnetic ones, and this fact alone makes them industrially important. Similar to ferromagnetic materials, they consist of magnetically saturated domains, and exhibit the phenomena of magnetic saturation and hysteresis. Their spontaneous magnetization disappears above a certain critical temperature  $T_c$ , (also called Curie temperature) and they become paramagnetic (See Fig 4) Inspection of figure 4 yields further evidence that the ferrites are not ferromagnetic. The fractional magnetization of a typical ferrite decreases rather rapidly with increasing temperature, whereas the value of  $M/M_s$  for iron, for example, remains large until  $T/T_c$  exceeds about 0.8. Furthermore, in the paramagnetic region, the variation of the inverse susceptibility with temperature is decidedly nonlinear, which means that the Curie-Weiss law is not obeyed, See Fig. 4 (B). The term Ferrimagnetic was coined originally to describe a ferrite-type ferromagnetic spin order, and by extension the term covers almost any compound in which some ions have a moment anti parallel to other ions, such as shown in the Fig.3 [73].



**Figure 4: Temperature dependence of magnetic properties of a typical ferrimagnetic (NiO·Fe<sub>2</sub>O<sub>3</sub>). Figure 4 (A) shows the fractional saturation magnetization per unit mass in the ferrimagnetic region and figure 4(B) shows the reciprocal susceptibility (per mole) in the paramagnetic region. The dashed curve in the left –hand figure is the corresponding data for metallic iron [73].**

In the figure shown below, we can observe a model of spin arrangement in magnetite, FeO·Fe<sub>2</sub>O<sub>3</sub>. In this arrangement the ferric Fe<sup>3+</sup> ions are in a state of spin,  $s = \frac{5}{2}$  and zero orbital moment. Thus, each ion would contribute a total of  $5\mu_B$ . The ferrous ions Fe<sup>2+</sup> with spin of 2 would contribute a total of  $4\mu_B$ , apart from any residual orbital moment contribution. Thus the effective number of Bohr magnetons per Fe<sub>2</sub>O<sub>4</sub> formula unit should be about  $2*5 + 4 = 14$ , if all spins were parallel. But the observed value is 4.1. This difference between these values is accounted for if the moments of the Fe<sup>3+</sup> are antiparallel to each other, which implies that the observed moments arises only from the Fe<sup>2+</sup> ions, as is shown in Fig 5. Measurements of neutron diffraction result agree with this model [65].

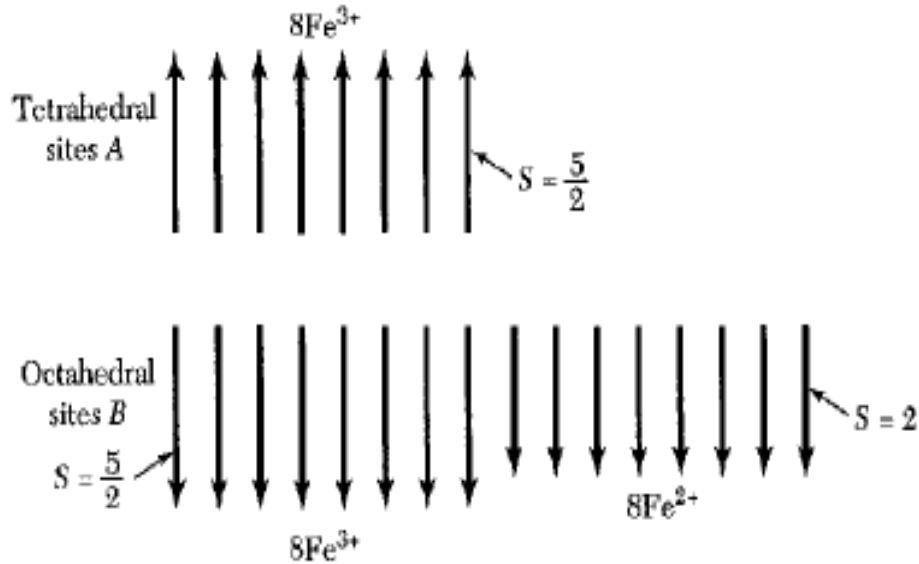


Figure 5: Spin arrangements in a magnetite,  $\text{FeO} \cdot \text{Fe}_2\text{O}_3$  showing how the moments of the  $\text{Fe}^{3+}$  ions cancel out, leading only the moments of  $\text{Fe}^{2+}$  [65].

## 2.2. Magnetic domains

Domains are groups of spins all pointing in the same direction and acting cooperatively. They are separated by domain walls, which have a characteristic width and energy associated with their formation and existence [32]. Within each domain the local magnetization is saturated. Domains not only form in ferromagnetic, but also in antiferromagnetic, ferroelectrics, antiferroelectrics, ferroelastic, superconductors, and sometimes in metals under conditions of a strong de Haas-van Alphen effect [65]. Two facts can increase the gross magnetic moment of a ferromagnetic specimen in a magnetic field. These processes are independent and they are:

- In weak applied fields the volume of domains favorably oriented with respect to the field increases at the expense of unfavorable oriented domains. In the Fig.6 we can observe this fact.

- In a strong applied field the domain magnetization rotates toward the direction of the field.

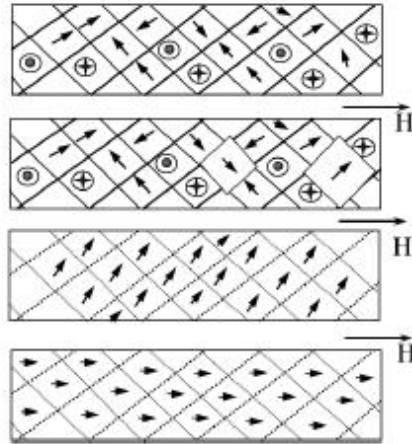


**Figure 6: Schematic representation of magnetization process explained by magnetic domain [78]**

### 2.3. Anisotropy energy

This is the energy that directs the magnetization vector along certain crystallographic axes called directions of easy magnetization. This energy is commonly called the magnetocrystalline or anisotropy energy. It does not come about from the pure isotropic exchange interaction. One origin of the anisotropy energy can be seen in the Fig. 7. The magnetization of the crystal sees the crystal lattice through orbital overlap of the electron; namely, the spin interacts with the orbital motion by means of the spin-orbit coupling. Iron is a cubic crystal where the cube edges are the directions of easy magnetization and the expression for the anisotropy energy is given by:

$$U_K = K_1 (\alpha_1^2 \alpha_2^2 + \alpha_2^2 \alpha_3^2 + \alpha_3^2 \alpha_1^2) + K_2 \alpha_1^2 \alpha_2^2 \alpha_3^2 \quad (16)$$

where  $\alpha_1, \alpha_2$  and  $\alpha_3$  are the direction cosines and  $K_1 = 4.2 \times 10^5 \text{ erg/cm}^3$  and  $K_2 = 1.5 \times 10^5 \text{ erg/cm}^3$ .

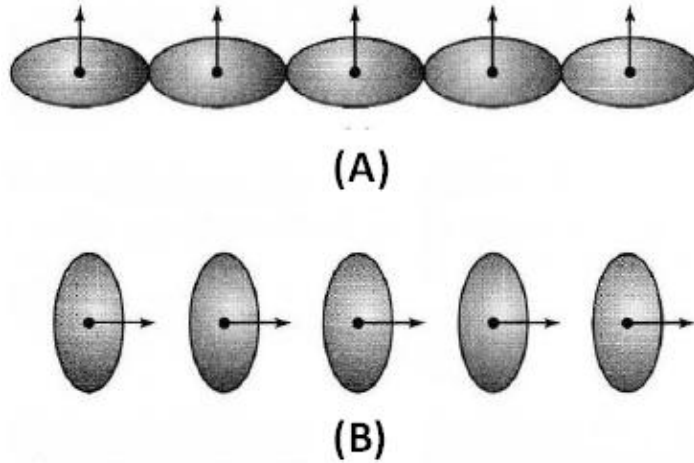


**Figure 7: Asymmetry of the overlap of electron distributions on neighboring ions provides one mechanism of magnetocrystalline anisotropy. The asymmetry is tied to the direction of the spin, so that a rotation of spin directions relative to the crystal axes changes the exchange energy and also changes the electrostatic interaction energy of the charge distribution on pairs of atoms, giving rise to anisotropy energy. In the figure, the energy in (A) is not the same as the energy of (B) [65]**

A Bloch wall in a crystal is the transition layer that separates the domains. We know that inside each domain the spin points out in the same direction. But the entire change in spin direction between domains does not occur in one discontinuous jump across a single atomic plane. It occurs in a gradual way over many atomic planes (See Fig. 8). The anisotropy energy acts to limit the width of the transition layer. This energy is proportional to the wall thickness. Within the wall the spins are largely directed away from the axes of easy magnetization.

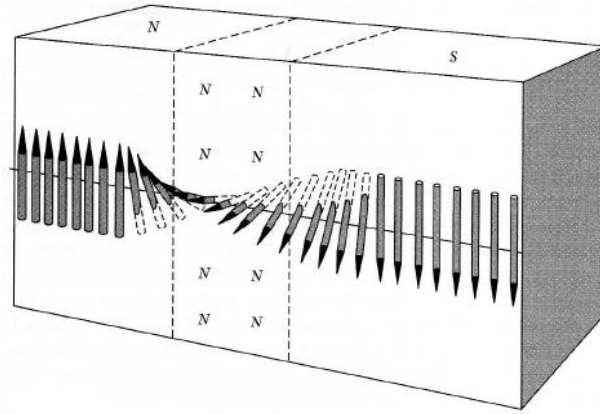


**Figure 8: The structure of the Block wall separating domains. In iron the thickness of the transition region is about 300 lattice constants [65].**

## 2.4. Single domains

An ideal single domain particle is a fine particle, usually elongated; that has its magnetic moment directed toward one end or the other of the particle. This orientations can be designed by N or S; + or -; in digital recording, as 0 or 1 [65]. Effective elongation can be attained with spheres by making a chain, like a string of beads. An ensemble of such chains or of elongated single domains particles is said to exhibit superparamagnetism if the magnetic moment of a unit is constant. The phenomenon of superparamagnetism will be briefly discus later. It is important to highlight that when the size of the particles is reduced below certain value, they will not contain domain walls and in this case the particle will consist only of a single domain as was mentioned earlier. When the size of the particle is less than the thickness of a domain wall, no two domains can coexist, and moreover, if the magnetic energy of the particle decreases with the volume, the wall energy decreases with the area. Typical single domain nanoparticles could have a diameter of the size less than about 100 atoms [81]

### 2.4.1. Origin of single domains

Domain is a natural consequence of various contributions to the energy- exchange, anisotropy, and magnetic-of a ferromagnetic body. This fact was showed by Landau and Lifshitz. Direct evidences of domain structures are furnished by technique such as, of magnetic powder pattern and by optical studies using Faraday rotation [65]. In the figure 9 we can observe the origin of the domains. In Fig.9 (a) we have a single domain; as a consequence of the magnetic poles formed on the surfaces of the crystal this configuration will have a high value of the magnetic energy. In 9(b) the energy is reduced by about one-half by dividing the crystal into two domains magnetized in opposite directions. In 9(c) with  $N$  domains the magnetic energy is reduced to approximately  $1/N$  of the magnetic energy of 9(a) due to the reduced spatial extension of the field.

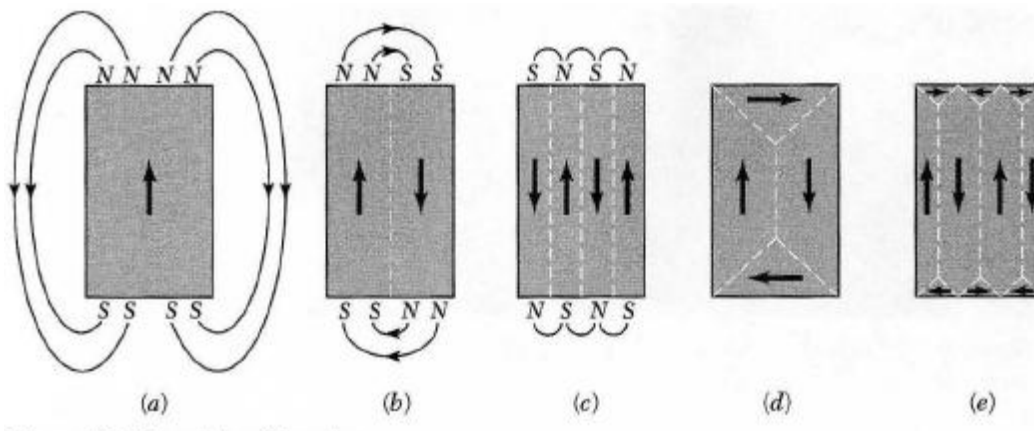


Figure 9: Representation of Origin of domains [65].

In arrangement such as 9(d) and 9(e) the magnetic energy is zero. Here, the component of magnetization normal to the boundary is continuous across the boundary and there is no magnetic field associated with the magnetization. The flux circuit is completed within the

crystal, giving rise to the term domains of closure for surface domains that complete the flux circuit [65].

## 2.5.Saturation Magnetization

The magnetization is defined by magnetic moment per unit volume of a solid. This is

$$\mathbf{M} = \frac{m}{v} \quad (17)$$

Since the unit of magnetic moment is *erg/Oersted*, the unit of magnetization  $\mathbf{M}$  is *erg/Oersted cm<sup>3</sup>*, or simply *emu/cm<sup>3</sup>*. It is sometimes convenient to refer the value of magnetization to units mass rather than unit volume. Consequently, it is defined the specific magnetization  $\sigma$  as:

$$\sigma = \frac{m}{w} = \frac{m}{v\rho} = \frac{\mathbf{M}}{\rho} \text{ emu/g}, \quad (18)$$

where  $w$  is the mass and  $\rho$  the density.

When a substance is placed in a magnetic field, the total magnetic in the region is expressed as:

$$\mathbf{B} = \mathbf{B}_0 + \mu_0\mathbf{M} \quad (19)$$

Analyzing the magnetic field that arises from magnetization, it is convenient to introduce a field quantity called magnetic field strength  $\mathbf{H}$  within the substance. The magnetic field strength is the magnetic moment per unit volume due to currents; thus, it is similar to the vector  $\mathbf{M}$  it which can also be defined by  $\mathbf{M} = \mathbf{B} / \mu_0$ . This similarity between,  $\mathbf{M}$ , and  $\mathbf{H}$ , allows define  $\mathbf{H}$  as:

$$\mathbf{H} = \mathbf{B}_0/\mu_0 \quad (20)$$

Thus, the Eq.19 can be written as:

$$\mathbf{B} = \mu_0(\mathbf{H} + \mathbf{M}) \quad (21)$$

the quantities  $\mathbf{H}$  and  $\mathbf{M}$  has the same units. Its SI units are Amperes/ meter (A/m).

The saturation magnetization of a material  $\mathbf{M}_0$  is defined by the product of  $n$  and  $\mathbf{m}$ , where  $n$  is the elementary atomic magnetic dipoles per unit volume of each magnetic moment,  $\mathbf{m}$ , when all these moments are aligned parallel. This is:

$$\mathbf{M}_0 = nm \quad (22)$$

$\mathbf{M}_0$  is termed the saturation magnetization. We can make a distinction between technical saturation  $\mathbf{M}_s$  and complete saturation  $\mathbf{M}_0$ . Technical saturation is achieved when a material is converted to a single magnetic domain, but at higher fields the magnetization increase very slowly beyond technical saturation. This slow increase of magnetization at high fields is due to an increase in the spontaneous magnetization within a single domain and is known as forced magnetization [73].

## 2.6.Coercivity

We know that when ferromagnetic materials can be highly magnetized by a magnetic field their magnetization is changed by a magnetic field in a complex way, which is described by a magnetization curve as shown in the Fig. 10.

Starting from a demagnetized state ( $M = H = 0$ ), the magnetization increases with increasing field along the curve OABC and finally reaches the saturation magnetization, which is normally denoted by  $M_s$ . If the magnetic field is decreased from the saturated state C, the magnetization  $M$  gradually decreases along CD, not along CBAO, and at  $H = 0$  it reaches the non-zero value  $M_r$ , which is called the residual magnetization or the remanence. If we continue increasing the magnetic field in a negative sense, it results in a continued decrease of the intensity of magnetization, which finally falls to zero. The absolute value of the field at this point is called the coercive force or the coercive field  $H_c$ . In other words, the coercivity is the magnetic field  $H_c$  required to reduce the magnetization or the induction  $B$  to zero. The value of the coercivity ranges over seven orders of magnitude. Materials with low coercivity are called soft and those with high coercivity are called hard. The coercivity of fine particles has a noticeable dependence on their size. As the particle size is reduced, it is typically found that the coercivity increases, experiences a maximum, and then tends toward zero [73].

In the figure 9 the portion, DE, of the magnetization curve is often referred to as the demagnetization curve. Further, increases of  $H$  in a negative sense result in an increase of the intensity of magnetization in a negative sense and finally to negative saturation magnetization. If the field is then reversed again to the positive sense, the magnetization will change along FGC.

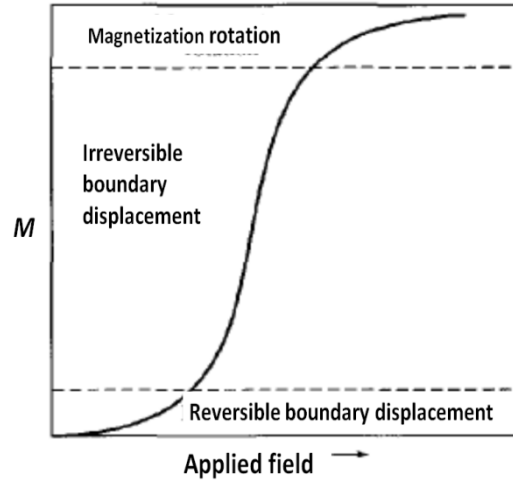


Figure 10: Representative magnetization curve, showing the dominant magnetization process in the different regions of the curve [65].

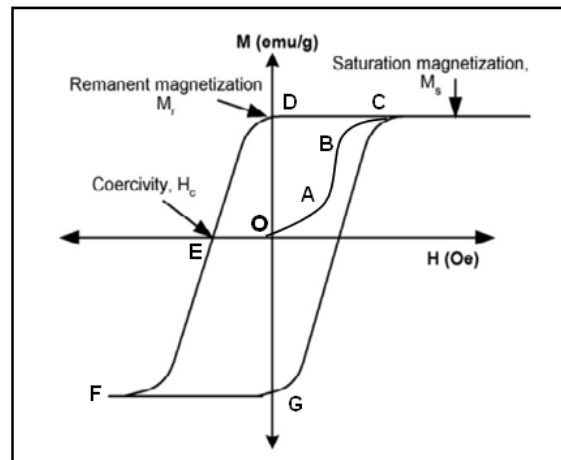


Figure 11: Hysteresis loop, where  $H$  is the magnetic field strength (Oe), and  $M$  is the magnetization of the material ( $\text{emu/g}$ ) [32].

The closed loop CDEFGC is called the hysteresis loop. The apparent magnetization curve of a material depends not only on its magnetic susceptibility, but also on the shape of the specimen

[77]. When a specimen of finite size is magnetized by an external magnetic field, the free poles which appear on its ends will produce a magnetic field directed opposite to the magnetization (See fig.12). This field is called the demagnetization field. The intensity of the demagnetizing field  $H_d$  is proportional to the magnetic free pole density and therefore to the magnetization, so that we have:

$$H_d = N \frac{M}{\mu_o} \quad (23)$$

where  $N$  is called the demagnetization factor, which depends only on the shape of the specimen. For instance,  $N$  approaches zero for an elongated thin specimen magnetized along its long axis, whereas it is large for a thick and short specimen. [77].

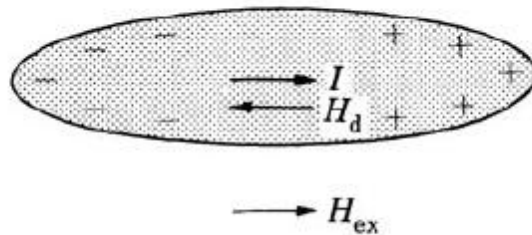


**Figure 12: surface magnetic free poles and resulting demagnetizing field [65].**

The coercivity decreases with decreasing impurities and strain in the material, i.e., in a very pure, unstrained single crystal the hysteresis loop is narrow [81].

## 2.7.Ferrites

In the introduction we talked about the ferrites where we briefly defined them, and mentioned some of their most important applications depending on some properties such as coercivity, resistivity, and among others that permit their different applications. In this section we are going to show other important characteristics associated with them.

The most important ferrimagnetic substances are certain double oxides of iron and other metal, called ferrites. These ferrites were developed into commercially useful magnetic materials, chiefly during the period of 1933-1945, by Snoek and his associates at the Philips Research Laboratories in the Netherlands [73].

The magnetic ferrites fall mainly into two great groups with different crystal structures:

1. Cubic. These have the general formula  $MO \cdot Fe_2O_3$ , where M is divalent metal ion, like Mn, Ni, Fe, Co, or Mg. Cobalt ferrite  $CoO \cdot Fe_2O_3$  is magnetically hard, but all the other cubic ferrites are magnetically soft.

2. Hexagonal. The most important in this group are barium and strontium ferrites,  $BaO \cdot 6Fe_2O_3$  and  $SrO \cdot 6Fe_2O_3$  which are magnetically hard.

### 2.7.1. Structure of cubic ferrites

Depending on the distribution of cations in the spinel structure, these are called normal or inverse. Normal Spinel have the general formula  $(M)^A(N_2)^B O_4$ , where, M, and N are divalent and trivalent ions, respectively. A and B represent the spaces occupied by oxygen ions and can be of two kinds. The A sites are called tetrahedral sites because they are located in the center of a tetrahedron whose corners are occupied by oxygen ions. The B site is called octahedral site, because the oxygen ions around it occupy the corners of an octahedron. Of course, this makes the environments crystallographic of sites A and B totally different. The following figures illustrate the above.

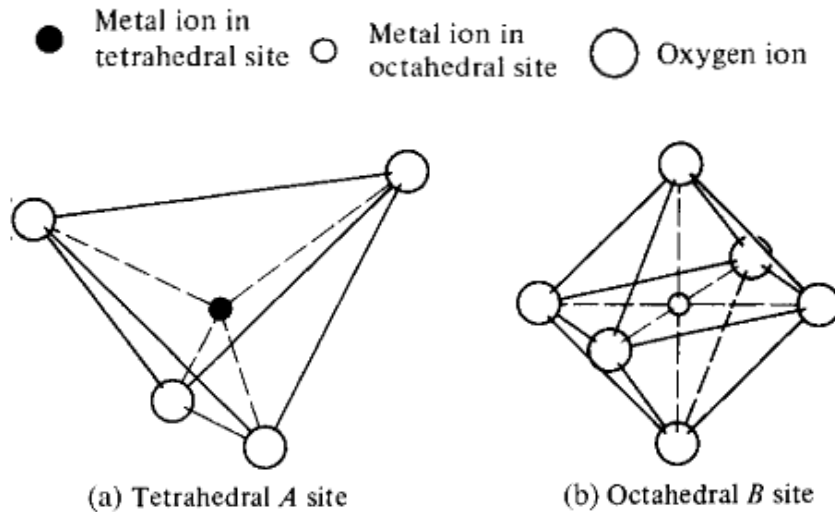


Figure 13: Environments crystallographic of A sites and B sites [65].

In some, system, and particularly high temperatures, the cation distribution may be disordered and the cations nearly randomly distributed on B sites and between A and B sites, but generally there is a tendency for individual ions to fit into particular sites so that either the normal or

inverse arrangement is preferred. Moreover, factors such as cation size, crystal field and valence play a role in site selection [84]. For example, magnetite has two  $\text{Fe}^{3+}$  ions and one  $\text{Fe}^{2+}$  ion. In this case,  $\text{Fe}^{3+}$  has much stronger tetrahedral (inverse) site preference than  $\text{Fe}^{2+}$ , it means that one of the  $\text{Fe}^{3+}$  ions occupies the A sites and relegates to the other two ions ( $\text{Fe}^{3+}$  and  $\text{Fe}^{2+}$ ) to the two B sites per formula unit. Hence, it is said that magnetite has the inverse sites occupations. On the other hand,  $\text{Zn}^{2+}$  has by far the strongest preference for A site occupation of any other ions such as:  $\text{Mn}^{2+}$ ,  $\text{Fe}^{3+}$ ,  $\text{Gd}^{3+}$ ,  $\text{Co}^{2+}$ ,  $\text{Mg}^{2+}$ ,  $\text{Fe}^{2+}$ ,  $\text{Cu}^{2+}$ ,  $\text{Al}^{3+}$ ,  $\text{Ni}^{2+}$ ,  $\text{Mn}^{3+}$  and  $\text{Cr}^{3+}$ . Ions such as,  $\text{Ni}^{2+}$  and  $\text{Mg}^{2+}$  show octahedral site preference. The Fig. 14 shows the cation site preference energy for various transition metals, and table 1 shows some ferrites and its cation distribution and its denotation: normal (N) or inverse (I).

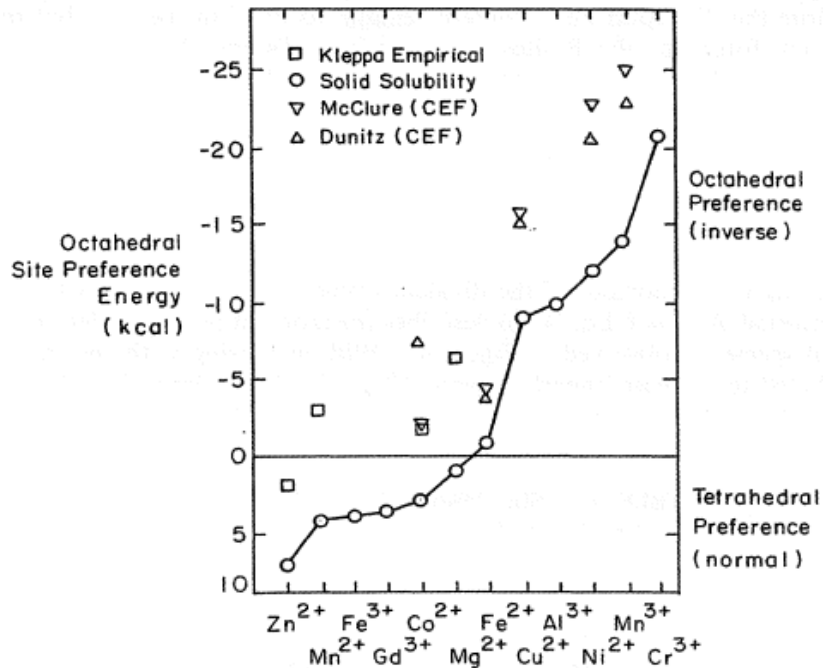


Figure 14: Cation site preference energy for various transition metal ions in A or B sites [84]

**Table 1: Crystallographic parameters of some spinel ferrites. N: Normal, I: Inverse and M: Intermediate [73]**

Ferrite	Lattice Parameter (Å)	Cation Distribution*	Density (g/cm <sup>3</sup> )
Fe <sub>3</sub> O <sub>4</sub>	8.398	Fe <sup>3+</sup> [Fe <sup>2+</sup> Fe <sup>3+</sup> ] (I)	5.193
CoFe <sub>2</sub> O <sub>4</sub>	8.381	Co <sub>x</sub> Fe <sub>1-x</sub> [Co <sub>1-x</sub> Fe <sub>1+x</sub> ] (I) 0.07 < x < 0.24	5.924
MnFe <sub>2</sub> O <sub>4</sub>	8.525	Mn <sub>1-x</sub> Fe <sub>x</sub> [Mn <sub>x</sub> Fe <sub>2-x</sub> ] (M) 0.07 < x < 0.23	4.94
NiFe <sub>2</sub> O <sub>4</sub>	8.337	Fe[NiFe] (I)	5.38
CuFe <sub>2</sub> O <sub>4</sub>	8.382 (cubic)	Cu <sub>0.33</sub> Fe <sub>0.67</sub> [Cu <sub>0.67</sub> Fe <sub>1.33</sub> ] (M)	5.39
ZnFe <sub>2</sub> O <sub>4</sub>	8.443	Zn[Fe] (N)	5.32
MgFe <sub>2</sub> O <sub>4</sub>	8.372	Mg <sub>x</sub> Fe <sub>1-x</sub> [Mg <sub>1-x</sub> Fe <sub>1+x</sub> ] (I) 0.14 < x < 0.26	4.53

A remarkable feature of Spinel is that all exchange integrals  $J_{AA}$ ,  $J_{AB}$  and  $J_{BB}$  are negative. This fact, favors antiparallel alignment of the spines connected by the interaction. Thus of all the interactions mentioned above, the  $AB$  interaction is the strongest, such that  $A$  spins are parallel to each other and  $B$  spins are parallel to each other, in a such way that the  $A$  spins may be antiparallel to  $B$  spins. The exchange integral will be ferromagnetic if  $J$  in the Eq.24 is positive. Otherwise, it will be antiferromagnetic if  $J$  is negative.

$$U = -2JS_i \cdot S_j \quad (24)$$

As the ferrites are ionic compounds, its magnetic properties are due to the magnetic ions that they contain. If we are interested in knowing what magnetic moment a particular metal ion should have, we can use the Hund's rule. It states that the spins in a partly filled shell are arranged so as to produce the maximum spin unbalance consistent with the Pauli exclusion

principle. Moreover, Hund's rule can be stated in terms of spin alone, because the orbital contribution is unimportant in ferrites [73].

## **2.8. Superparamagnetism**

We saw earlier that if the size of the particle of a magnetic material is below a certain critical size, then the magnetic material can only acquire a single domain. If the size is reduced even further, the magnetic anisotropy energy goes down and may become as low as to be comparable to or even lower than the thermal energy. This implies that the barrier energy for magnetization reversal may be thermally overcome and the magnetic moment will thermally fluctuate like a single spin in a paramagnetic material. This describes the phenomenon known as superparamagnetism, namely, a state where the spins within a single-domain particle remain magnetically coupled to each other, thereby allowing the formation of a "superspin" with relative enormous moment per particle. [80]. This concept was originally advanced by Néel to explain the possibility of thermal fluctuations in single domain ferromagnetic clusters and subsequently, Bean and Livingston and Jacobs and Bean [69] reviewed the problem in great detail, and showed that if a single domain cluster is small enough, then the presence of thermal energy becomes an important consideration, since,  $kT$ , energy can act to randomize the clusters with respect to a magnetic field,  $H$ .

Other characteristic of superparamagnetism is related to relaxation time ( $\tau$ ). The actual magnetic behavior depends on the value of the measuring time ( $t_m$ ) for a particular experimental technique. In bi-stable system, the probability for such magnetic moment thermally overcoming energy barrier is proportional to Boltzmann factor, as derived by Néel [80] as:

$$\tau = \tau_0 \exp\left(-\frac{KV}{k_B T}\right) \quad (25)$$

In this equation,  $\tau_0$ , is an attempt frequency factor equal to approximately  $10^{-9}$ s, and depends on several factors such as temperature, gyromagnetic ratio, magnetic field, magnetization, particle size, and damping constant, and yet is treated as a constant [85]. If the measurement (with a given temperature) in the time is much longer than relaxation time, the moment is rapidly relaxed by thermal fluctuations, and consequently the entire system is in superparamagnetic state. On the other hand, the moment relaxes so slow that it seems to be blocked. The blocking temperature is defined as the temperature at which the magnetic moment relaxation time is equal to the measurement time, or the temperature where the moment is able to overcome the energy barrier into the superparamagnetic state at a certain measurement time. Some typical instrument measurement times are 100s for DC SQUID,  $10^{-7}$ - $10^{-9}$ s for Mossbauer spectroscopy, and  $10^{-8}$  to  $10^{-12}$ s for neutron diffraction, respectively [85].

### 3. EXPERIMENTAL PROCEDURES

#### 3.1. Sample preparation

The samples were prepared using stoichiometric mixtures of hematite  $\alpha$ -Fe<sub>2</sub>O<sub>3</sub> and zinc oxide (ZnO) both from Alfa Aesar (99% or better) in a ratio molar from 1:1. This informed the amounts of precursor powders that were measured and loaded in vials for Pulverisette 4. The following equation shows the chemical reaction scheme leading to the formation the zinc ferrite.



The ball milling with the pulverisette-4 was carried out by setting a rotation speed of 1400 rpm for the main disk, and 450 rpm for the secondary disk rotating in the opposite direction. 17 tempered steel grinding balls of 10 mm in diameter were used. The milling was stopped each 5 hours to remove sample from the milling jars which were subsequently housed in glass container. This process was carried out for all three syntheses with BPR of 10:1, 20:1 and 40:1. For syntheses with BPR of 20:1 and 10:1 it was necessary to mill the materials until 50h and 60h respectively to reach the stage where the Mössbauer spectra showed non-magnetic peaks of the samples in contrast to the synthesis with BPR 40:1 where similar state or comparable state of the sample was achieved after 10h. However, the milling was stopped until 35h hours to study the behavior of the samples after this stage was achieved. After ball milling all samples, they were characterized by XRD, VSM and Mössbauer measurements. In the following section we will describe each of these techniques employed to carry out the measurements, as well as the theoretical foundations related to each technique.

### **3.2. High Energy Ball Milling (HEBM)**

The planetary ball mill owes its name to the planet-like movement of its vials. These are arranged on a rotating support disk and a special drive mechanism, which causes them to rotate around their own axis. The centrifugal force produced by the vials rotating around their own axis and by the rotating support disk, both act on the vials contents, consisting of material to be grounded by the grinding of the balls. The figure 15 shows the schematic depiction of the ball motion inside the ball mill.

Mechanochemical synthesis of materials is the general name given to the process of milling of materials powders involving chemical reactions occurring during the milling process or action. To realize the milling, different types of high-energy milling equipment can be used to produce mechanically alloyed powders. These may differ in their capacity, efficiency of milling, and additional arrangement for cooling, heating, etc.[29]. In our case, a Pulverisette-4 mill, commonly referred to as P-4 was used. This is shown in Fig. 15. The P-4 consists of both a main and a secondary disk. On the secondary disk, two vials are placed and the secondary disk can rotate clockwise, counter clockwise or just free rotation manipulated by the main disk. Moreover, the main disk always rotates clockwise and the secondary plate rotates as a function of the rate of the main disk. This rate is known as R-ratio [83].

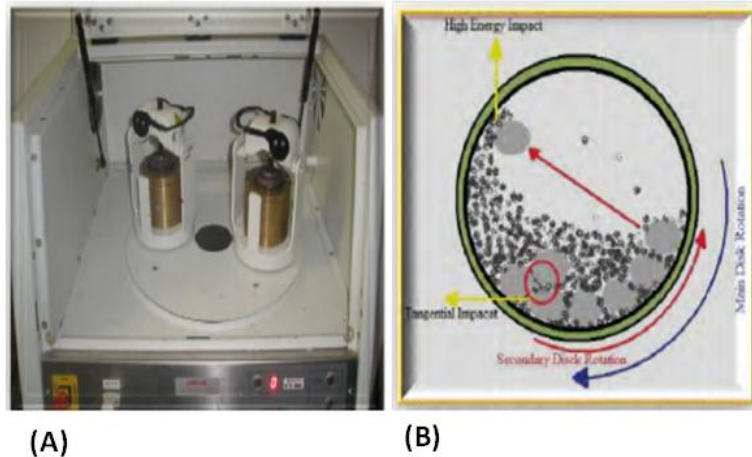


**Figure 15:** (A) Fritch Pulverisette-4 with the two special made brasses cans . (B) Milling ball action on grinding [83]

By varying the ratio between the rotation speed of the vials and the rotation speed of the disc, it is possible to control the movements and trajectories of the balls. This has allowed the creation of various models to describe the trajectories of the balls that can be found in the study of Jean and Nachbaur [28]. In this study, we can read that the milling governing factor is the injected power, and, that the shock power increases as a function of the vial and disc rotation speeds. The impact force generated in these movements can be tangential or centrifugal. The centrifugal force is present when the rotation of the secondary disk is clockwise; in this case the balls stay around the inner walls while the predominant impact of the ball is the centrifugal impact. When the secondary disk rotates counterclockwise the ball moves around the inner walls of the jar and jump side to side within the jar.

It is important to note that during ball milling the powder particles are repeatedly flattened, cold welded, fractured, and re-welded. Whenever two balls collide, some amount of powder is trapped in between them (See Fig. 16). The force of the impact plastically deforms the powder

particles, leading to work hardening and fracture. This process enables the particles to weld together and this leads to an increase in the particle size depending on the type of material under milling, and , the extent of the milling in terms of time from the start of the process [14],[29].

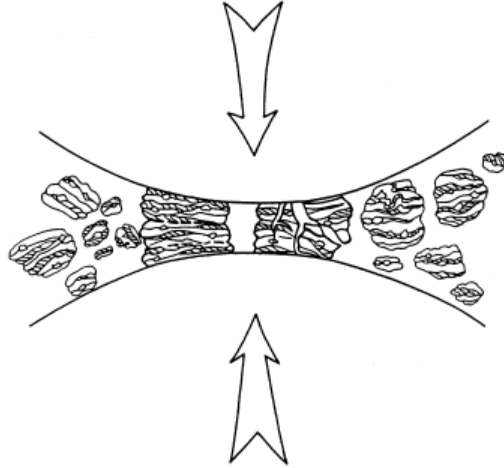


**Figure 16: Ball-powder-ball collision of powder mixture during mechanical alloying [29]**

### **3.3. X-Ray Diffractometry**

X-ray diffraction is a technique for the investigation of the internal atomic arrangement of the materials. This technique had its beginnings in von Laue's discovery in 1912 that crystals diffract x-rays, thereby revealing the structure of the crystal. At first, this technique was used for the determination of crystal structure. Later on, however, other uses were developed, and today, the method is applied to structural determination as well as diverse problems as chemical analyses and stress measurements, to the study of phase equilibrium and measurement of particle sizes, to the determination of the orientation of one crystal or the ensemble of orientations in a polycrystalline aggregate [74]. Below, we are going to describe the most important concepts related to this technique.

### 3.3.1. Bragg's Law

This law allows us to relate the distance between a set of planes in a crystal, and the angle at which these planes will diffract X-rays of a particular wavelength. Bragg showed that the scattering process can be visualized as if the X-ray were “reflecting” from the imaginary planes defined by Miller indices.

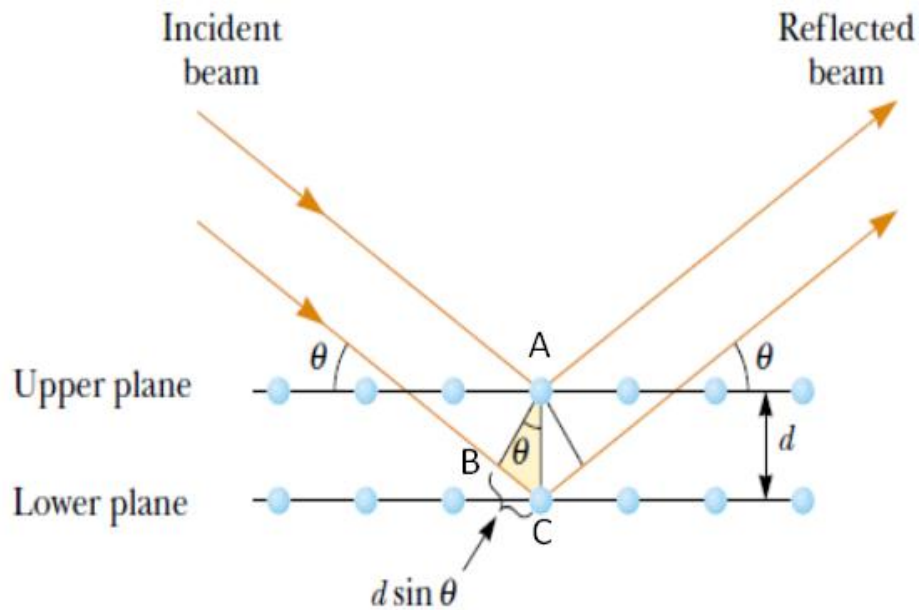


Figure 17 : Diffraction of X-rays from the planes in a crystal [84].

The above figure shows a scheme that can demonstrate Bragg's law. We suppose that X-ray incident from the left on a set of atomic planes of indices  $(h, k, l)$  and making an angle  $\theta$  with them. Constructive interference will occur when, for example, two waves, come out in phase. This implies that the path difference between the two waves is an integer multiple of wavelength  $\lambda$ . According to the geometry of the figure 17, it means that a reflected ray from the lower plane

will travel an extra distance BC compared with a reflected ray from the upper plane. Therefore, the effective path difference between the two beams is  $2d\sin\theta$ , and we can write Bragg's law as:

$$n\lambda = 2d\sin\theta \quad (27)$$

If we divided both side of this equation by,  $n$ , and, we defined,  $d/n = d_{hkl}$ , Bragg' law could then be re-expressed as [72]:

$$\lambda = 2d_{hkl}\sin\theta \quad (28)$$

In the original form of Bragg's law according to Eq. 4.2, we consider first order ( $n = 1$ ) or second order ( $n = 2$ ) diffraction from any plane, while with the last equation, we consider all diffraction to be first order from each of the family of planes in the crystal [72]. We can also see Bragg's law when  $\lambda$  is known, and,  $\theta$  is measured; that we can determine the interplanar distance,  $d_{hkl}$ , which one can find the dimensions of the unit cell.

### 3.3.2. Crystal size

When we defined Bragg's law, we saw that, when the diffraction occurs, the distance between adjacent planes, the distance ABC, must exactly equal to  $1 \lambda$ . In general this condition means that the distance between the first plane and a lower laying plane must be  $n \lambda$ . If the incident angle  $\theta$  is increased, so that distance ABC becomes  $1.1\lambda$ , then the extra distance travelled for the incident beam will be  $2.2 \lambda$  for the second deepest plane. The scattered waves from the sixth deepest plane plane will be  $6.6 \lambda$  and will therefore be exactly out of phase ( $0.5 \lambda$ ), with the ray

scattered from the first plane. In a similar way, the scattering from the second and seventh planes will be exactly out of phase. This means that when all planes of the unit cell are considered, no net scattering will occur.

If we set  $\theta$  closer to the Bragg angle, namely, the path difference between the first and second plane is closer to  $\lambda$ , the number of deepest planes necessary to cancel the scattering from the first plane with any other ones becomes bigger. If the crystal is only of a few angstroms in size, then the number of plane necessary to cancel scattering from, for example, the first deepest plane cannot be present. When this occurs the diffraction peak begins to show intensity at lower  $\theta$  and ends at an angle higher than the Bragg angle. This is the source of the 'particle size broadening' of diffraction lines [72].

The crystallite size broadening of a peak can be determined via Scherrer's equation, which is given by:

$$d = \frac{0.9\lambda}{B \cos \theta_B} \quad (29)$$

Here,  $d$ , denotes the crystal size and  $B$  is usually measured, in radians, at an intensity equal to the half of the maximum intensity, and this measure of width is commonly known as the full-width at half maximum (FWHM).

Our X-ray measurements were carried out with a Siemens D500 diffractometer with a  $\text{CuK}\alpha$  source of  $1.5418 \text{ \AA}$ . The parameters utilized were a step of  $0.02^\circ$  for 1seg per point and measured in the  $2\theta$  range from  $10^\circ$  until  $90^\circ$  for all samples. The figure 18 shows the equipment

that we utilized to make these measurements. The crystal size was determined utilizing the Scherrer's equation.



**Figure 18: Siemens D500 diffractometer, taking of [81]**

### **3.4. Vibrating Sample Magnetometry (VSM)**

The vibrating sample magnetometer is an apparatus that measures the magnetic field produced by a magnetized body. A scheme of this apparatus is shown in the Fig. 19. The sample S is oscillated vertically in a region of uniform field. If the sample is driven by a loudspeaker mechanism, the frequency is usually near 80Hz and the amplitudes are 0.1-0.2mm. The AC signal induced in the pick-up coil by the magnetic field of the sample is compared with the signal from a standard magnet M, and converted to a number proportional to the magnetic moment.

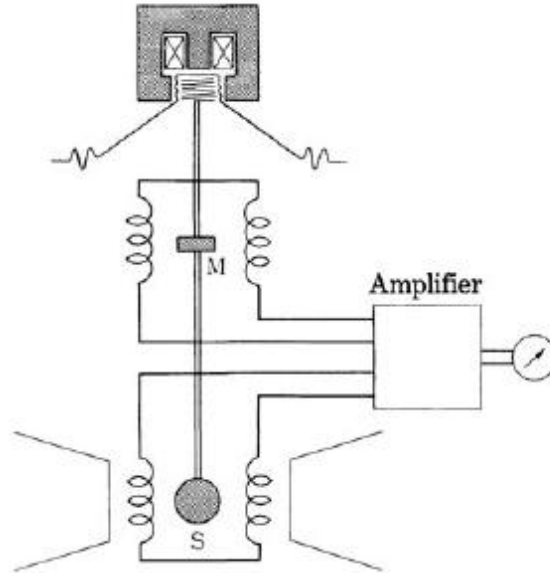


**Figure 19: vibrating sample magnetometer (VSM) [78]**

The sample, usually in the form of a small disk, is attached to the end of a nonmagnetic rod, the other end of which is fixed to a loudspeaker cone or to some kind of mechanical vibrator. The VSM is very versatile and sensitive, and it may be used for both weakly and strongly magnetic substances, with standard versions able to detect a magnetic moment of about  $10^{-5}$  emu = erg / Oe or  $10^{-8}$  Am<sup>2</sup>. This corresponds to the saturation magnetization of about 0.04 μg of iron [73].

The magnetic properties such as magnetization, coercivity, and loop hysteresis were performed, similarly as was carried out by Cedeño-Matei [89] by utilizing a lakeshore 7400 series VSM operated at a maximum magnetic field of 2.2 T, with a magnet gap of 0.9 in, which is shown in the Fig. 20.



**Figure 20: lakeshore 7400 series Vibrating Sample Magnetometer (VSM) taken from [81].**

### **3.5. Mössbauer spectroscopy**

Mössbauer spectroscopy is an analytical technique which was developed by using  $\gamma$ -ray nuclear resonance fluorescence, or the Mössbauer effect [75]. This effect was discovered by Rudolph Mössbauer in the works developed in the years 1955 to 1958 at the Max Planck Institute in Heidelberg, which finally led to the establishment of the field of recoilless nuclear resonance absorption. Later he was awarded with the Nobel Prize in 1961 for this discovery. Starting approximately in 1963 some chemists realized the potential of this new technique being applied to the study of chemical bonding, crystal structure, electron density, ionic states, and magnetic properties, [75]. Moreover, Mössbauer spectroscopy is used to determine the magnetic order,

hyperfine parameters such as internal magnetic field, quadrupole shift, and isomer shift of the various atomic-sites of Mössbauer nucleus. In relation to the distinguished power of the Mössbauer spectroscopy in resolving the differences in the different Fe-sites, this technique is particularly useful in our study, since we can determine the following: (1) the distinction between Fe in the tetrahedral and octahedral sites, (2) the cationic distribution, (3) the direct monitoring of reaction evolvments, and (4) super-paramagnetic phenomena enunciated with particle size at any given temperature. Within the application to material studies we can find that Mössbauer spectrometry is used to analyze: meteoritic Iron minerals, hemoglobin: paramagnetic effects, studies of rare-earth intermetallic compounds [68] and other more that we can find in the series of text about the symposiums on Mössbauer spectroscopy edited by Gruverman [67], [70].

### 3.5.1. Natural Line Width

The natural linewidth of an absorption line reflects a fundamental quantum property of incoming radiation. The uncertainty in the energy is related to the uncertainty in the lifetime of the excited state by Heisenberg's relation thus:

$$\Delta E \Delta t \geq \hbar \quad (30)$$

Here,  $\Delta E$  is the uncertainty in energy and  $\Delta t$  the interval available to measure the energy  $E$ . This time is of the order of the mean life  $\tau$  of the state under consideration. Setting  $\Delta t \approx \tau$ , we get the approximate width  $\Gamma = \Delta E$  of the level

$$\Gamma = \frac{\hbar}{\tau} \quad (31)$$

The last relation gives us the approximate width of energy range on which the energy  $E$  of an energy level is spread. We are going to assume that the energy of a particular state is given by  $E_0$ . The spectral line has a lorentzian profile centered on  $E_0$  with intensity  $I_0$  and full-width half-maximum (FWHM)[33].

$$I = \frac{I_0 \left(\frac{\Gamma}{2}\right)^2}{(E-E_0)^2 + \left(\frac{\Gamma}{2}\right)^2} \quad (32)$$

This relation was derived by Weisskopf and Wigner [86].

### 3.5.2. Recoil Energy Loss

In this section we consider one of the two most important aspects of the Mössbauer effect, which does reference a recoil energy loss and the section number 3.5.4., we are going to refer to the Doppler broadening that is considered of the most important aspect to produce Mössbauer effect.

When nucleus emits a gamma ray, in general, there will be recoil energy loss  $R$ . To calculate  $R$ , we assume that the photons are emitted by a nucleus of mass  $M$  that is at rest before the decay. Considering momentum conservation, and assuming that the nucleus is very heavy, it is, when their rest energy is compared to the decay energy  $E_0$ , that we can use non-relativistic approximation to connect the magnitude of momentum with the recoil energy  $R$ , namely:

$$R = \frac{p_{nucleus}^2}{2M} E_0 \quad (33)$$

As R will be smaller compared to  $E_0$ , we can set  $E_{photon}=E_0$  and, utilizing momentum conservation and the momentum of photon, we get the next relation

$$R = \frac{E_0^2}{2Mc^2} \quad (34)$$

With the last equation, R can be calculated for a given decay energy  $E_0$  and a given nuclear mass M.

### 3.5.3. Resonance and Resonance Fluorescence

In excitations of atomic or nuclear levels, the term resonance implies large cross section and this occurs when an incident gamma ray has the energy  $E_0$ . If the nuclei in the resonator are identical to the radioactive source, we expect that the photons are resonantly absorbed and that they excite the resonator nuclei into level B. Once excited, the nuclei will decay again with the reemission of gamma rays of energy  $E_0$ . The complete process is called nuclear resonance fluorescence [75]. In the Fig. 21 is shown a scheme of resonance absorption.

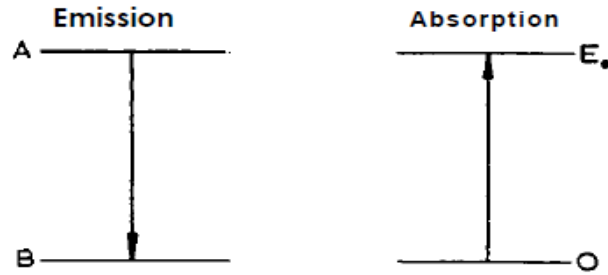
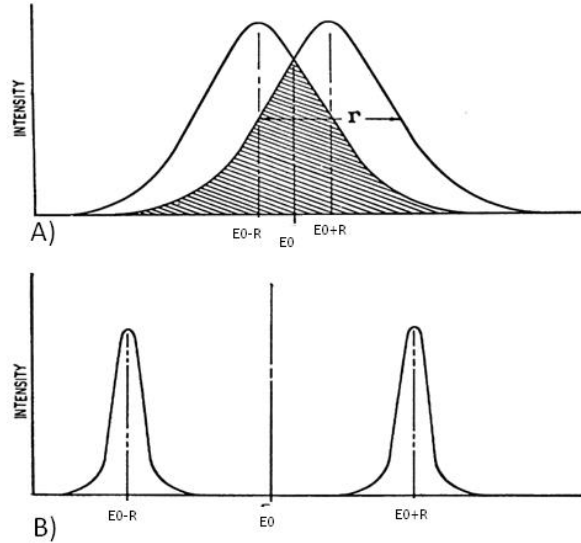


Figure 21: scheme of resonance absorption[34]

In this transition, however, not all of the energy goes into the photon, because some of this energy is lost to recoil of the emitter. Likewise, when a photon is absorbed, the absorber will recoil and the distributions of the emission and absorption energies are therefore separated by twice the recoil energy. The probability of resonant absorption is proportional to the overlap of these distributions. In the case of atomic transitions, there is a high probability of resonant absorption because, in this case, the recoil energies are small compared with natural widths. In contrast, for nuclear transitions, photon energies are much higher and recoil energies are much larger than the natural line width. This implies no overlap of transition energy probabilities (see Fig.22). This means that resonant absorption is not very probable for nuclear transitions [35].



**Figure 22: relation of line width, transition energy and recoil energy. (A) Overlap (schematic) of emission and absorption lines in optical transitions. (B) Absence of overlap of emission and absorption lines in nuclear transitions involving atoms free to recoil [75]**

### 3.5.4. Doppler Broadening

We know that atoms in a gas or a solid are not at rest, and that at room temperature their velocities reach values of several hundred m/s. These speeds lead, to a Doppler broadening. For a gamma ray emitted, if the source is moving with velocity component  $v_\gamma$  in the direction of emission, its energy is shifted by an amount

$$\Delta E = \frac{v_\gamma}{c} E_0 \quad (35)$$

In a gaseous source the velocity of the emitting atom will be directed at random with respect to the direction of the source resonator. The velocity along the direction of emission will therefore

vary from  $\nu_0$  to  $-\nu_0$ . This leads to observe a broadening in the line shape from a large number of decaying atoms. This broadened is given by [75]:

$$D = 2 \frac{\nu_0}{c} E_0 \quad (36)$$

This broadening implies a reduction in emission and absorption line height. When this reduction is of the same order as  $R$ , emission and absorption lines overlap somewhat and a small amount of resonance fluorescence is expected. The reduction in the line height is given by the factor

$$\frac{\Gamma}{D} \quad (37)$$

This reduction drastically affects the number of observed fluorescence photons [75]. But R. Mössbauer discovered, by his study in nuclear resonance at low temperature, that it was possible to observe nuclear resonance fluorescence with non-broadened lines. In Fig.22 (A) and (B), we can observe as the emission and absorption line overlap and also as the recoil energy loss affects the resonance fluorescence, respectively.

### **3.5.5. Recoil-free Emission of gamma ray**

Based in the two precedent sections, we can see the importance of gamma rays without Doppler broadening and without recoil energy loss, to observe Mössbauer effect. To show this fact we consider transition from the first excited to the ground state in two different isotopes of iron. If the two parents nucleus,  $^{57}\text{Co}$  and  $^{58}\text{Co}$ , are embedded in an iron lattice, the following parameter are obtained for the two decays of the nucleus [75]

**Table 2: Parameter for the two decays from the first excited to the ground state in two isotopes of iron [86]**

Decay energy	$^{57}\text{Fe}$	$^{58}\text{Fe}$
		14 Kev
$R$	0.002 ev	6 ev
$E_E$	0.04 ev	0.04 ev

To  $^{57}\text{Fe}$ , the 14-Kev transition is emitted without recoil. Also, we see that  $R$  is much smaller than  $E_E$  (Einstein energy). In this case the gamma ray escapes with the full energy  $E_0$  and therefore, it is not Doppler broadened, because it comes from thermal excitation of the solid, and for this case, the gamma ray scapes without changing the internal energy of the solid and hence has the natural line width. As the minimum amount of energy that the solid can accept is  $E_E$ , and to  $^{57}\text{Fe}$ , we have that  $R \leq E_E$ ,  $R$  is not accepted by the solid. For the 800- Kev the situation is different because in this case  $R$  is very large compared to  $E_E$ . In this situation, the solid is excited very highly and the discrete Einstein levels overlap. Therefore the solid can accept a particular recoil energy  $R$  while the iron nucleus can emit its photon as if it were free, and so this manner of energy loss and Doppler broadening of the photon line due to vibrating of the atoms in the solid occurs. Classically, it can occur that the gamma ray escapes without energy loss (in this case  $R \leq E_E$ ) and if  $R \geq E_E$ , recoil energy loss can occur. Quantum mechanically, however, there is still a small probability that the gamma ray excites the solid even if ( $R \leq E_E$ ) [75].

As the energy levels of the nucleus are dependent on a number of external factors, it is possible to obtain information about the atomic and molecular structure of materials from their Mössbauer spectra. Depending on the nature of the interaction, there may be a resulting split or

shift of nuclear energy levels. This allows us to study properties such as, isomer shift, magnetic splitting, and the electric quadrupole coupling. In the next sections, we will give a brief description of each one.

### 3.5.6. Isomer shift

The isomer shift involves a differing change in the size associated with nuclear energy levels resulting from electron charge densities at the nucleus which differ for the emitting and absorbing materials. The origin of the isomer shift  $\delta$  is the result of the Coulomb interaction of the nuclear-charge distribution over a finite nuclear radius  $R$  in the excited and ground states, and, the electron-charge density at the nucleus (electrons) [76]. The  $s$  electron density of the resonating nuclei in the source and the absorber can be varied by the chemical environment. By Coulomb interaction, the levels of the ground and of the excited state are changed. Because the electron density of the nucleus is a function of the valence state and chemical bonding, the isomer shift is also sometimes called “chemical shift” or “differential chemical shift” [76].

### 3.5.7. Nuclear Zeeman Effect

The interaction of the nuclear magnetic dipole moment  $\mu$  with a magnetic field  $H$  at the sites of the nucleus, splits the nuclear state with spin  $I$  ( $I > 0$ ) into  $(2I+1)$  sublevels with eigenvalues

$$E_m = -\frac{\mu H m_I}{I} = -g_n \beta_n I \quad (39)$$

Where  $m_I$  is the magnetic quantum number with the values  $m_I = I, I-1, \dots, -I$ , while the nuclear magnetic moment is related to the nuclear Bohr magneton  $\beta_n$  by the nuclear Lande splitting factor  $g_n$  thus:

$$\mu = g_n \beta_n I \quad (40)$$

### 3.5.8. Quadrupole splitting

The quadrupole interaction is caused by an electric quadrupole moment in the atomic crystal lattice [33]. The ground state of the atom is not affected, but the first excited state is split into sublevels that correspond to different magnitudes of  $m_j$ . An energy diagram of combined Zeeman splitting and quadrupole-interaction is given in the figure Fig. 23.

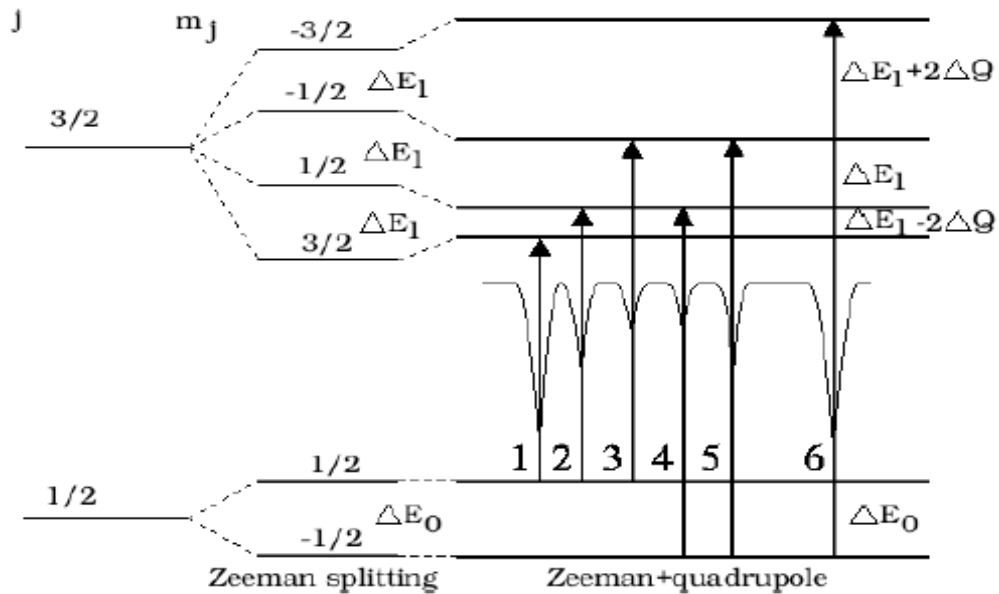


**Figure 23:** This Figure shows of left to right the energy levels diagram of the 14.4 KeV  $3/2 \ 1/2$  iron-57 transition, split by the Zeeman effect, altered by the electric quadrupole interaction. Taken of [33].

When there is net quadrupole moment,  $Q$ , the distribution of electric charge is either prolate (“cigar- shaped”) or oblate (“flattened”) and with the mean position of the charge remains at the origin but it is deformed. These permanent deformations, in atomic or nuclear systems, are caused by tensor forces, where the quadrupole moment of the nucleus is in general a nine component tensor [35].

## 4. MECHANOCHEMICAL SYNTHESIS OF $\text{ZnFe}_2\text{O}_4$ AS A FUNCTION OF “BALL TO POWDER RATIO” (BPR)

### 4.1. Mechanochemical synthesis of Zinc ferrite BPR=10:1

XRD measurements associated with the mechano-chemical syntheses of the  $\text{ZnFe}_2\text{O}_4$  from the ball milling of the powdered ZnO and  $\alpha\text{-Fe}_2\text{O}_3$  powder materials. It should be noted that processing-aiding agent, notably, (6ml) of acetone was added to the powder mixture before starting the jar before commencing the milling action. The effect of changing the ball-to-powder ratio (BPR) in the formation of  $\text{ZnFe}_2\text{O}_4$  will be presented for the 10:1; 20:1; and 40:1 cases respectively.

#### 4.1.1. XRD measurements

The powder patterns of unmilled mixture contain only the individual reflections of ZnO (PDF#98-000-0483) and  $\alpha\text{-Fe}_2\text{O}_3$  (PDF#98-000-0240) as shown in Fig.24. We can see in the Fig.24, that in the course of ball-milling of ZnO and  $\alpha\text{-Fe}_2\text{O}_3$  mixture, the formation of  $\text{ZnFe}_2\text{O}_4$  phase appeared after 5h of milling, as evidenced by the appearance of two peaks around approximately 35.5 and 62.3 ( $2\theta$ ) degrees, corresponding to the reflection (311) and (440), planes respectively. These reflections are characteristic of spinel phase [21][36]. It is also evident from the figure that some of ZnO and  $\alpha\text{-Fe}_2\text{O}_3$  materials phases remained until, approximately 40h of milling time after which reaction finished for 60h of milling. We can observe diffraction peaks broadening with the milling time. This broadening in the diffraction peaks of the milled materials can be the result of the reduced grain size, increase of structural defects and the atomic level strain introduced during the milling [36]. The XRD peaks for the  $\text{ZnFe}_2\text{O}_4$  were indexed based in the cubic structure for the spinel phase.

The average grain size was evaluated from the full width at half maximum of the reflection (311) (located at approximately  $(2\theta) = 35.4$  degrees) in the XRD pattern using the Scherrer's formula. The grain size was found to decrease with the milling time and reached an average size of 8.14 nm while it ranged between 6.75 - 15.40 nm corresponding to 60h and 5h of milling times, respectively. The particle size of ZnO and  $\alpha$ -Fe<sub>2</sub>O<sub>3</sub> were evaluated from FWHM of the reflection (103) and (104) respectively. In the Fig. 25 (B) we can note how the particle size of precursors decreased rapidly from 5h until approximately 20h of milling. After this time the particle size of both ZnO and  $\alpha$ -Fe<sub>2</sub>O<sub>3</sub> decreased slowly according the milling time evolved. The particle size of ball milled  $\alpha$ -Fe<sub>2</sub>O<sub>3</sub> phase reduced from 19.58 for 5h of milling time to 7.83 nm for the first 20h ball milling and after this time decreased slowly up 20h milling until finally reach a value of 6.19 nm. The ZnO phase decreased from 10.83 nm within 5h of milling time, until 8.01 nm within 15h of ball milling. After this time, similar as occurred with the  $\alpha$ -Fe<sub>2</sub>O<sub>3</sub> phase, the crystal size of ZnO decreased slowly until the 40h of ball milling. From the plot we can note that by increasing of milling time, the particle size of ZnFe<sub>2</sub>O<sub>4</sub> and precursor cannot be reduced further after 15h of milling time approximately.

The examination of the XRD spectra shown in figure 24 indicates that the mechanochemical reaction process occurred in a gradual progressive manner given that the spectra peaks for the precursor solid materials evolved at different rates, while the intensities of these peaks decreased continuously with increasing time of ball milling. From comparison with the unmilled or unreacted powder mixture, one can notice that the prominent ZnO peaks close to  $2\theta = 32^\circ$ , and the one at  $2\theta = 37^\circ$  were drastically reduced in intensities within the 5hours of ball milling. In general, the ZnO peaks at higher angles always decreased in intensities as well.

In contrast to the ZnO case, the peaks associated with the  $\alpha\text{-Fe}_2\text{O}_3$  did not evolve in the same manner. This is an indication that the mechanochemical synthesis commenced with the rapid decomposition of ZnO leading to the formation of metastable intermediate phases typified by the shifts of spectral peaks centered around  $2\theta = 32 - 33^\circ$  to higher angles. We can see this trend and we can attribute this fact, as was mentioned in experimental procedures that in high-energy milling the powder particles can repeatedly be flattened, cold welded, fractured and re-welded. These facts lead to an increase as well as a decrease in the crystal size [29].

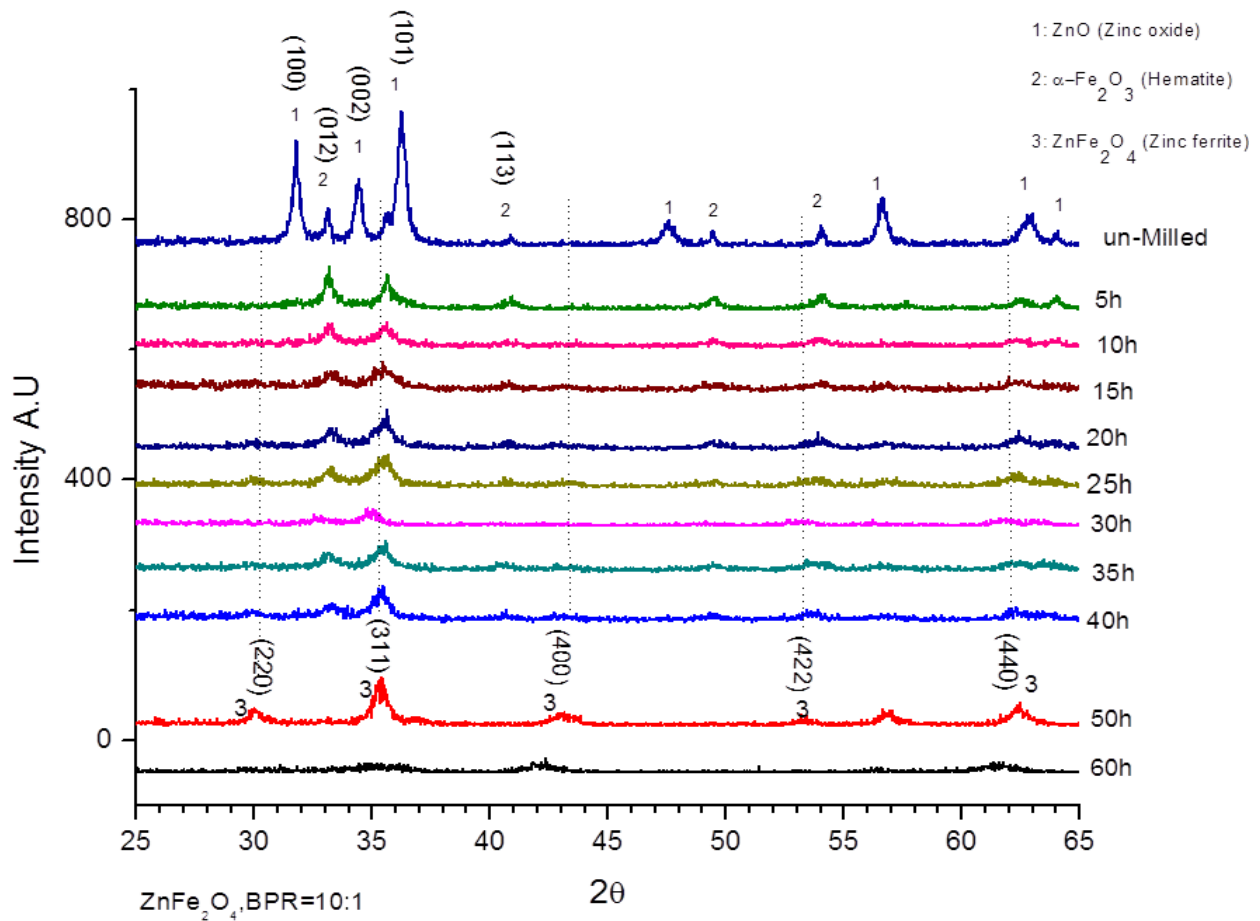


Figure 24: X-ray diffraction spectra of synthesis of  $\text{ZnFe}_2\text{O}_4$  by ball milling of  $\text{ZnO}$  and  $\alpha\text{-Fe}_2\text{O}_3$  as a function of time using a BPR of 10:1.

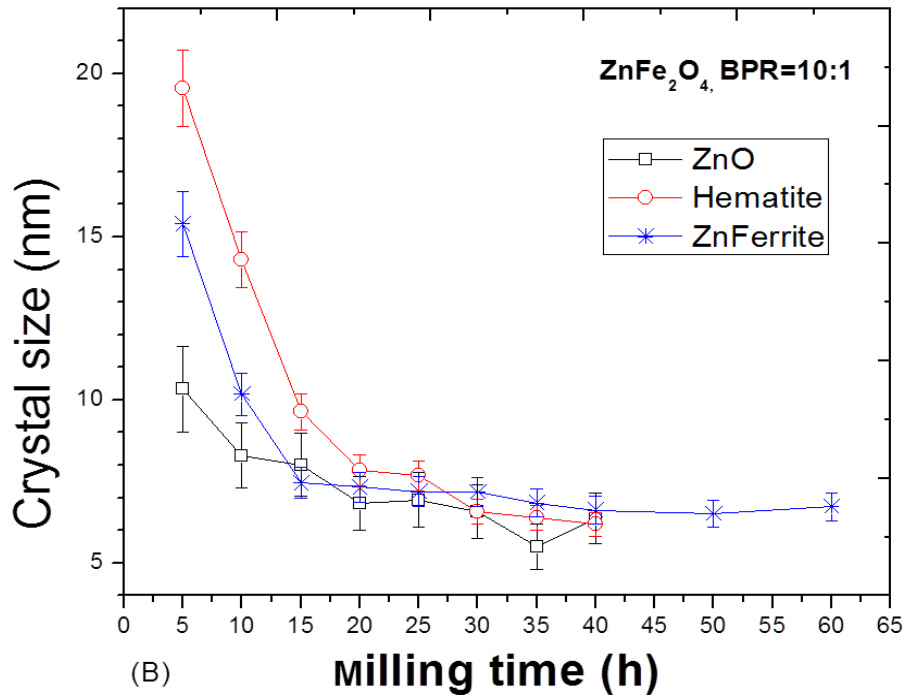
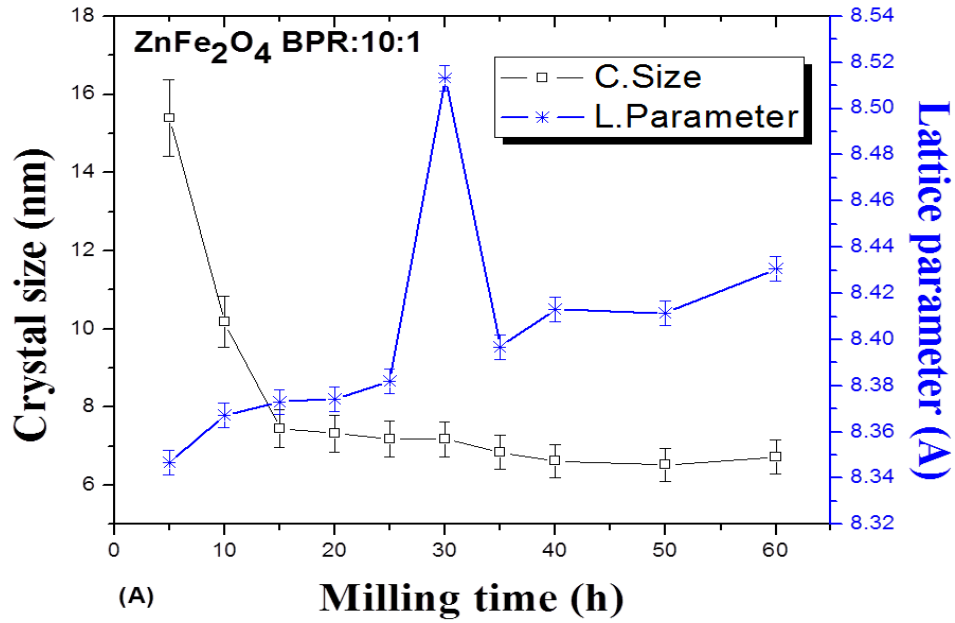


Figure 25: (A) Crystal size and lattice parameter of ZnFe<sub>2</sub>O<sub>4</sub> formed as a function of time during the ball milling of NiO, ZnO and  $\alpha$ -Fe<sub>2</sub>O<sub>3</sub> powder mixtures using a BPR of 10:1. (B) Evolution of crystal size of ZnO and  $\alpha$ -Fe<sub>2</sub>O<sub>3</sub> as function of milling time during Zinc ferrite formation.

The Fig.26 shows the variation of strain as a function of the milling time. We can observe that the strain increases from 5h of milling time until approximately 50h. For 60h, milled state the strain shows a slight decrease. From Fig. 24 we can observe how the diffraction peaks become broader compared to the unmilled state patterns. The broadening is due to the residual stress which produces a distribution of both tensile and compressive forces [72]. Further, On the peak-broadening we can observe how it increases significantly and this fact is due to the fact that the nanocrystalline particles contain a huge amount of lattice strain which arises from HEBM [21]. The average strain evolution with milling time is summarized in table 3, and it was calculated by means the equation 41, where B is the FWHM. [72]. Fig.25 (A) shows the variation of the lattice parameter with the milling time. This variation in the lattice parameter with increasing milling time is further attributed to the accumulation of lattice imperfections in the process of the continuous fracture and re-welding of grains under high-energy impact, as well as continuous redistribution of cations between tetrahedral and octahedral positions [21]. For average crystal size we can compare our data to those obtained by Ehrhardt et al [37], who studied the crystal size and lattice parameter for low energy milling (LEM) and high energy milling (HEM). For example, they obtained  $d = 18$  nm and  $a = 8.451 \text{ \AA}$  after 120h for LEM mode. On the other hand, they obtained  $d = 8$  nm and  $a = 8.462 \text{ \AA}$  after 12h for HEM mode. As can be observed, we obtained a slightly larger value for crystal size, but a slightly smaller value for the lattice parameter. The average lattice parameter was  $8.4008 \text{ \AA}$ , but it varied in the range  $8.421\text{-}8.528 \text{ \AA}$ , being in accord with the cited literature data. For example, our lattice parameter is slightly smaller than those reported by other methods such as micro-emulsion method[31], Hydrothermal synthesis[3] and by of rapidly quenched zinc ferrite[38]. The authors of the work reported above values of  $8.43$ ,  $8.435 \text{ \AA}$  and  $8.439 \text{ \AA}$ , respectively.

$$\epsilon_{str} = \frac{B}{4TAN\theta}$$

[41]

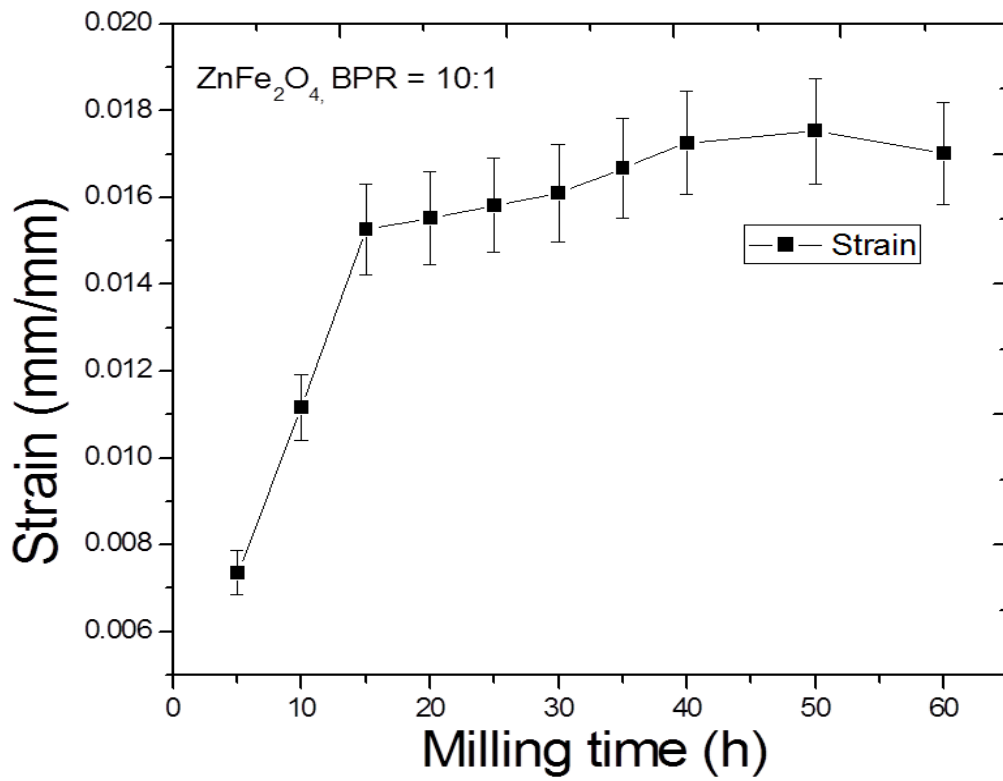


Figure 26: Strain as function of milling time to zinc ferrite synthesized by HEBM.  
BPR = 10:1

**Table 3: Crystal size, strain and lattice parameter of zinc ferrite synthesized by HEBM with BPR=10:1**

Milling time (h)	ZnFe <sub>2</sub> O <sub>4</sub> with BPR = 10:1		
	Crystal size* “ <i>d</i> ” (nm)	Lattice parameter (Å)	Average Strain (mm/mm) x 10 <sup>-3</sup>
5	15.40	8.3467	7.358
10	10.18	8.3671	11.164
15	7.45	8.3730	15.261
20	7.32	8.3742	15.535
25	7.19	8.3820	15.284
30	7.18	8.5132	16.097
35	6.84	8.3968	16.675
40	6.62	8.4132	17.258
50	6.52	8.4115	17.528
60	6.73	8.4305	17.023
Average	8.14	8.401	8.4008

\* Determined from (311) ZnFe<sub>2</sub>O<sub>4</sub> reflection with Debye-Scherrer formula.

#### 4.1.2. VSM measurements

Magnetic behavior of the soft ferrites samples synthesized by HEBM can be observed in the hysteresis loop shown in Fig. 27. Maximum magnetization and minimum coercivity were reached for the 50 and 40h of milling times respectively. The corresponding values for these times are 51.64 Am<sup>2</sup>/Kg and 1.40 mT. In general, for a homogeneous material phase, the coercivity should be decrease as particle or crystal size decreases until the characteristic superparamagnetic size limits are approached for ferrimagnetic materials. This trend would not be deduced based on measurements of coercivity for ZnFe<sub>2</sub>O<sub>4</sub> since in its pure form, it belongs to the subgroup of ferros spinels known as the normal types by virtue of its cationic distribution. Recall that the overall designation of ferros spinel materials in terms of their cationic distribution is denoted as  $(M_{1-\lambda}^{2+}Fe_{\lambda}^{3+})^{Tet}[M_{\lambda}^{2+}Fe_{2-\lambda}^{3+}]^{oct}O_4$  where,  $\lambda$ , refer to the degree of inversion, and outer bracket “*Tet*” and “*oct*” superscripts designations referring to the tetrahedral and octahedral sites of spinel phase. In this designation,  $\lambda = 0$ , such ferrite is known as Normal type, of which ZnFe<sub>2</sub>O<sub>4</sub> is a typical example. Thus, in an inhomogeneous phase material consisting of ZnFe<sub>2</sub>O<sub>4</sub>, the Zn<sup>2+</sup> cations would be in tetrahedral sites, while the Fe<sup>3+</sup> will reside into octahedral

sites exclusively. Therefore, from 40h of milling, it is possible that some distribution leading to some  $\text{Fe}^{3+}$  within the tetrahedral site or some  $\text{Zn}^{2+}$  within the octahedral site leading to the formation of non-completely normal  $\text{ZnFe}_2\text{O}_4$  is the reason for the increase of the coercivity despite that attainment of nanosize limits to yield superparamagnetic behavior that should yield zero coercivity.

It is instructive to make some comments concerning the overall trend observed in figure 25 (A) which showed the variation or evolution of the crystal size as a function of milling time, and the trend of coercivity from VSM measurements of Figure 28. Both materials properties displayed drastic reduction in values within the first 10 hours of ball milling, which were followed by vary slight variation until 40 hours of ball milling, after which the coercivity tended to increase to a value of  $49.60 \times 10^{-4}\text{T}$  at 60h of milling from the value of  $13.99 \times 10^{-4}\text{T}$  in the case of the 40h milled state.

The VSM plot for the 50h milled state, and the corresponding data analyses with the magnetization saturation or magnetic moment of  $51.64 \text{ Am}^2/\text{Kg}$  seemed to be extra-ordinary in comparison to the other plots with rather closely related overall behavior.

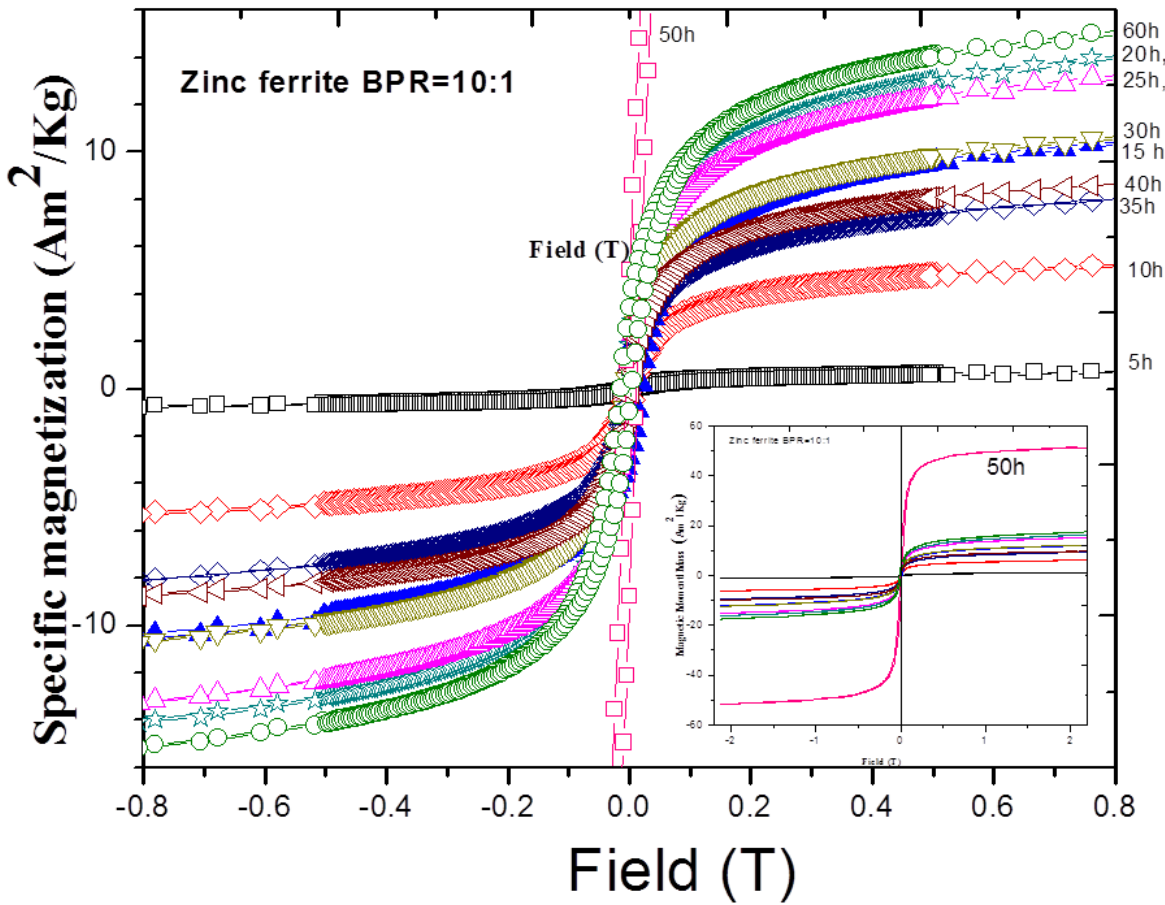


Figure 27: Hysteresis loop for the synthesis of Zinc ferrite with BPR=10:1.

On the other hand, magnetization increases with the milling time from 1.0210 until 16.122 Am<sup>2</sup>/Kg for 20h. After this time, it tends to decrease until 40h, reaching 9.8 Am<sup>2</sup>/Kg. For 50h of milling the magnetization reaches the maximum value mentioned above, and finally decreases. We can note that the magnetization behavior changes during the time and this can be due to a disruption of the magnetic Fe<sup>3+</sup> and Zn<sup>2+</sup> ions in the two sub-lattices. The table 4 shows the minimum and maximum values for coercivity and magnetization respectively.

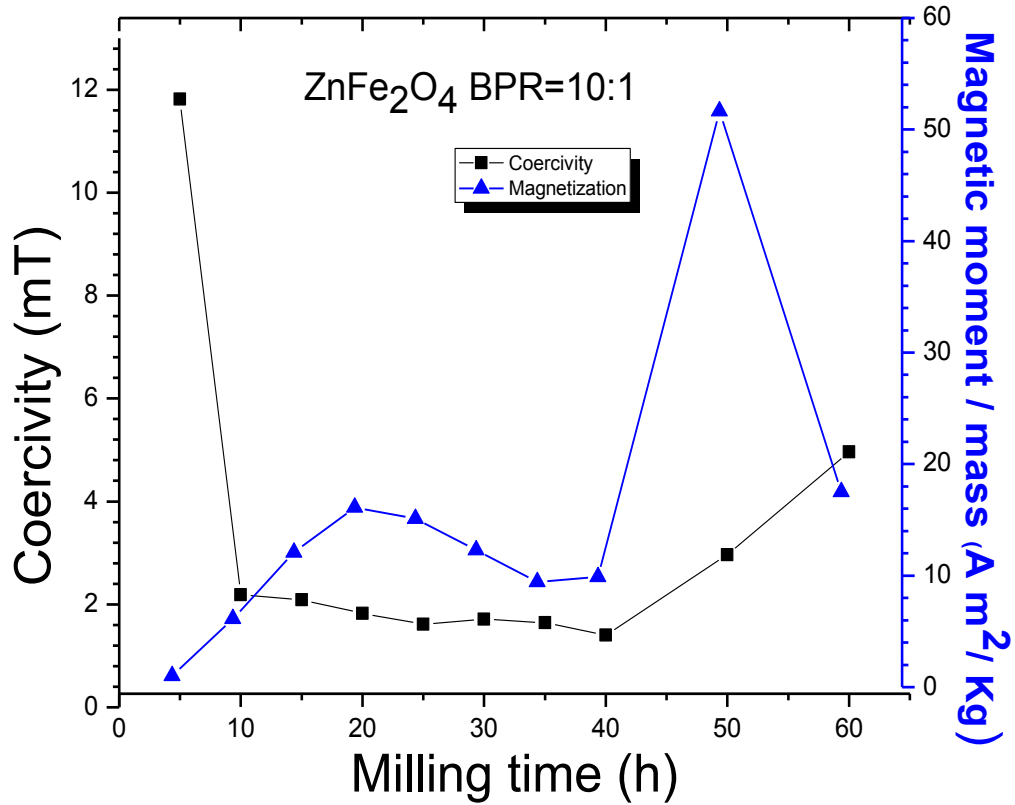


Figure 28: Coercivity size and Specific magnetization as function of milling time to  $\text{Ni}_x\text{Zn}_{1-x}\text{Fe}_2\text{O}_4$  with  $x=0$ , synthesized by HEBM and BPR=10:1.

Table 4: Values for coercivity and magnetization as a function of milling time for zinc ferrite with BPR=10:1

Milling time (h)	ZnFe <sub>2</sub> O <sub>4</sub> with BPR = 10:1	
	Coercivity (mT)	Saturation magnetization (Am <sup>2</sup> /Kg)
5	11.81	1.02
10	2.18	6.14
15	2.09	12.07
20	1.83	16.12
25	1.61	15.09
30	1.71	12.30
35	1.65	9.43
40	1.40	9.87
50	2.96	51.64
60	4.96	17.50

### 4.1.3. Mössbauer measurements

Room temperature Mossbauer spectra of the samples as a function of milling time are shown in the Fig.29. The five hours ball milled state is seen to be majorly consisted of prominent sextet peaks and weak or small intensity doublet peaks at the central portion of the spectrum. The spectrum background is seen to be flat, except in the middle portion where some broadening is displayed. The slight change observed in the middle portion due to the non-magnetic Fe sites for the 5 hours milled state, is increased in the 10 hours milled state. The sextet peaks remained prominent in comparison to the 5 hours milled state despite more broadening at the base of the sextet peaks.

The development of the central doublet assume an asymmetrical profile, with the Left Hand Side (LHS) peak being more intense in the 10 hours state, while almost equal in the 15 hours milled state. In the 15 hours milled state, the continued change of the relative intensities difference of the outer, middle and inner-most sextet peaks became less pronounced, appearing completely overturned from the 20 hours milled state, where the intensities of the sextet peaks appeared to be equal. While the intensities of the magnetically split sextet peaks diminished progressively with increased mechanochemical synthesis, the spectrum of the 50 hours milled state suggested that overlapping magnetically split peaks were not associated with the hematite precursor material. The LHS peak of the 50 hours ball milled state appeared more prominent than any other peak, while the 60 hours ball milled state spectrum showed only overlapping non-magnetically split sites in the central portion of the spectrum, with a fairly flat background.

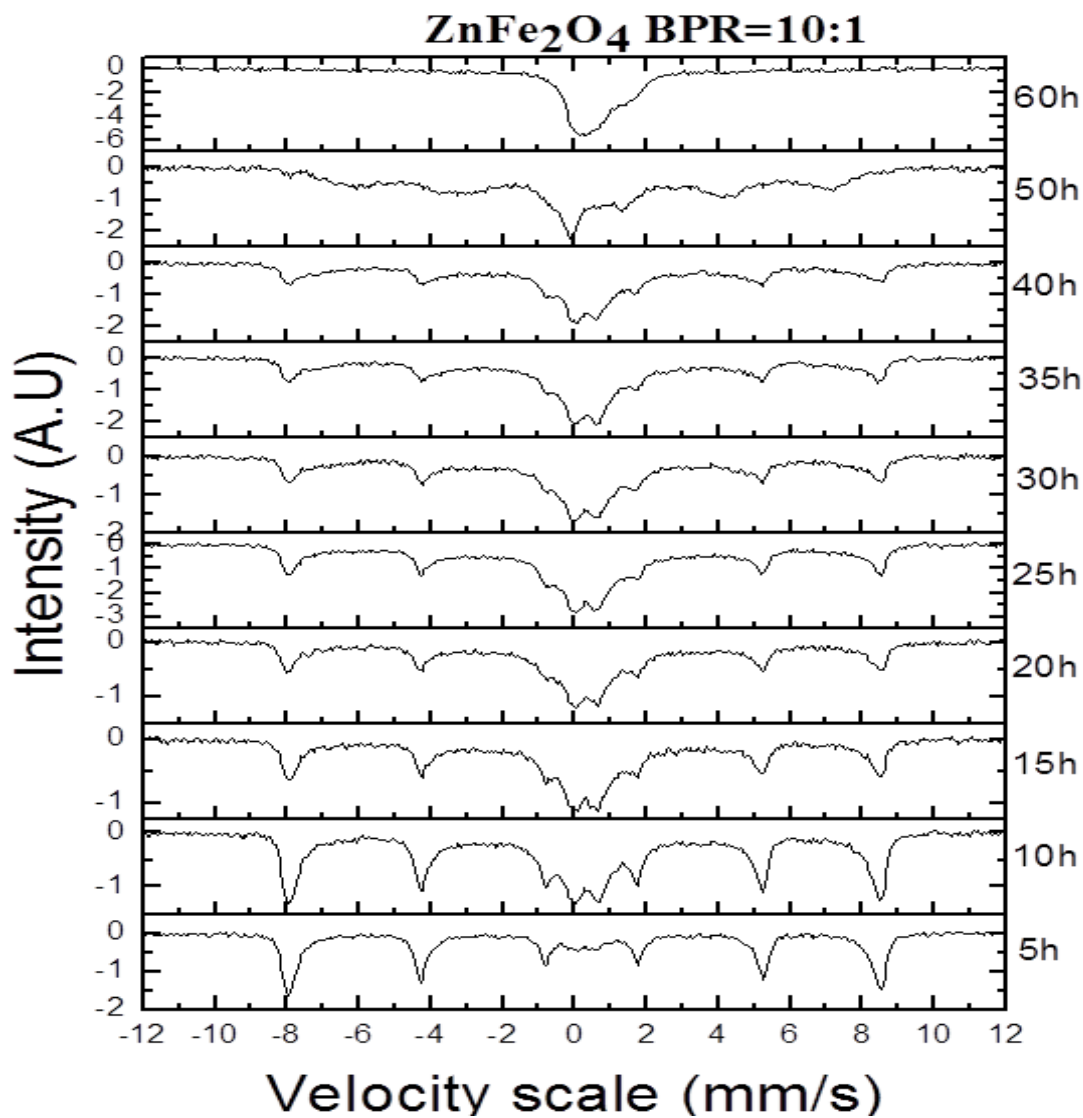


**Figure 29: Room temperature Mossbauer spectrum to zinc ferrite with BPR =10:1**

The spectrum for the 5h of milling time was fitted with a site whose internal magnetic field value was of 510.97 kOe, belonging to the hematite phase. The internal magnetic field varied from 510.97 kOe to 509.8 kOe, 509.36 kOe, 511.27 kOe, 509.5 kOe, 509.06 kOe, 508.77 kOe, 508.62 kOe, 512.44 kOe and 507.89 kOe, and relative abundance of 45.25%, 24.98%, 15.88%, 14.37%, 11.89%, 11.13%, 10.15%, 9.05%, 3.7% and 0.53%. The diminution in relative abundance

indicated that the mechanochemical synthesis process was progressive and its evolution as a function of milling time is depicted in the figure 30.

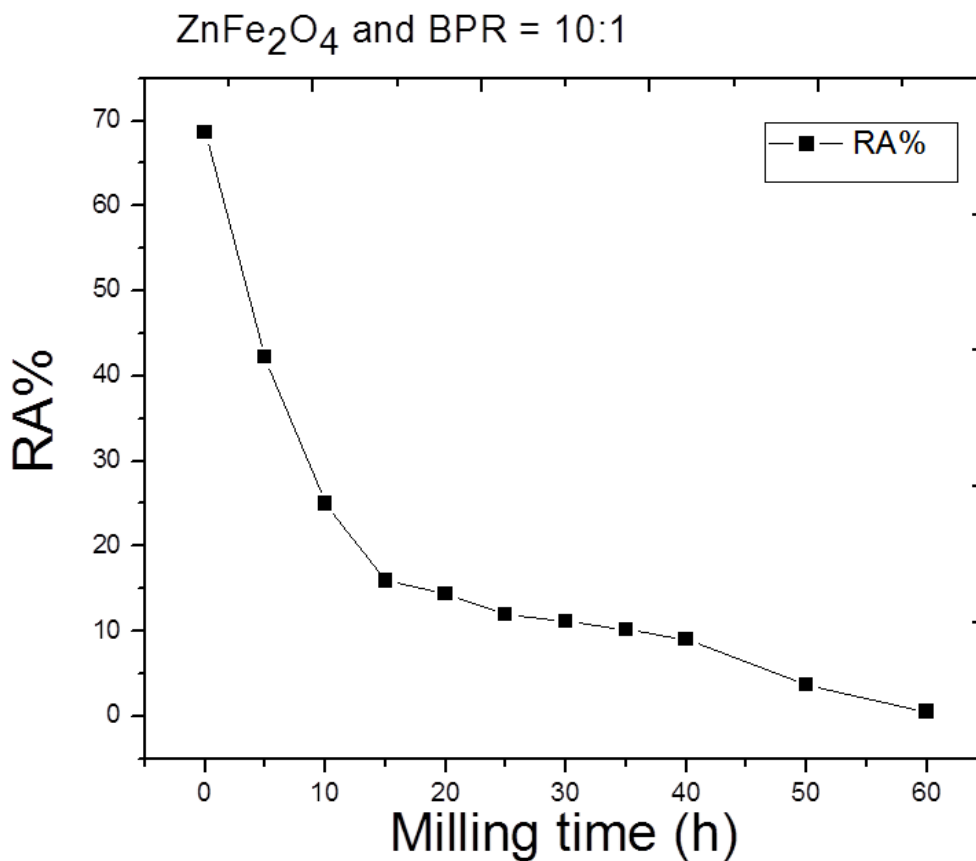


Figure 30: Relative abundance of hematite as a function of milling time during the synthesis of  $\text{ZnFe}_2\text{O}_4$  using a BPR of 10:1

## 4.2. Mechanochemical synthesis of Zinc ferrite BPR=20:1

### 4.2.1. XRD measurements

The XRD pattern of the un-milled mixture of solid precursors materials together with the spectra of the various milled states as a function of milling time are shown in the Fig. 31. As in the previous section, the average size of the nanoparticles were evaluated from the full width at half

maximum (FWHM) of the (311) reflection from the XRD pattern based on the Scherrer's equation. Close examination of the spectra displayed in figure 31, showed that both spectra peaks reductions and broadening occurred as a function of milling time. In addition, the shift of peaks positions occurred in relation to changes of lattice parameters of the various materials phases. The peaks corresponding to the ZnO phase (Identified as "1") being the most intense ones served to show how the ball milling process resulted in mechanochemical syntheses leading to the progressive and gradual formation of ZnFe<sub>2</sub>O<sub>4</sub> following the reaction scheme



The peak for ZnO labeled or identified as (101) exhibited the most dramatic reduction, and also, a noticeable shift in  $2\theta$  position towards the low angle side. Similarly, the peak identified as (100) with its drastic reduction also shifted to the low angle direction. This is an indication to the change of the lattice parameters as the ball milling action progressed.

The  $\alpha\text{-Fe}_2\text{O}_3$  spectral peaks also shifted in position towards the high angle direction. Since the spectral shift of ZnO and  $\alpha\text{-Fe}_2\text{O}_3$  were at variance to each other, we can then infer that structural deformation at the atomic scales are essential to the mechanochemical synthesis.

Ball milling action causes creation of atomic, linear, surface, and volume defects. The linear and surfaces defects (grain boundaries increases, stacking faults etc) serve to shorten diffusion pathways for Zn cations following the decomposition of ZnO to Zn<sup>2+</sup> and O<sup>-2</sup>, after which  $\alpha\text{-Fe}_2\text{O}_3$  transformation into Spinel cubic structure occurs. While the ZnFe<sub>2</sub>O<sub>4</sub> formed exists in

metastable state due to the high level of structural defects, at different length scales explain why we have the features observed for the 35h to 60 hours of ball milling states.

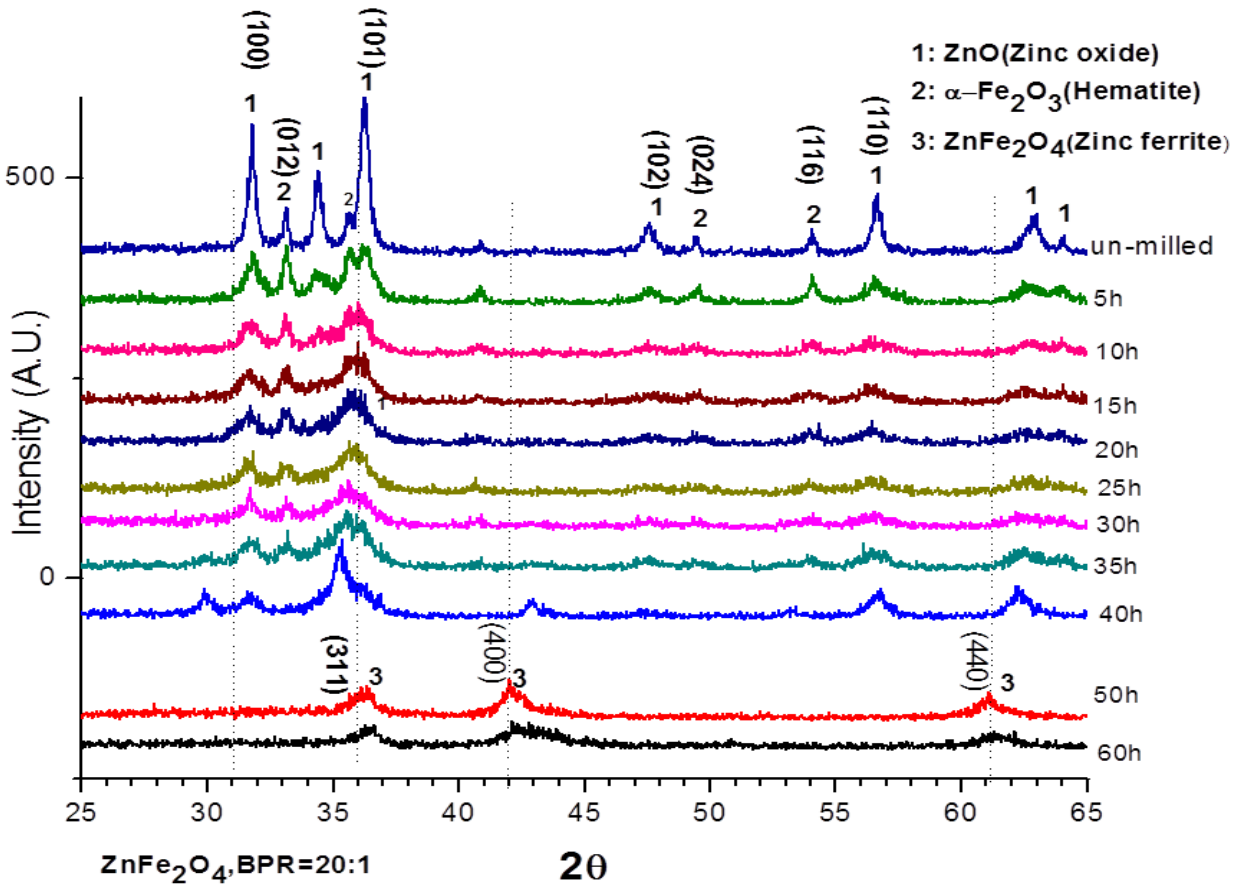


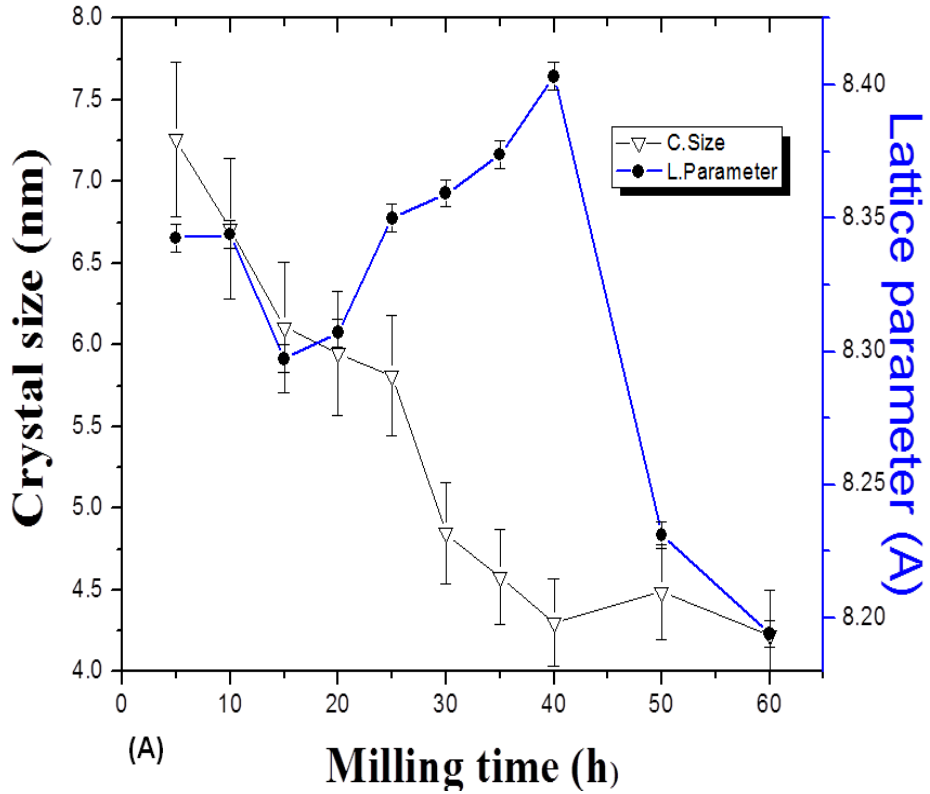
**Figure 31 : X-ray diffraction spectra of synthesis of ZnFe<sub>2</sub>O<sub>4</sub> by ball milling of ZnO and α-Fe<sub>2</sub>O<sub>3</sub> as a function of time using a BPR of 20:1.**

The average crystal size was about 5.43 nm, but varied in the 4.22nm-7.26nm range. This average crystal size is slightly smaller than those found by Verdier et al [26], which were 11.3, 11.1, and 10.9 nm for 9h of milling, corresponding to three different trials. As mentioned in the literature review, in this work, the authors reported that the spinel phase becomes homogeneous after 9h of milling time [26]. At 3h and 6h of milling time, the spinel phase is not homogeneous and the peaks of hematite were still observed. However, in our case, the single phase Spinel

structure, formed after of 50h of milling time. The ZnO peak (100) persisted upto 40h of milling, while it was a peak of zinc oxide in either nor present or not observed after 50h milling due to extremely low intensity with XRD measurements. Although, the BPR utilized by Verdier et al [26], and the one reported here is same (20:1), we can see that the time to get single phase Spinel structure reported by them was less in our case. This difference is commonly related to the influence of other parameter such as milling speed, milling container, as well as type, and size distribution of the grinding medium [29]. Jean et al [28], found efficient modes to obtain a pure zinc ferrite phase as a function of the rotational speeds of main disk and vials. Jean et al [28] experimented on the influence of rotational speeds of the main disk and vials in the mechanochemical syntheses of  $\text{ZnFe}_2\text{O}_4$  materials in order to determine its optimal synthesis condition. They reported the formation of  $\text{ZnFe}_2\text{O}_4$  having a size of 10 nm, which is slightly smaller than the value we obtain in this study, which ranged from 4.22 – 7.26 nm. Further, these values are smaller than the values quoted in the earlier section, with BPR of 10:1.

From the figure 32(A), the variations of crystal size and lattice constant for the  $\text{ZnFe}_2\text{O}_4$  with milling time are shown. The crystal size exhibited a less drastic reduction with milling time in comparison to the BPR = 10:1 processing reported in the previous section. The lattice parameter appeared to increase after 10 hours of ball milling and reached a maximum in the 40h of milled state, before a drastic drop for the 50h and 60h milled states. Interestingly, the maximum, lattice parameter for the 40h milled state corresponded to the “levelling-off” value of crystal size semblance at 40h. In the figure 32 (B) we can observe that the Crystal size of ZnO reached a minimum value of approximately 5.19 nm. From the figure we can observe that the crystal size did not decrease continuously if no that it varied after 10h until finally reach the value mentioned earlier. The crystal size for  $\alpha\text{-Fe}_2\text{O}_3$  phase decreased continuously until 35h of ball milling. Is

evident from the plot that crystal size shows further reduction between 5 and 10h of milling time, and after this time it decreased slowly. When compared with the precursors, the crystal size of Zinc ferrite also decreased continuously but it did not show drastic reduction as occurred for the ZnO and  $\alpha$ -Fe<sub>2</sub>O<sub>3</sub> phases within the first 10 hours of milling time.



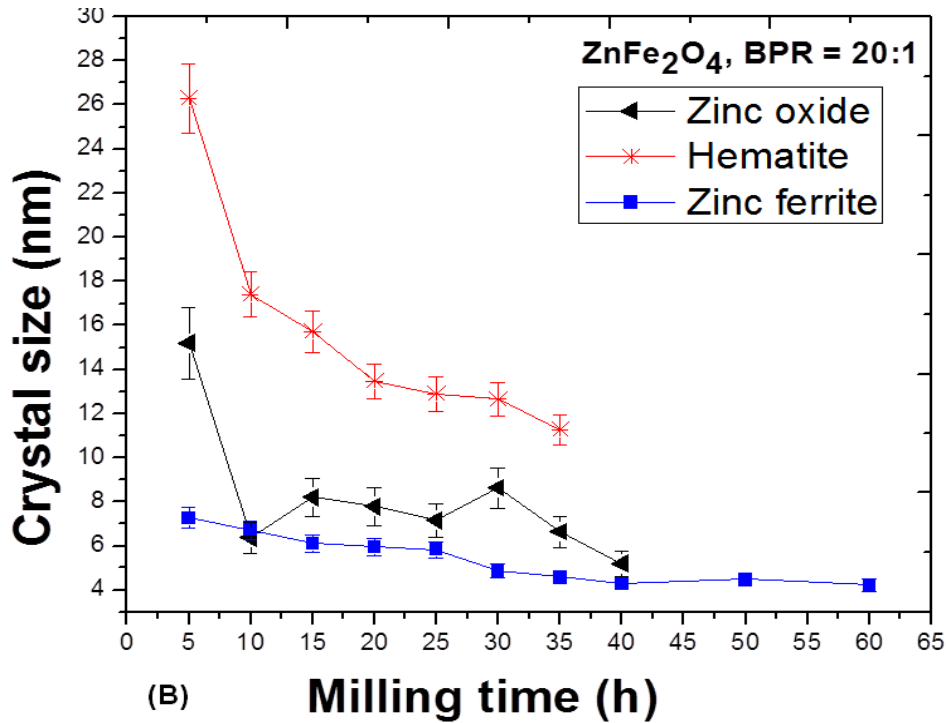


Figure 32: (A) Crystal size and lattice parameter as function of milling time to zinc ferrite synthesized by HEBM and BPR=20:1. (B) Evolution of the crystal size for the precursors ZnO,  $\alpha$ -Fe<sub>2</sub>O<sub>3</sub>, and ZnFe<sub>2</sub>O<sub>4</sub> as function of milling time.

The Fig.33 shows the variation of strain as a function of the milling time. We can observe how the strain increased in the material milled from 5h until 40h of milling time. For the following 5h, the strain shows a slight decrease and then an increase for 60h of milling. Similar to the case of ZnFe<sub>2</sub>O<sub>4</sub> synthesized with BPR = 10:1, the XRD diffraction peaks associated with prolonged milling time became broader, and, according to Lisfisths [72] this is due to fact particles have a large amount of lattice strains [39]. The average strain values are summarized in the table 5. If we compare carefully with table 3, it is easy to observe that we obtained higher strains for zinc ferrite synthesized with (BPR= 20:1), than those obtained using BPR=10:1. In the Fig.32 (A) we can also see the variation of the lattice parameter with the milling time. As in the previous

section, this variation can be due to accumulation of the strain. Table 5 summarizes the average for crystal size, lattice parameter and strain together with the entire values as a function of time. For the average crystal size we can compare our data to those obtained by Ehrhardt et al [37] , who obtained crystal size and lattice parameter for low energy milling (LEM) and high energy milling (HEM) synthesis. For example, they obtained  $d = 18$  nm and  $a = 8.451\text{\AA}$  after 120h for LEM mode. On the other hand, they obtained  $d = 8$  nm and  $a = 8.462\text{\AA}$  after 12h for HEM mode. As can be observed we obtained smaller value for crystal size (5.43 nm) and also a smaller value of the lattice parameter of  $8.320(3)\text{\AA}$ .

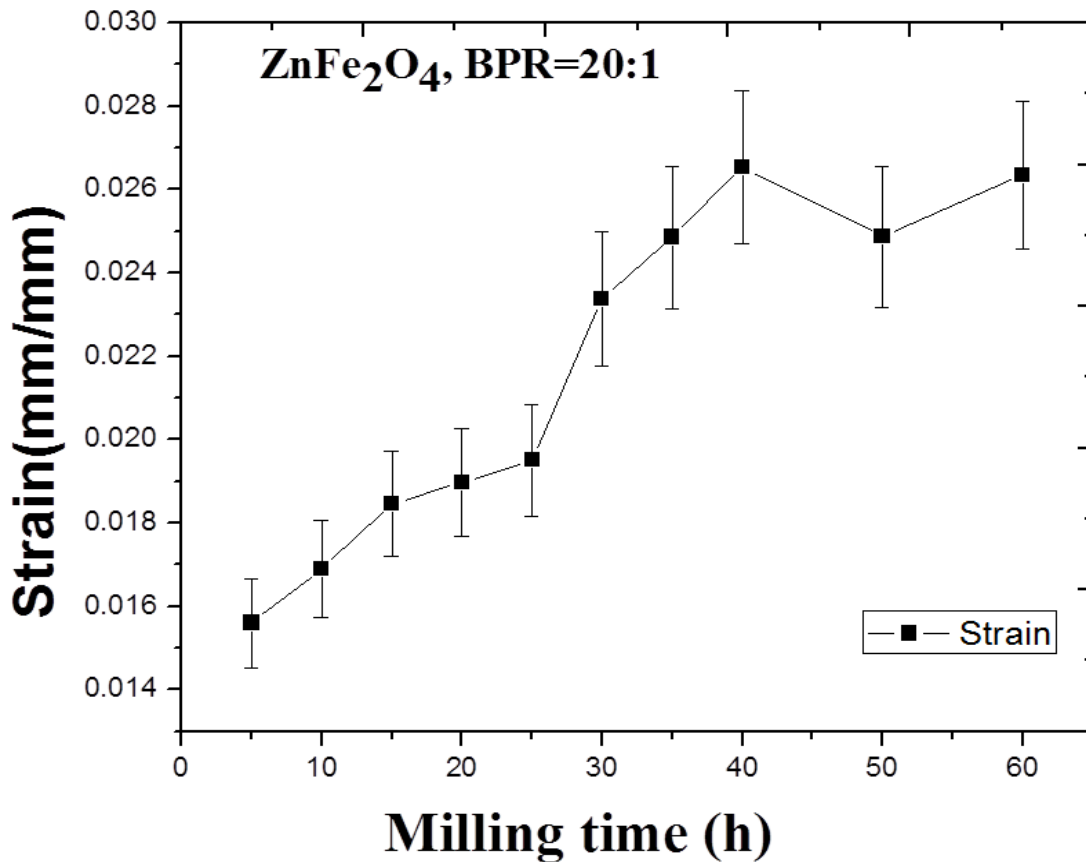


Figure 33: Strain as function of milling time to zinc ferrite with BPR=20:1 and synthesized by HEBM.

**Table 5: Crystal size, strain and lattice parameter of zinc ferrite synthesized by HEBM with BPR=20:1.**

Milling time (h)	ZnFe <sub>2</sub> O <sub>4</sub> with BPR = 20:1		
	Crystal size* " <i>d</i> " (nm)	Lattice parameter (Å)	Average Strain (mm/mm)
5	7.26	8.3426	15.603
10	6.71	8.3440	16.889
15	6.11	8.2974	18.453
20	5.95	8.3070	18.968
25	5.81	8.3501	19.506
30	4.85	8.3594	23.391
35	4.58	8.3740	24.855
40	4.30	8.4033	26.547
50	4.49	8.2313	24.869
60	4.22	8.1943	26.342
Average	5.43	8.3203	21.542

\* Determined from (311) ZnFe<sub>2</sub>O<sub>4</sub> reflection with Debye-Scherrer formula.

Further, in Fig. 32(A) we can observe the overall results of the lattice parameter variation as a function of milling time. We can notice that it changed slightly accord the time evolved. The minimum and maximum values reached by the lattice parameter were 8.342 and 8.444 Å respectively. The average lattice parameter was 8.408 Å. This value is slightly less than the lattice parameters obtained by Verdier et al.[26], and, Jean and Nachbaur [28]. Verdier et al reported a value of 8.438 Å for the lattice parameter, and while, Jean and Nachbaur [28] reported a value of 8.44 Å for the lattice parameter. The lower value obtained by us can be a consequence of a small inversion. Namely, Fe<sup>3+</sup> ions partially located in A sites.

#### 4.2.2. VSM measurements to ZnFe<sub>2</sub>O<sub>4</sub> with BPR 20:1

The room temperature measurements for all the milled materials up to 60 hours are shown in the figure 34. The magnetization and coercivity maximum were 28.726 Am<sup>2</sup>/Kg and 11.2 mT to 60

and 50h of milling time respectively. Coercivity, as in the before case, shows a decrease until the first 40h of milling time. From this time, coercivity shows an increase until it reaches a value of 120 mT. The magnetization continuously increased from 0.71644 Am<sup>2</sup>/Kg to 28.726 Am<sup>2</sup>/Kg. To 50h of milling time, the magnetization drops until a value of 8.6409 Am<sup>2</sup>/Kg and after, it increased until the maximum value of 28.726 Am<sup>2</sup>/Kg. This trend is generally associated with the increase in the cation distribution and with the diminution in the size of the grain. We can observe both coercivity and specific magnetization as function of milling time in the figure 35. Table 6 shows the values for both coercivity and specific magnetization for the synthesis of zinc ferrite with a BPR of 20 :1.

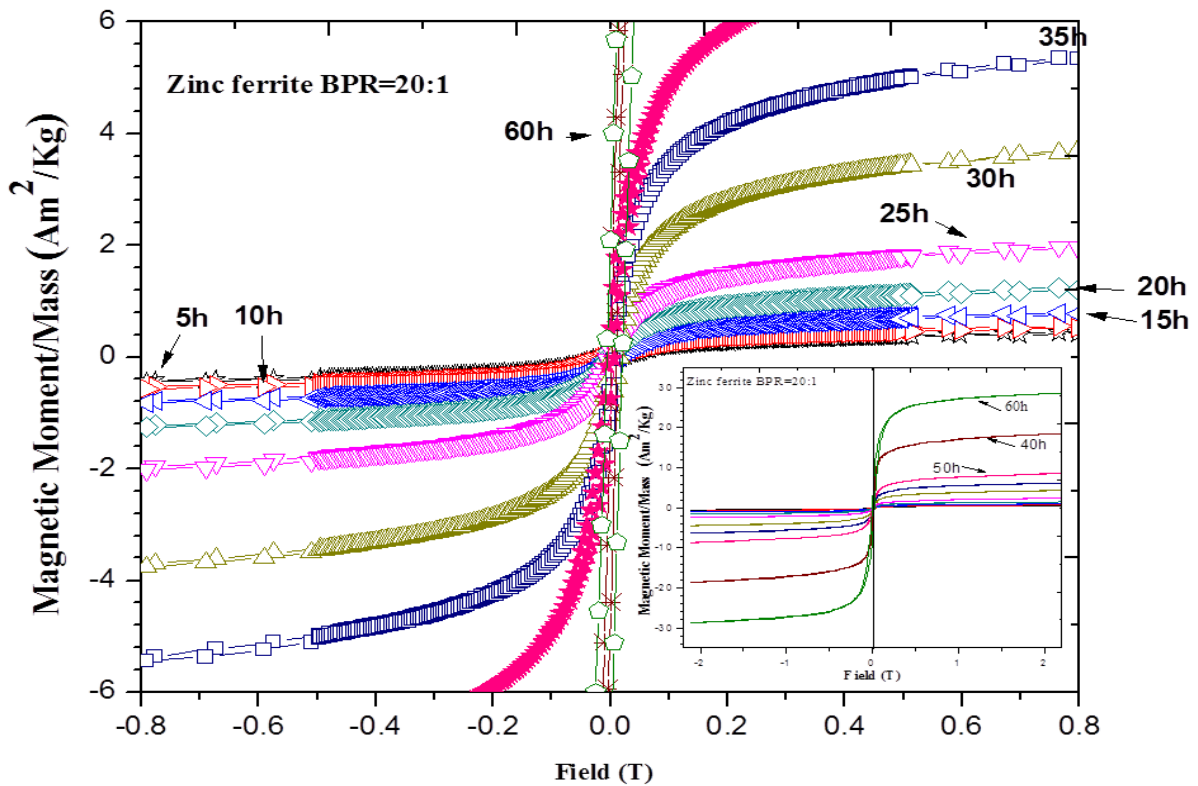


Figure 34 : Hysteresis loop for synthesis of ZnFe<sub>2</sub>O<sub>4</sub> with BPR= 20:1.

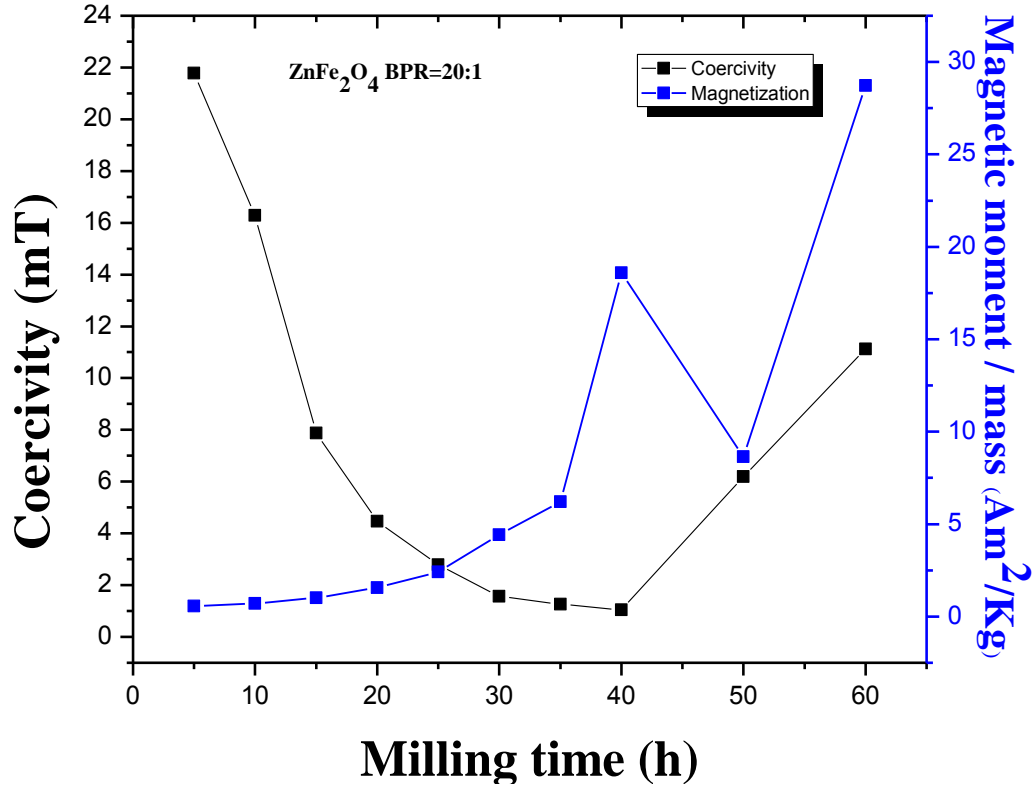


Figure 35: Coercivity size and Specific Magnetization as function of milling time for  $Ni_xZn_{1-x}Fe_2O_4$  with  $x=0$ , synthesized by HEBM and BPR=20:1

Table 6: Values for coercivity and magnetization as a function of milling time for zinc ferrite with BPR = 20:1

Milling time (h)	ZnFe <sub>2</sub> O <sub>4</sub> with BPR = 20:1	
	Coercivity (mT)	Saturation magnetization (Am <sup>2</sup> /Kg)
5	21.79	0.56
10	16.29	0.72
15	78.78	1.01
20	44.69	1.55
25	27.78	2.42
30	15.60	4.41
35	12.68	6.21
40	10.40	18.59
50	61.93	8.64
60	111.22	28.73

### 4.2.3. Mössbauer measurements to $\text{ZnFe}_2\text{O}_4$ with BPR 20:1

The Fig. 36 shows the entire room temperature Mössbauer spectra of all milled materials from 5h until 60h. The Mössbauer spectra showed the progressive increase in intensity of the central portion which evolved to a doublet that is clearly discernible for the 40h milled state. It could be observed that the mechanochemical synthesis did not conclude with the formation of non-magnetic  $\text{ZnFe}_2\text{O}_4$  up to 40 hours given that traces of magnetic sextet peaks are observed. This fact was also verified by XRD measurement, as shown in Fig. 31 where only spinel phase peaks are observed for the 50 h of milling. Compared to the previous case, we can say that in this case, the speed of reaction depends on BPR; i.e., it means that, the higher BPR led faster the rate of reaction. These spectra constituted by a magnetically ordered six-line pattern along with a paramagnetic doublet, can be explained on the basis of the presence of Fe ions with several environments, or sites [26]. The superparamagnetic relaxation time is clearly evidenced from the evolution from a sextet until a doublet appears. The superparamagnetic relaxation is related with a distribution times, consequence of a particle size distribution in a magnetic sample and this can manifest in the form of collapse of the sextet peaks to the non-magnetic singlet or doublet peaks.

The 5 hours ball milled state showed extremely small amount of conversion of the solid precursor materials as seen within the central portion of the spectrum together with the prominent sextet peaks of the hematite phase. The spectrum background could be seen to be flat indicating that the iron sites are well resolved. In comparison to the 10 hours ball milled state, the hematite sextet peaks are observed to be prominent while the central non-magnetic portion is found to increase in intensity. The same trend is observed in the 15 hours milled state with the major difference that the spectral background begin to be broad, while the base of the sextet

hematite peaks assume increased broadening. The central doublet peaks appear increasingly asymmetrical with the RHS peak more intense than the LHS one of the doublet.

The next major change in the overall spectral change is observed with the 40 hours ball milled state which showed evidence of only doublet peaks, with rather broad background. The evolution accompanying the subsequent 50 hours and 60 hours ball milled state, the background of the spectrum become better resolved with asymmetrical doublet especially in the 50 hours milled state. The totality of the spectral evolution for the BPR of 20:1 mechanochemical synthesis for the  $\text{ZnFe}_2\text{O}_4$  end-member ferrite suggested the presence of overlapping non-magnetically split Fe-sites. The first appearance of unsymmetrical profile of the central doublet peaks observed in the 20 hours milled state was reversed from the 40 hours ball milled state, where progressively, the LHS peak of the doublet became more intense than the RHS peak. The slightly higher intensity of the RHS peak noticed in the 20 hours ball milled state decreased, and eventually reversed with the LHS peak becoming more intense than the RHS one was shown in the 40 hours milled state.

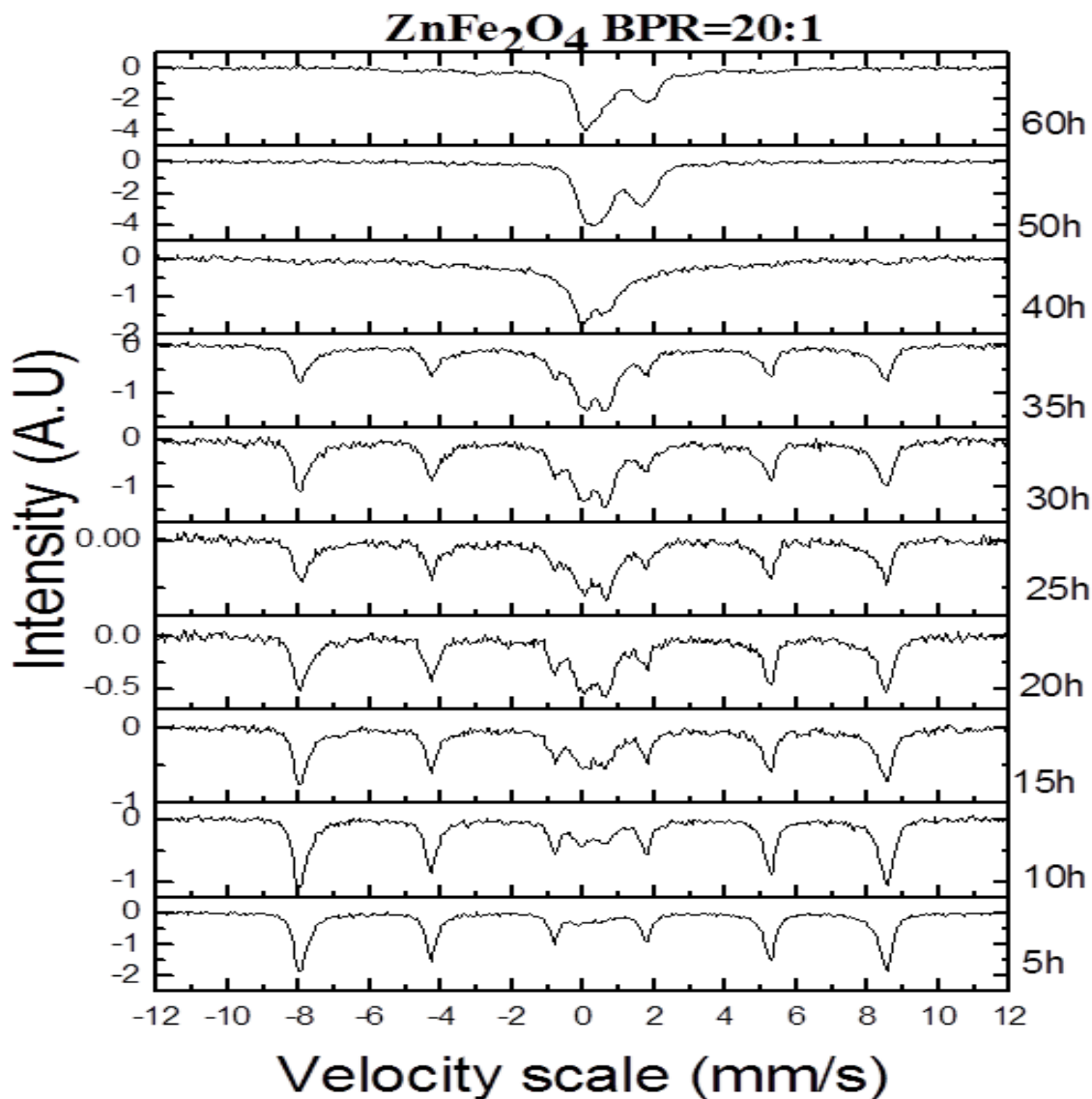


**Figure 36: Mössbauer spectra of ZnFe<sub>2</sub>O<sub>4</sub> ball-milled ZnO- $\alpha$ -Fe<sub>2</sub>O<sub>3</sub> mixture to BPR=20:1**

The Mössbauer spectrum for the 5h of milling time was fitted with a site whose internal magnetic field value was of 511.12 kOe, belonging, as in the before case, to the hematite phase. The internal magnetic field varied from 511.12 kOe to 511.71 kOe, 510.83 kOe, 510.83 kOe, 511.12 kOe, 511.56 kOe, 500.98 kOe and 504.95 kOe with relative abundance of 61.62%,

57.44%, 46.41%, 37.86%, 26.43%, 31.06%, 21.48%, 4.82% and 4.63%. The diminution in relative abundance, once more, indicated that the mechanochemical synthesis process was progressive and its evolution as a function of milling time is depicted in the figure 37. Although the relative abundance for the synthesis of zinc ferrite with BPR 10:1 showed further reduction in the firsts 35h of milling in comparison to the present case, we can observe from the description and the figures 31 y 37 than from 40h of milling the relative abundance for the BPR = 20:1 case is lower than the BPR = 10:1 case. In addition, the hematite for the present case had gone for 50h of milling. The last fact corroborates the dependency of velocity reaction on BPR.

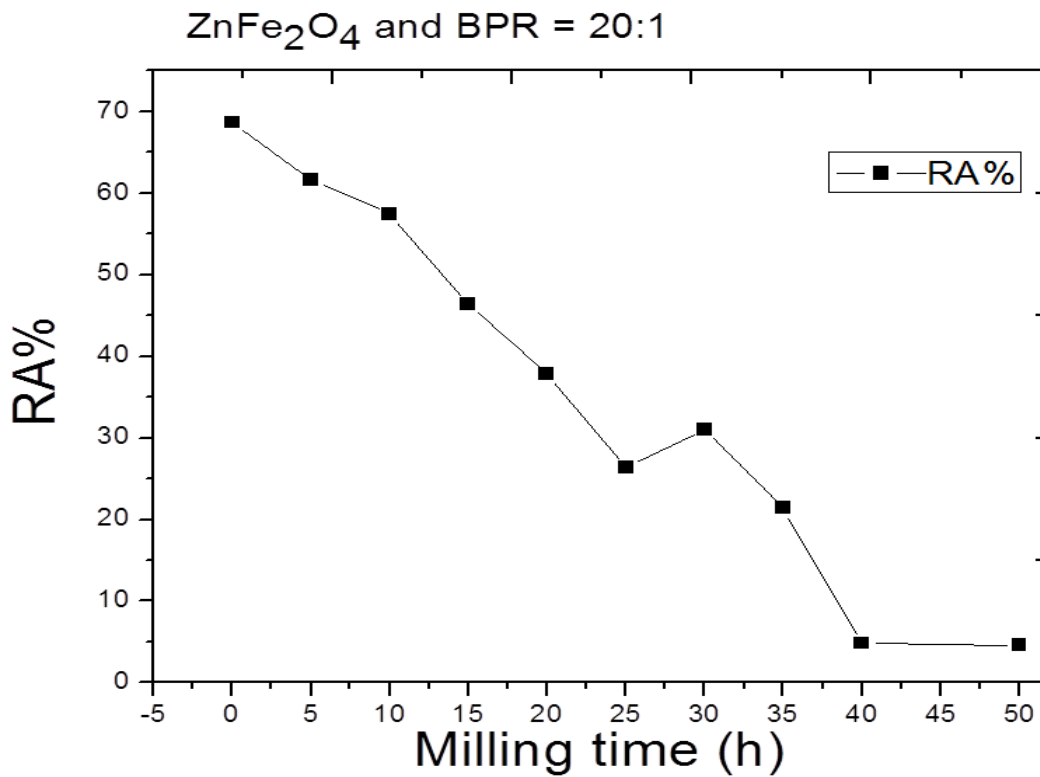


**Figure 37: Relative abundance of hematite as a function of milling time during the synthesis of ZnFe<sub>2</sub>O<sub>4</sub> using a BPR of 20:1**

### **4.3. Mechanochemical synthesis of Zinc ferrite BPR = 40:1**

#### **4.3.1. XRD measurements**

Figure 38 shows the XRD patterns of all the milled materials during the mechano-chemical synthesis zinc ferrite with a BPR of 40:1. Unlike the previous cases shown in Fig. 24 and Fig. 31 we can see that the spinel phase was reached in a lesser time. After the 5h of milling time, we can observe only a peak, in approximately  $2\theta = 40^\circ$ , which corresponded to hematite phase. This implies that zinc oxide was consumed in comparison with hematite. The pure spinel phase peaks became the only ones observed for 10h of milling time (see Fig.38), thus allowing us to state that the spinel phase materialized in shorter milling time when compared to the previous cases. In the Fig 39, we assemble the XRD spectra corresponding to the times when only the spinel phase was obtained as a function of BPR used. We can observe clearly that only the spinel phase peaks are observed thereby confirm the completion of the mechano-chemical synthesis.

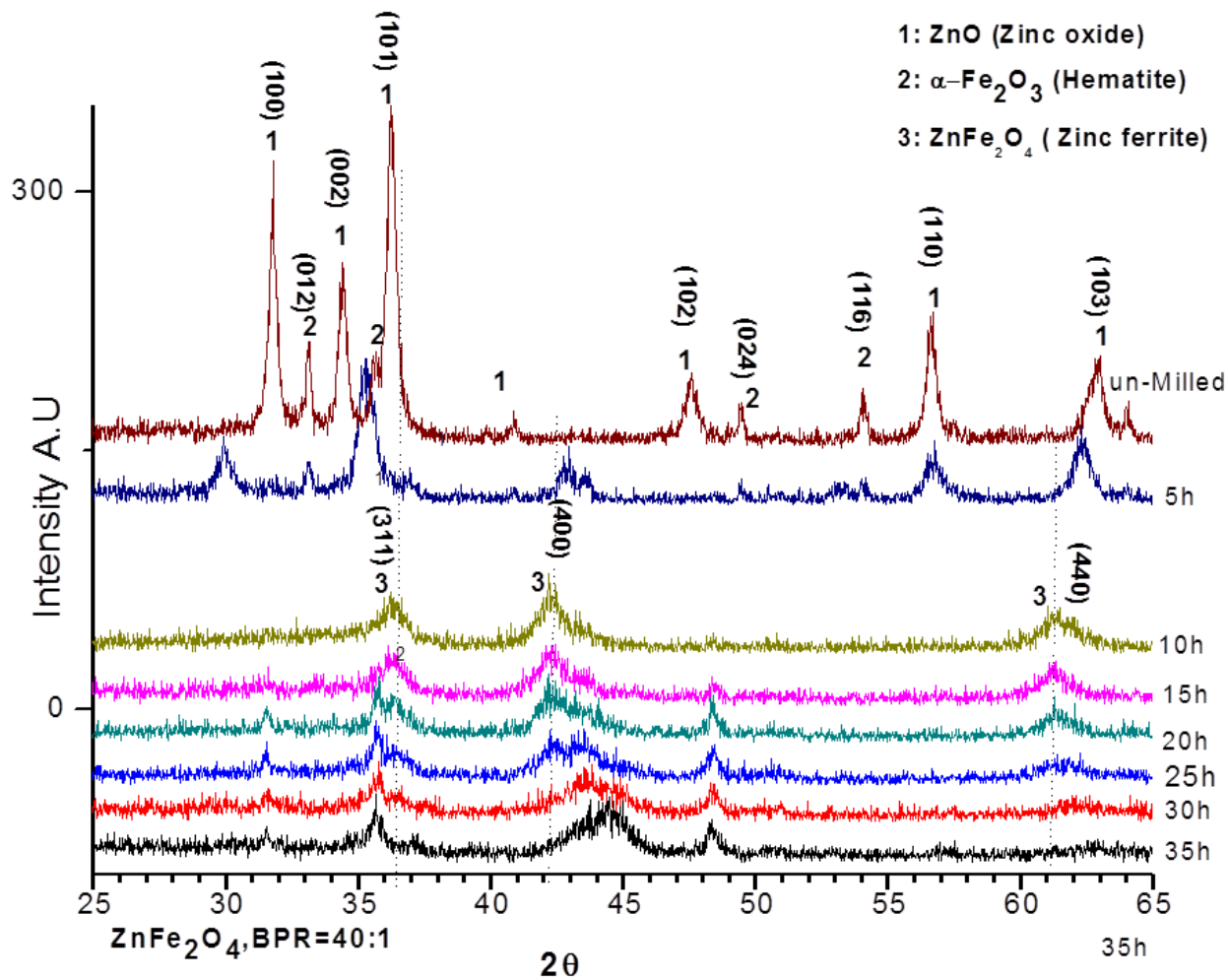
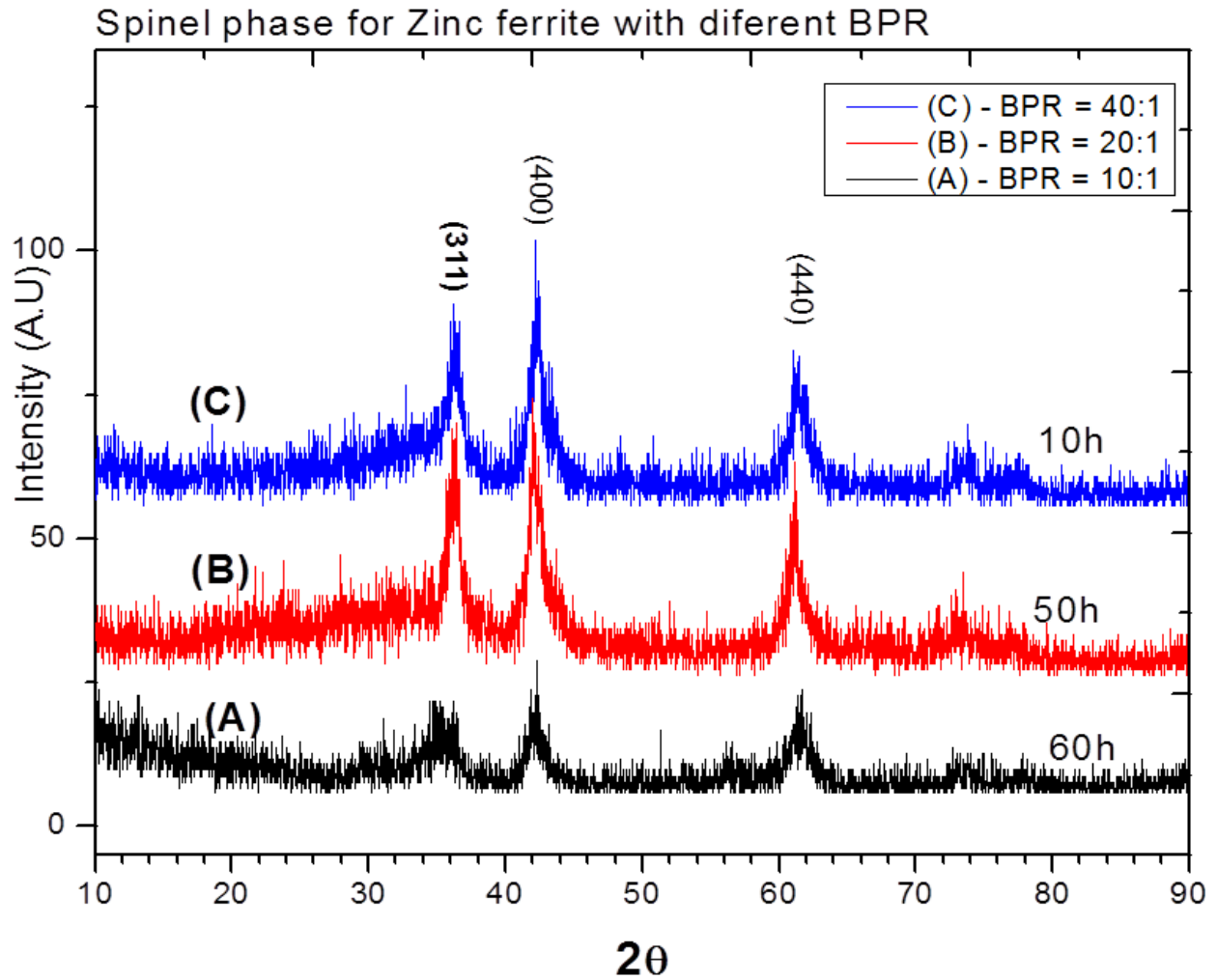


Figure 38: : X-ray diffraction spectra of synthesis of ZnFe<sub>2</sub>O<sub>4</sub> by ball milling of ZnO and  $\alpha$ -Fe<sub>2</sub>O<sub>3</sub> as a function of time using a BPR of 40:1.

The principal difference showed in Fig. 39 is the time employed to reach the spinel phase. This is the evidence pointing to the importance of BPR as was mentioned earlier. Our study showed that with higher BPR we can get spinel phase in a lesser time. The Fig. 39 also allows us observe the reproducibility of the mechanochemical synthesis because in each case, we observed the same set of peaks in the same positions. Some differences in the spectra such as the intensities in the diffraction peaks are clearly discernible. Clearly we can observe lower intensities in the diffraction peaks for zinc ferrite with BPR = 10:1 and higher intensities in the diffraction peaks

for zinc ferrite for BPR = 20:1. The above mentioned is commonly related to crystallinity of the samples and the disorder induced during the milling.



**Figure 39: XRD spectrums for spinel phase. The time represent the hour of milling time necessary to reach the spinel phase. This fact is corroborated with Mossbauer measurement.**

The Fig.41 shows the variation of the crystal size and the lattice parameter as a function of the milling time for zinc ferrite with BPR = 40:1. The crystal size decreased as the milling time evolves and their values ranged between 4.80 - 7.05nm approximately. The average crystal size was 5.74 nm. In the Fig. 40 we can see the crystal size reached a value of 7.08 nm for the first 5h

of milling time, which is lower than 7.26 nm, and, 15.40 nm for zinc ferrite obtained for BPRs of 20:1, and, 10:1 respectively. We can compare, from this figure, the evolution in the crystal size. We can observe that the average crystal size is less for the BPR = 40:1 case. This fact is commonly due to higher energy of impact transferred to the grain, and therefore it is possible to get smaller crystal size than the case of both BPR = 20:1 and BPR = 10:1 respectively. The variation in the lattice parameter, similar to previous cases, shows increases between 5 and 10h of milling time. For the 15 hour of milling time, its value dropped and thereafter it increased until 35h. This variation is also due to strain, it which can be observed in the figure 42, introduced by the ball milling. Similar to the previous cases, it showed an increase as the milling time evolved. The average lattice parameter in this case was 8.3400 Å, which is slightly less than those reported in other work by the same and different synthesis processes [1], [2],[3],[4]. In Table 7, we can observe the average lattice parameter, average strain and crystal size to zinc ferrite with the distinct BPR mentioned earlier.

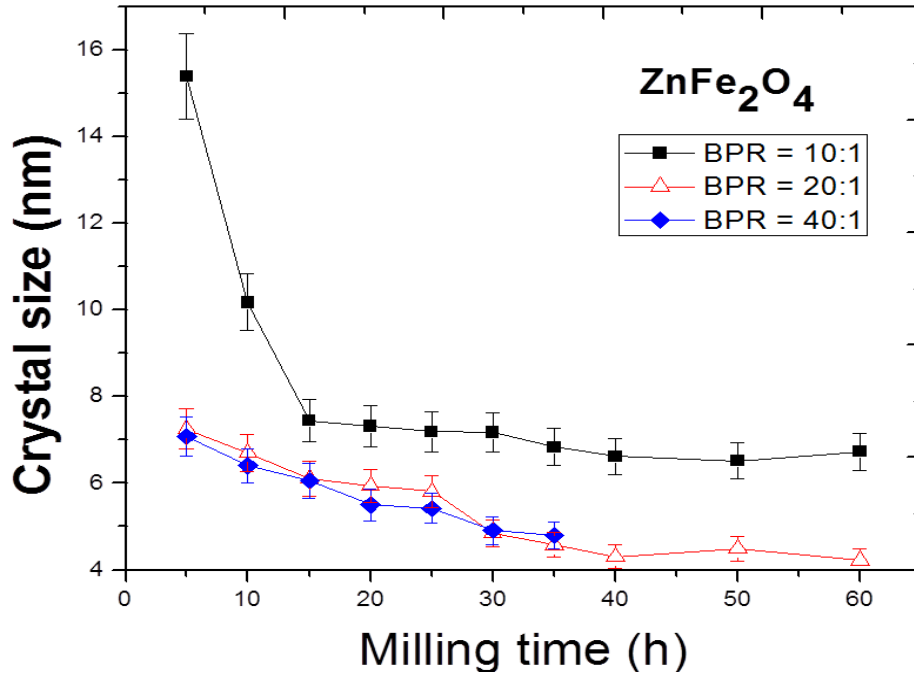


Figure 40: Evolution in the crystal size for Zinc ferrite for the different BPR: 10:1, 20:1 and 40:1

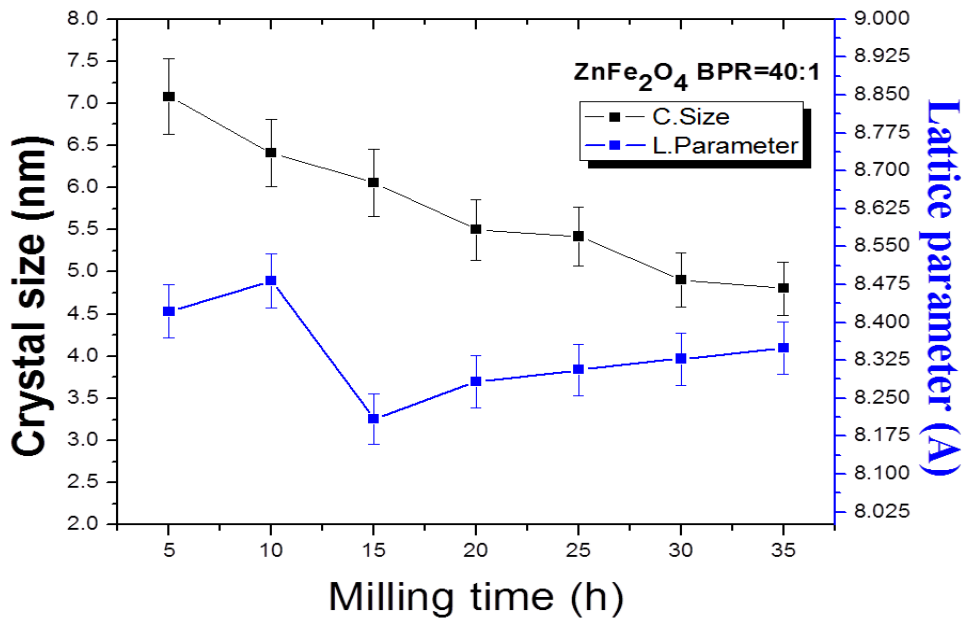


Figure 41: Crystal size and lattice constant as function of milling time to zinc ferrite synthesized by HEBM and BPR = 40:1.

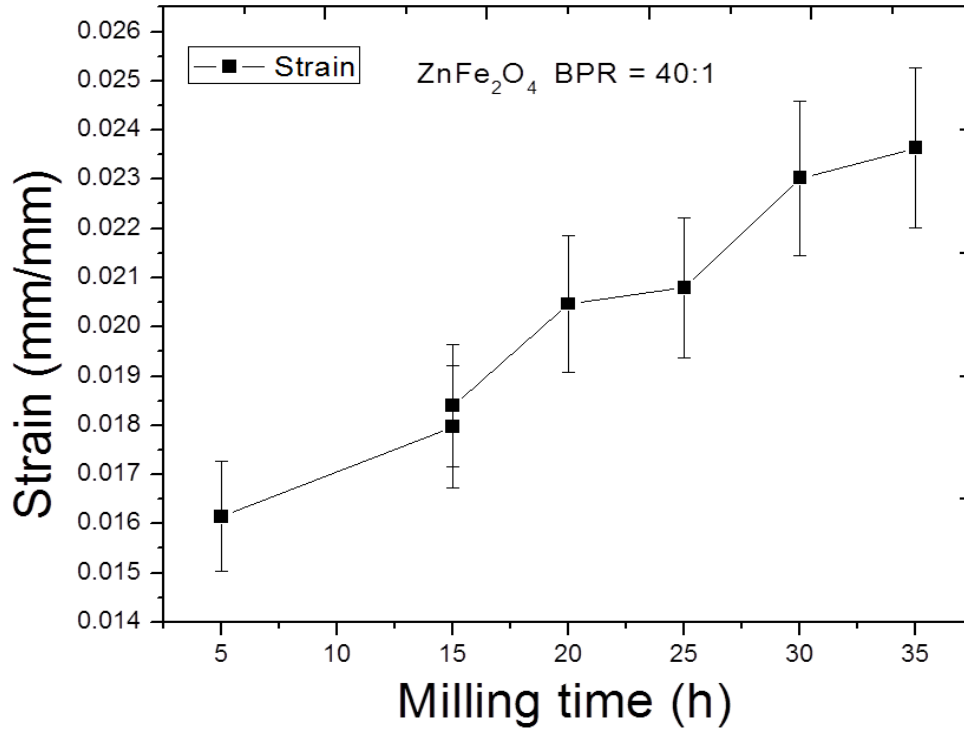


Figure 42: Strain as function of milling time for Zinc Ferrite with BPR = 40:1 and synthesized by HEBM.

Table 7: Crystal size, strain and lattice parameter of zinc ferrite synthesized by HEBM with BPR=40:1.

Milling time (h)	ZnFe <sub>2</sub> O <sub>4</sub> with BPR = 40:1		
	Crystal size* " <i>d</i> " (nm)	Lattice parameter (Å)	Average Strain (mm/mm) x 10 <sup>-3</sup>
5	7.08	8.4217	16.15
10	6.41	8.4824	17.97
15	6.06	8.2087	18.40
20	5.50	8.2833	20.47
25	5.42	8.3063	20.80
30	4.91	8.3281	23.03
35	4.80	8.3494	23.63
40	-	-	-
50	-	-	-
60	-	-	-
Average	5.74	8.3400	20.06

\* Determined from (311) ZnFe<sub>2</sub>O<sub>4</sub> reflection with Debye-Scherrer formula.

### 4.3.2. VSM measurements

VSM measurements of all the samples materials were carried out at room temperature, and are shown in the Figure 43. Coercivity was found to increase with the milling time. It is important to note that the least value was for the 5h of milling time (0.0011 T). After this time, coercivity showed a continuous increase. For 10h of milling time, the coercivity reached a value of 0.0084T. From this value, it increased until it reached a value of 0.0219T. This enhancement in coercivity occurs when it increases toward an extreme value controlled by the anisotropy when the crystal size is reduced to dimensions of the domains wall width [40].

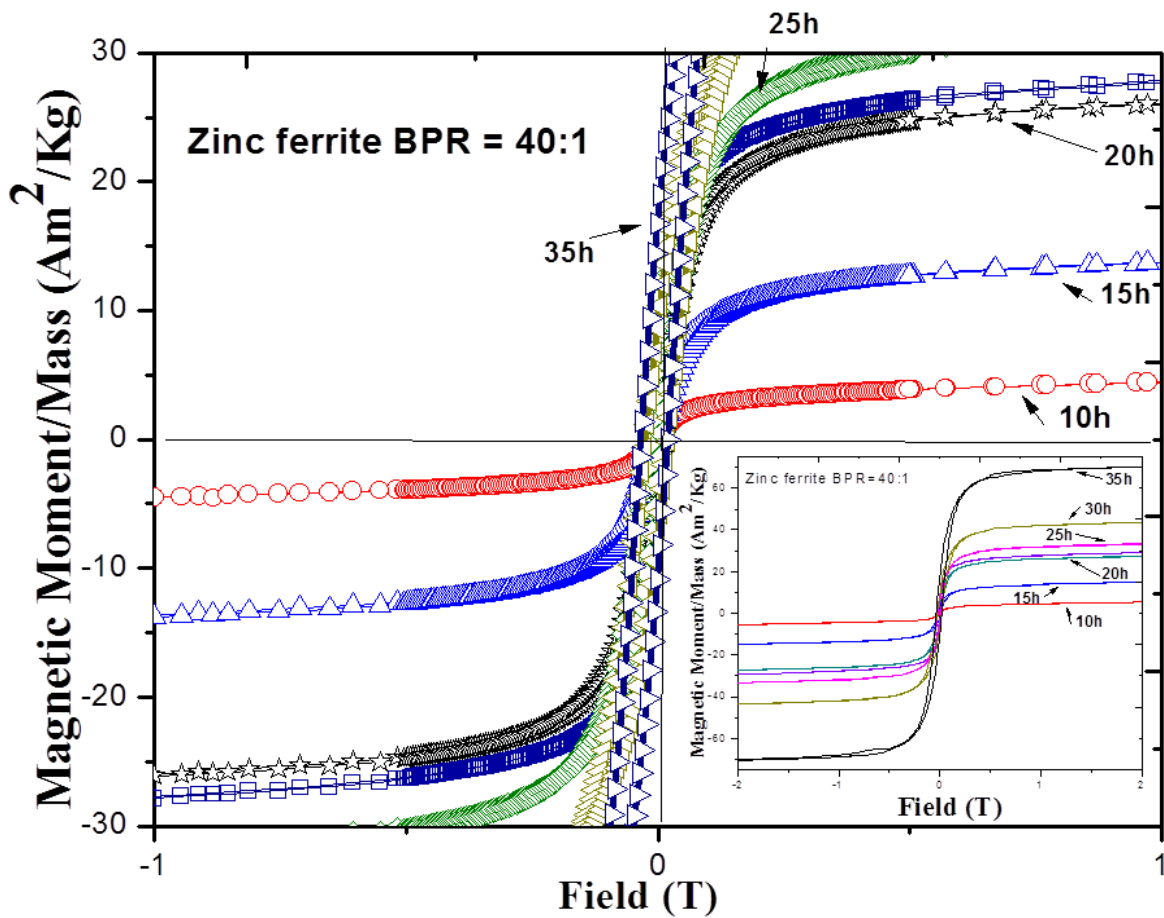


Figure 43: Hysteresis loop for the synthesis of ZnFe<sub>2</sub>O<sub>4</sub> with BPR= 40:1

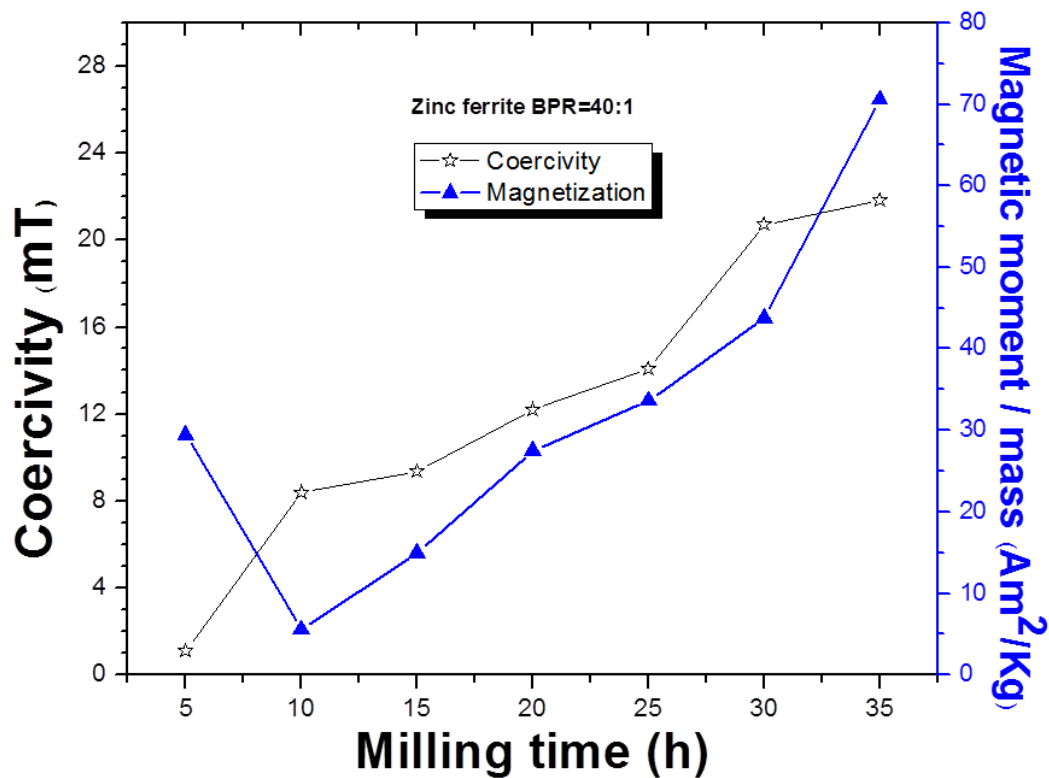


Figure 44: Coercivity size and magnetization as function of milling time for the synthesis of  $Ni_xZn_{1-x}Fe_2O_4$  with  $x=0$  ( $ZnFe_2O_4$ ), synthesized by HEBM and BPR = 40:1.

Table 8: Values for coercivity and magnetization as a function of milling time for the synthesis of  $ZnFe_2O_4$  with BPR = 40:1.

Milling time (h)	$ZnFe_2O_4$ with BPR = 40:1	
	Coercivity (mT)	Saturation magnetization (Am <sup>2</sup> /Kg)
5	1.11	1.16
10	8.38	0.57
15	9.37	1.94
20	12.19	4.40
25	14.60	5.65
30	20.72	7.78
35	21.83	11.76
40	-	-
50	-	-
60	-	-

On the other hand, magnetization increased from 10h until 35 h of milling time and its evolution according milling time can be observed in the figure 44. The increase in the magnetization is generally associated with the grain size reduction and with the increase of the cation inversion[32] . The increase in the coercivity, as was seen earlier, has been observed in other ferrites such as cobalt ferrite. In this case, the enhancement in coercivity is due to the increase in magnetocrystalline anisotropy imparted by cobalt to the oxide when more cobalt is added [32]. The data of Table 8 summarizes all values of coercivity, and saturation magnetization corresponding to the synthesized zinc ferrites with BPR = 40:1.

#### **4.3.3. Mössbauer measurements to $\text{ZnFe}_2\text{O}_4$**

In the Fig. 45 we can observe the evolution in the Mössbauer spectrum to zinc ferrite with BPR = 40:1. We can observe that for the 5h of milling time the six-line pattern all together collapsed in a doublet for the next 5h of milling time. In contrast to of the Fig. 29 and Fig. 36, the mechanochemical synthesis was completed for 10h of milling time. This implied that the reaction rate depended on the BPR value used. In this figure we can observe as, from 25h of milling time, the Mössbauer spectra showed some wings, with the doublets decreasing in intensity and while the sextet lines increased. For 35h of milling, we can observe that the superparamagnetic state was almost disappeared. We can see that sextet peaks indicates a ferromagnetic ordering in the materials, where this ordering can be explained either from the theory of superparamagnetic relaxation or from a presence of large particles measuring, at least 18 nm according Kundig and Bommel [42] which is referenced in the study by Bid [41]. According to Bid et al [42], in our

case we can also say that the appearance of sextet from the theory can be due to the loss of superparamagnetic relaxation, which is given by

$$\tau = \tau_0 \exp(KV/K_B T) \quad [43]$$

Here,  $\tau_0$  depends slightly on temperature, and, is of the order of  $10^{-9}$ - $10^{-12}$ ;  $K$ , is the Boltzmann constant,  $T$ , is the temperature,  $K$ , is the magnetic anisotropy energy constant, and,  $V$ , is the volume of the particle. According to Bid, the form of the Mössbauer spectrum of magnetic nanoparticles depends on the correlation between the time of observation ( $\tau_{\text{obs}}$ ) and the vector relaxation ( $\tau$ ). Similar to Bid, we obtained particles with smaller crystal size than 18 nm, which according to him, the corresponding Mössbauer spectra, consisting of doublet and sextet, implied that  $\tau = \tau_0$ . Moreover, he said that the sextet can be explained through a possible variation of the anisotropy constant  $K$  for differently ball-milled samples presumably due to internal strain [41]. On the other hand, Wang and Jiang [42] related the doublet with small hyperfine field values of about 30 kOe. Others authors, such as Mozzafari [43] related the sextet due to iron in the samples and two overlapping quadrupole doublets.

Looking at carefully the Mossbauer spectra we can observe that the 5 hours milled state, show the presence of sextet peaks associated with the hematite phase, and a very small intensity sextet peaks followed by the central portion that is consisted of the non-magnetic peaks. In addition, the background of the spectrum is broadened and dropping from the flanks. The 10 hours ball milled state show that the mechanochemical synthesis process was completed with the complete disappearance of the sextets found in the 5 hours ball milled state. The background of the

spectrum is flat in contrast to the previous cases associated with the mechanochemical syntheses for the end-member  $\text{ZnFe}_2\text{O}_4$  for the ball-to-powder ratio of 40:1.

The 15 hours ball milled state showed the presence of the non-magnetically split central doublets with more prominent doublets than in the 10 hours milled state. In contrast, in the 20 hours milled state, the spectrum consists of both weak magnetically split portions and the prominent central doublet similar to the previous case of the 15 hours milled state. The subsequent continued ball milling as in the case of 25 hours milled state showed that the magnetically split portion remained less than the non-magnetic state, despite slight increase in comparison to the 20 hours state. Further, the 30 hour milled state, showed that the central portion of the spectrum revealed slight changes in general in comparison to the central portion for the previous milled states. Lastly, in the 35 hours milled state, the sextets portion becomes much more prominent, while the central portion evolved rather to a prominent singlet and a doublet as well.

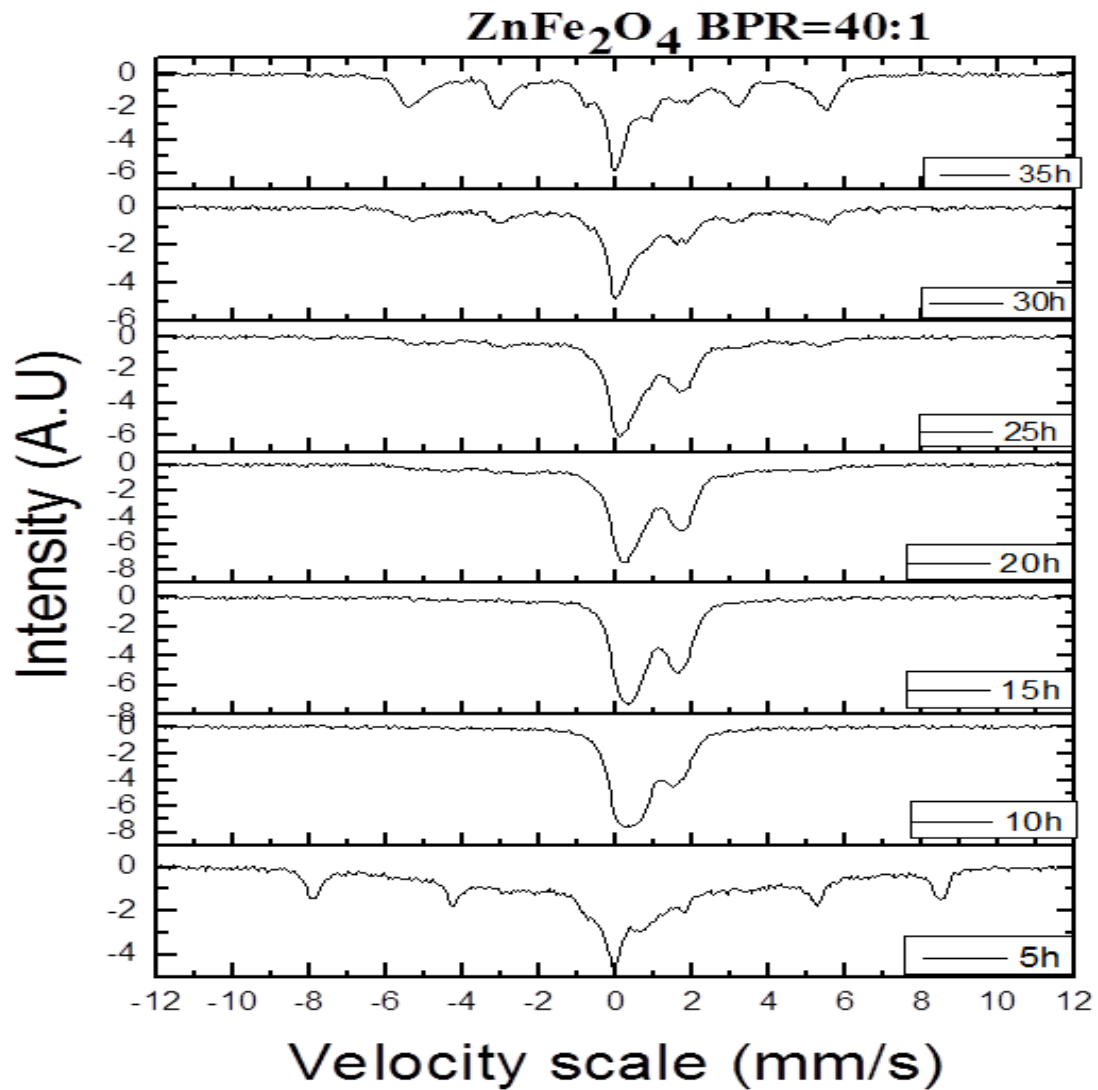


**Figure 45: Mössbauer spectra of ZnFe<sub>2</sub>O<sub>4</sub> ball-milled ZnO- $\alpha$ -Fe<sub>2</sub>O<sub>3</sub> mixture to BPR = 40:1**

In this case, for the 5h of milling time, the Mössbauer spectrum belonging to hematite phase was fitted with a internal magnetic field value of 506.71 kOe, and relative abundance of 17.9%, which is lowest than the previous cases. Is important note that for the 10h of milling time the hematite phase had gone entirely and we can corroborate this fact looking at figure 45, where for

the 10h of milling the Mossbauer spectrum collapsed in a doublet that evidence the completion of the mechanochemical synthesis. Figure 46 shows the relative abundance for the unmilled and milled for 5h phase of hematite.

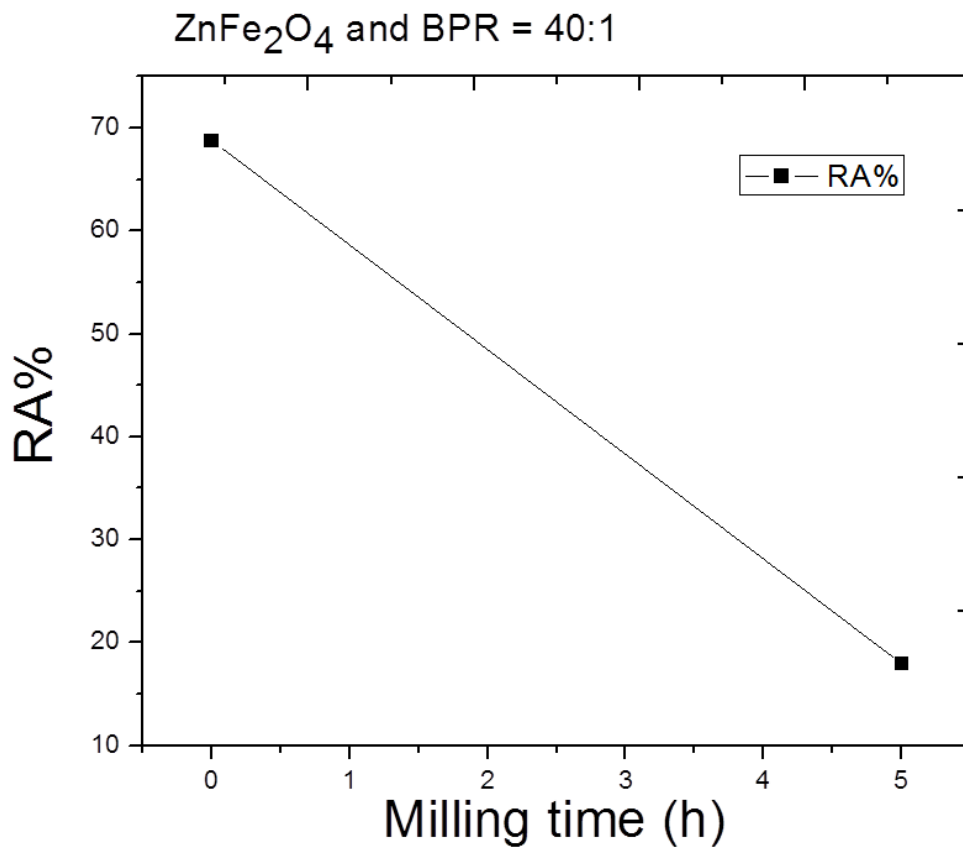


**Figure 46: Relative abundance of hematite as a function of milling time during the synthesis of  $\text{ZnFe}_2\text{O}_4$  using a BPR of 40:1**

In Fig. 47, we can observe the spectrum for the superparamagnetic state of each sample of zinc ferrite. We can note three doublets, each one corresponding to a synthesis, namely, zinc ferrite, with the BPR's 10:1, 20:1 and 40:1. In the figure we can note the milling time that indicated the time necessary to get the superparamagnetic state. As was corroborated earlier, we can see that

the doublet for zinc ferrite with BPR = 40:1 was obtained in a lesser time, namely, 10h of milling time. In similar manner, the synthesis with BPR = 20:1 was completed in a less time than the case with BPR = 10:1. It is important to note carefully the shape for each spectrum. Although they all represent doublets, there are differences in the shape of these spectra. The three doublets are asymmetric as a consequence of milling process which introduced disorder, giving rise to the form asymmetric doublets [44] . In all spectra of our work for each synthesis, it was possible to observe the relaxation time, which gives rise to the quadrupole doublets and the singlet peaks, where doublets are due to spin relaxation rather than to a quadrupole interaction. According to calculations short relaxation times corresponded to a large quadrupole interaction [45]. In other systems, it has been found that the Mössbauer spectrum depended on the jump-time (electron hopping) and the electronic occupation probability [46], small polaron hopping [47] or temperature [31]. Also, it is possible to observe the relaxation time in other system carried out by different methods [48–50]. Table 9 shows the values of crystallite sizes obtained for ZnFe<sub>2</sub>O<sub>4</sub> for different synthesis methods. These values can be compared with those obtained in earlier sections. We can observe that the crystallite size depend on preparation method. In our case, all doublet were obtained with crystal sizes below 10 nm.

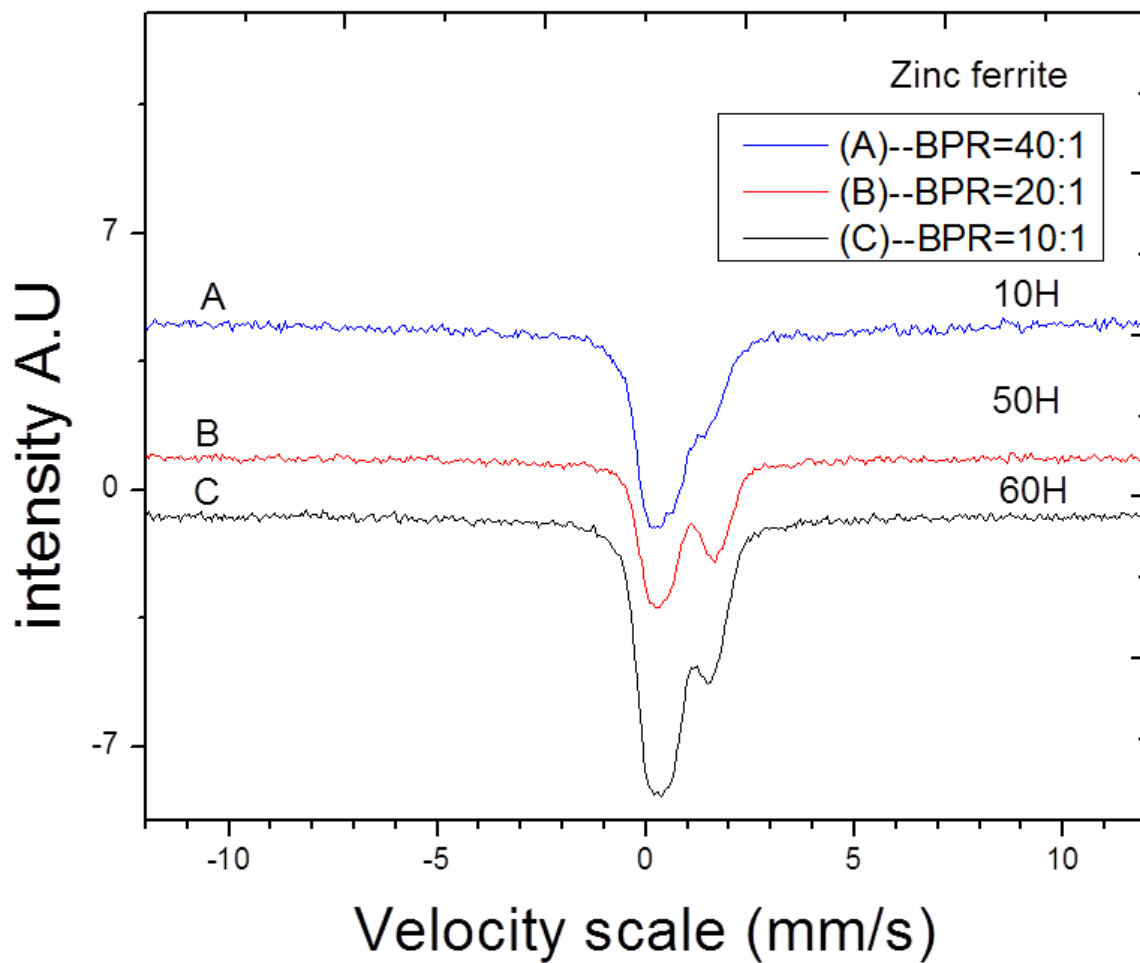


Figure 47: Mössbauer spectra for Zinc ferrite. Each doublet corresponds to synthesis with a distinct BPR, and, the time to obtain corresponding superparamagnetic state.

**Table 9: Comparison of crystallite sizes obtained for ZnFe<sub>2</sub>O<sub>4</sub> for different synthesis methods.**

		Ceramic or Co-precipitation	Hydrothermal Micro emulsion	Hydrothermal+ Milling	LT	LTSSR	Sol-gel	HEBM
<b>Li et al. (2007)</b>	XRD (C. Size(nm))	39				58 45		
	TEM (C. Size(nm))					60 50		
<b>Battle et al.(1997)</b>		15-20	5-20	15-20	<b>5-20</b>	5-20		
<b>Li et al. (2004)</b>						6-90	20	20 (ZFB)
<b>Verdiel et al. (2005)</b>								11, 10.5
<b>Ehrhardt et al. (2002)</b>								18, 8
<b>Ahn et al. (2002)</b>			8.4					
<b>Kundu et al. (2003)</b>		13						

## **5. Comparative study of the synthesis $\text{Ni}_x\text{Zn}_{1-x}\text{Fe}_2\text{O}_4$ for $x = 0.25, 0.75$ and $x = 0$ (End member)**

### **5.1.Synthesis of $\text{Ni}_x\text{Zn}_{1-x}\text{Fe}_2\text{O}_4$ for $x = 0.25$**

#### **5.1.1. XRD measurements**

We can observe rapid or drastic reduction in the intensity, and broadening of the XRD peaks of NiO, ZnO and  $\alpha\text{-Fe}_2\text{O}_3$ . Solid precursor materials XRD results show that the onset time of Ni-Zn ferrite formation was as early as 5h of ball milling time; with the associated peaks located in approximately  $2\theta = 35^\circ$  and  $43^\circ$  respectively. For the 10h of milling time, see Fig. 48, mainly includes the ferrite phase, although traces of both ZnO and hematite were still observed. This fact suggests that ZnO and hematite were not completely consumed by the reaction within 10 hrs. The average crystallite size was determined by the Scherrer's equation to be an average of 8.23 nm. The overall variation of the crystallite size was from 10.11 nm to 6.23 nm, for the 5h and 35h of milling times respectively. For 35h of milling time, the crystal size showed a slight increase which can be due to the effects of cold-welding characteristic in this type of milling process.

Fig. 49(A) shows the evolution of the crystal size and lattice parameter with the milling time. It can be observed as the crystal size showed a clear trend to decrease as the milling evolved. On the contrary, the lattice parameter varied as the milling time evolved and did not showed a clear trend. As was mentioned in the previous section for the zinc ferrite syntheses, this variation of lattice parameter with the milling could be due to accumulation of lattice imperfections characteristic of ball milling. The evolution the crystal size for the different phases, namely, ZnO,  $\alpha\text{-Fe}_2\text{O}_3$  and zinc ferrite can be observed in the Fig. 49 (B). The crystallite size of ZnO phase increased from 5 to 10h of milling time, and for 15h it decreased and after this time it

decreased slowly until the 30h of milling time. Contrary to the ZnO phase, we determined the crystal size for the  $\alpha$ -Fe<sub>2</sub>O<sub>3</sub> phase only for 5h of milling time due to the peaks belonging at this phase were not observed clearly due to extremely low intensity as can be observed in the XRD pattern. The average crystal size reported in this thesis is slightly lower to the values found by Jalaly et al [51], who reported 18 nm after 60h of milling time. Their Ni-Zn ferrite was produced directly by HEBM and was reported to be realized in two stages. According to these authors, in the first stage, zinc ferrite by diffusion of ZnO through Fe<sub>2</sub>O<sub>3</sub> was obtained, while in the second stage, NiO was diffused through zinc ferrite [51]. Takur et al. [52], reported an average crystal size of 8.4 nm based on their synthesis carried out by reverse micelle technique. The bulk material was subsequently prepared by annealing the as-produced nickel-zinc ferrite nanoparticles at 1473 K. [52]. Sharma et al. [53] reported an average crystal size in the range of 4-8nm without heat treatment, and 15-18nm and 40-50nm after heat treatments [53]. The method utilized in their study was by synthetic route and heat treatments. By means of chemical precipitation of hydroxides followed by hydrothermal technique, Upadhay et al.[54] reported the formation of Ni-Zn ferrite with an average crystal size in the range of 6-10nm [54]. In this work, these authors reported the compositions of  $x = 0, 0.5$  and  $1.0$  for Ni<sub>1-x</sub>Zn<sub>x</sub>Fe<sub>2</sub>O<sub>4</sub>. It should be noted that is possible to obtain ferrites with crystal size bigger than the values reported in their work. An example to this fact was the Cobalt-substituted nickel-copper ferrite system prepared by the standard method of sintering ceramic technique, where the average grain sizes reported were 1.16, 1.28 and 1.32  $\mu\text{m}$  for the materials with  $x = 0.01, 0.02,$  and  $0.03$  in the Ni<sub>0.95-x</sub>Co<sub>x</sub>Cu<sub>0.05</sub>Fe<sub>2</sub>O<sub>4</sub> system [55].

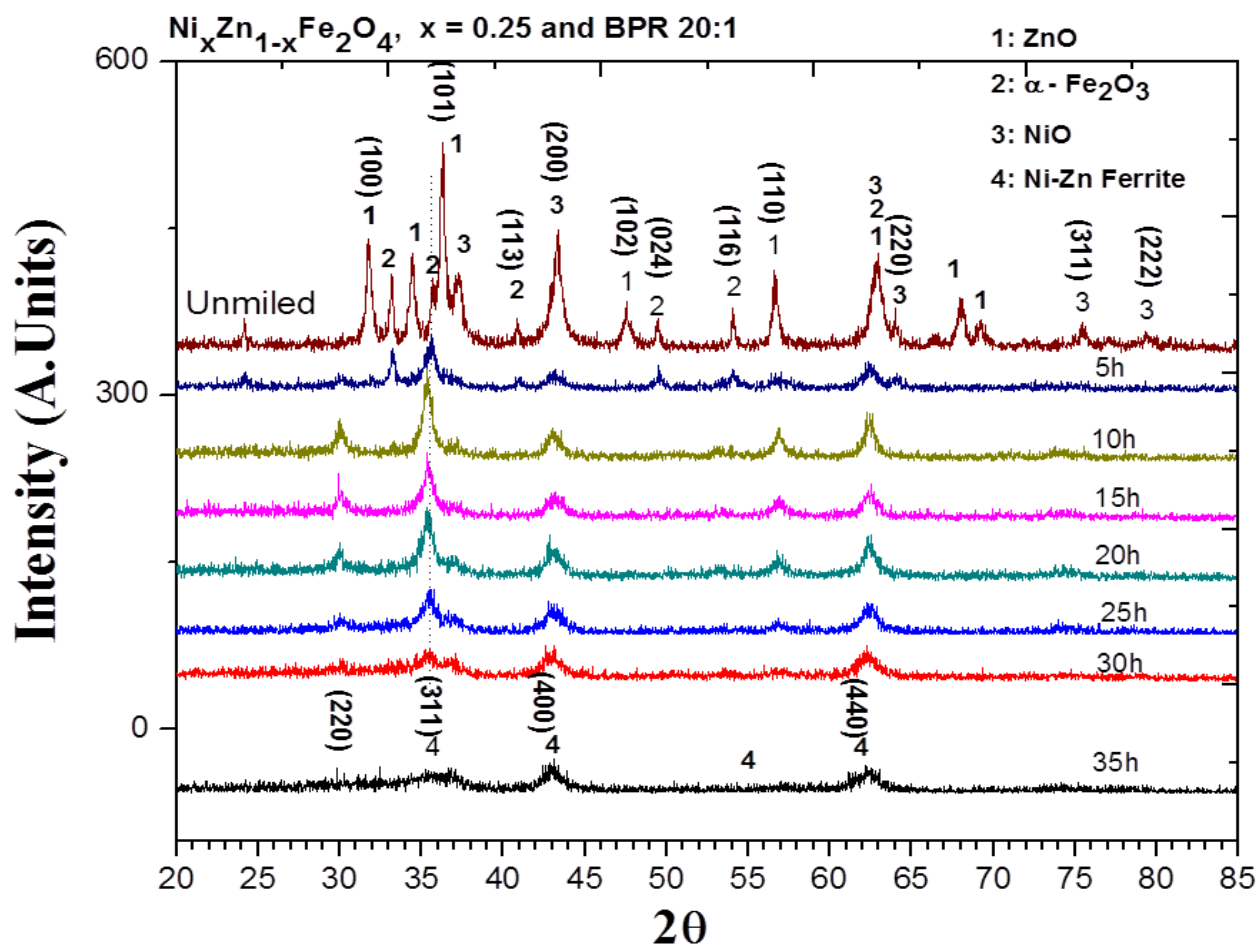
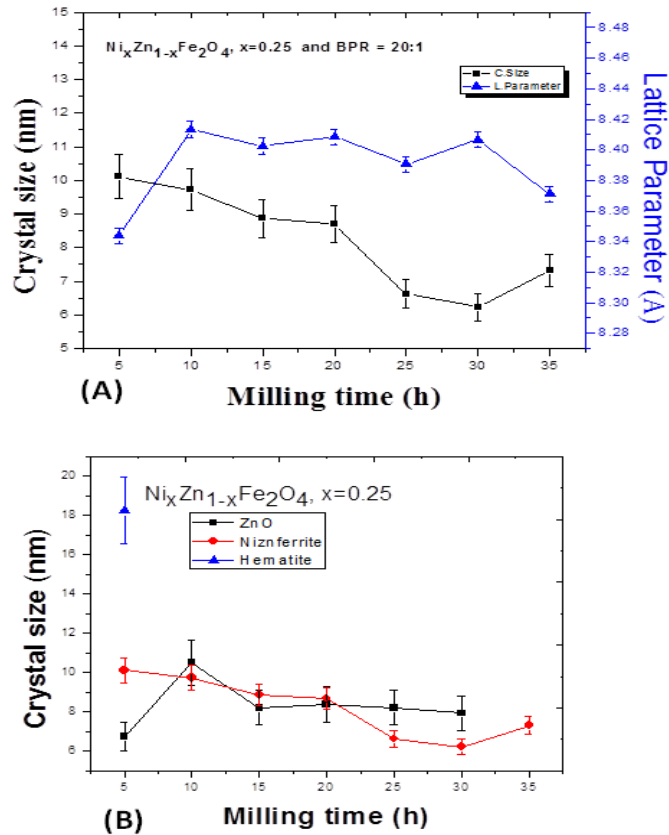


Figure 48: XRD spectral measurements of mechano-chemical synthesis of  $\text{Ni}_x\text{Zn}_{1-x}\text{Fe}_2\text{O}_4$ ,  $x = 0.25$  and BPR = 20:1 in the range of 5-35h of milling time.



**Figure 49: Crystal size and lattice parameter as function of milling time for the synthesis of  $Ni_xZn_{1-x}Fe_2O_4$  with  $x = 0.25$  and BPR = 20:1.**

Figure 50 shows the strain as a function of milling time, and we can observe that the average strain increased as time evolved, presenting only a decrease for 35h of milling time. As depicted in Figures 49 and 50, we can also note that the average strain can be relate to be proportional to the average crystal reduction. The average strain value was 0.0142 mm/mm while in Table 10, we show the average crystal size, as well, as both the average lattice parameter and the average lattice strain corresponding to this synthesis.

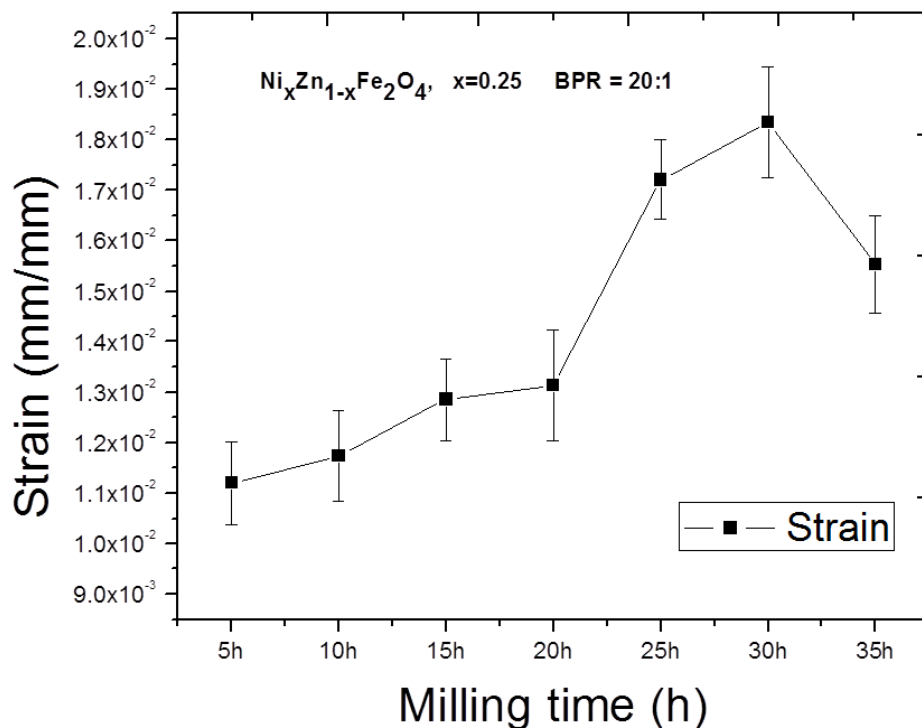


Figure 50: Strain as function of milling time for  $\text{Ni}_x\text{Zn}_{1-x}\text{Fe}_2\text{O}_4$  with  $x=0.25$  and BPR: 20:1

Table 10: Average lattice parameter “ $a$ ”, crystal size “ $d$ ” and average strain for  $\text{Ni}_x\text{Zn}_{1-x}\text{Fe}_2\text{O}_4$  with  $x=0.25$  and BPR= 20:1

Milling time (h)	$\text{Ni}_x\text{Zn}_{1-x}\text{Fe}_2\text{O}_4$ with BPR=20:1 and $x = 0.25$		
	Crystal size* “ $d$ ” (nm)	Lattice parameter (Å)	Average Strain (mm/mm) × 10 <sup>-3</sup>
5	10.11	8.3437	11.20
10	9.73	8.4134	11.73
15	8.87	8.4026	12.86
20	8.69	8.4083	13.14
25	6.62	8.3906	17.21
30	6.23	8.4067	18.34
35	7.32	8.3710	15.53
40			
50			
60			
Average	8.23	8.3909	14.29

\* Determined from (311)  $\text{ZnFe}_2\text{O}_4$  reflection with Debye-Scherrer formula.

### 5.1.2. VSM measurements

The results of the VSM measurements of all the  $\text{Ni}_x\text{Zn}_{1-x}\text{Fe}_2\text{O}_4$  with  $x = 0.25$  milled to different times are depicted in Fig. 51. We can observe that as the coercivity showed an increasing trend from 2.19 up to 3.4 mT as the milling time evolved from 5 until 35 hours of milling time, except for the 20h case where the value of coercivity was down. This trend in coercivity was related earlier to the anisotropy when the crystal size is reduced to the dimensions of the domain wall width. [40]. With respect to the magnetization, we can observe that initially, it exhibited an increase within the 5h and 10h of milling time. After this time, the magnetization showed a clear trend of decrease in value with time until 35h of milling. The initial value for 5h is  $12.9 \text{ Am}^2/\text{Kg}$  while for the 10h of milling, the value is  $44.5 \text{ Am}^2/\text{Kg}$  and subsequently it decreased continuously decreasing until  $12.7 \text{ Am}^2/\text{Kg}$ . Similar trend in the magnetization was been observed by Urcia and attributed this behavior to the promotion of random spin canting on the crystal surface [81]. In Fig. 52 we can observe both coercivity and magnetization as a function of milling time evolution for the mechanochemical synthesis of Ni-Zn ferrite based on BPR of 20:1. The table 11 summarizes the values for both coercivity and magnetization for the mechanochemical synthesis of  $\text{Ni}_x\text{Zn}_{1-x}\text{Fe}_2\text{O}_4$  for the  $x = 0.25$  and BPR = 0.25.

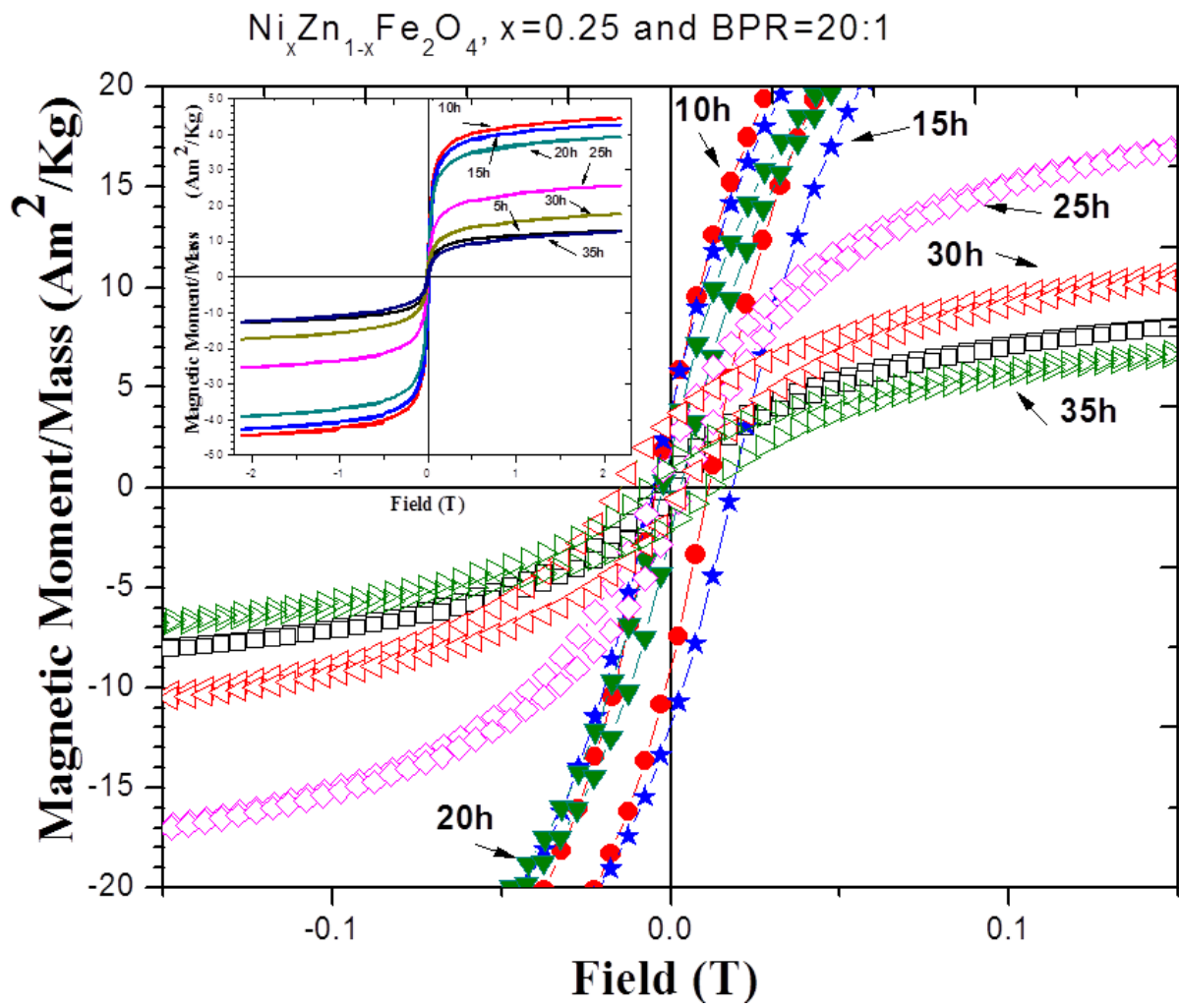


Figure 51: Hysteresis loop for the synthesis of  $\text{Ni}_x\text{Zn}_{1-x}\text{Fe}_2\text{O}_4$  with  $x = 0.25$  synthesized by HEBM and BPR=20:1.

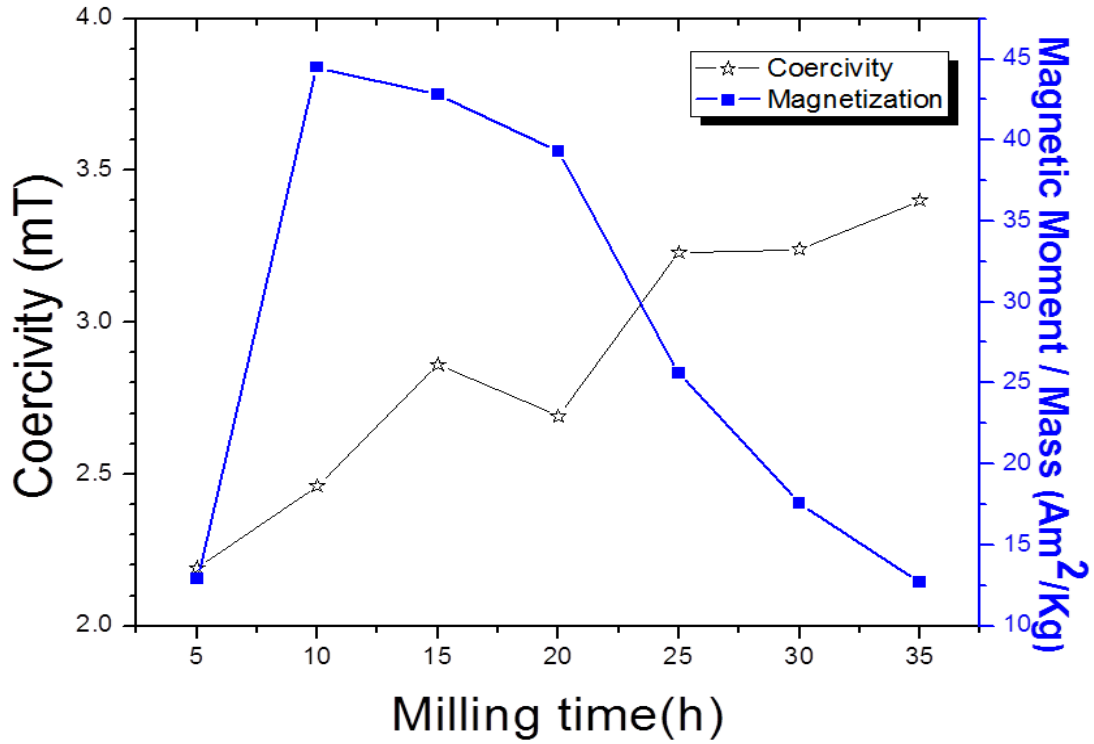


Figure 52: Coercivity and Magnetization as function of milling time for  $Ni_xZn_{1-x}Fe_2O_4$  with  $x=0.25$  synthesized by HEBM and BPR=20:1

Table 11: Values for coercivity and magnetization as a function of milling time for the synthesis of  $Ni_xZn_{1-x}Fe_2O_4$  with  $x = 0.25$  and BPR= 20:1

Milling time (h)	$Ni_xZn_{1-x}Fe_2O_4$ with BPR=20:1 and $x = 0.25$	
	Coercivity (mT)	Saturation magnetization (Am <sup>2</sup> /Kg)
5	2.19	12.91
10	2.46	44.54
15	2.86	42.77
20	2.69	39.28
25	3.23	25.58
30	3.24	17.60
35	3.40	12.70
40	-	-
50	-	-
60	-	-

### 5.1.3. Mössbauer measurements

Fig.53 shows room temperature Mössbauer spectrum for all materials corresponding to the synthesis of  $\text{Ni}_x\text{Zn}_{1-x}\text{Fe}_2\text{O}_4$  by ball-milling of  $\text{ZnO}/\text{NiO}/\alpha\text{-Fe}_2\text{O}_3$  mixture, with BPR=20:1. We can observe the presence of a sextets peaks around within  $\pm 8$  mm/s, and non-sextet peaks within the central region in the velocity range of  $\pm 2$  mm/s. We can note, from the figure, that the sextet almost disappeared for 10h of milling time. In other words, the sextet decreased in intensity due to ball milling time, while the central portion of the spectra progressively increased. This effect is commonly related to relaxation behavior which [53] as was seen in the preceding sections of 4.1, 4.2 and 4.3. Similar to the previous cases, we can observe that, due to the milling time, the six-line collapsed in a superparamagnetic doublet in the Mössbauer spectrum. The superparamagnetic doublet appears only when  $\tau$  is shorter than 10 ns. This doublet corresponds to the quadrupole splitting of nuclear energy levels [50].

The 5 hours ball milled state showed both the presence of the sextet hematite precursor, and pronounced non-magnetic peaks associated with the mechanochemical reaction process. The sextet peaks showed that the outer most peak to be more intense than the middle, with the inner-most peaks least intense, despite that overall, they did not have the expected 3:2:1 ratio that characterizes randomly grains of the reference  $\alpha\text{-Fe}$  absorber. The LHS peak associated with the middle doublet is clearly more intense than the RHS peak.

The 10 hours milled state displayed overlapping sextet collapsing peaks, with the internal magnetic fields clearly less than the highest internal magnetic field of the hematite precursor material. The central portion showed very broad peak, with the LHS peak centered within the zero velocity scale. The very broadened background with diminished in intensity for the 20, 25,

and 30 hours milled states respectively. In the 25, 30, and 35 hours milled states, the asymmetry of the non-magnetic peaks evolved slightly or not all based on visual inspection. In conclusion, the background of the 35 hours milled state clearly suggested that the complete conversion of the solid precursors to a new material phase occurred.

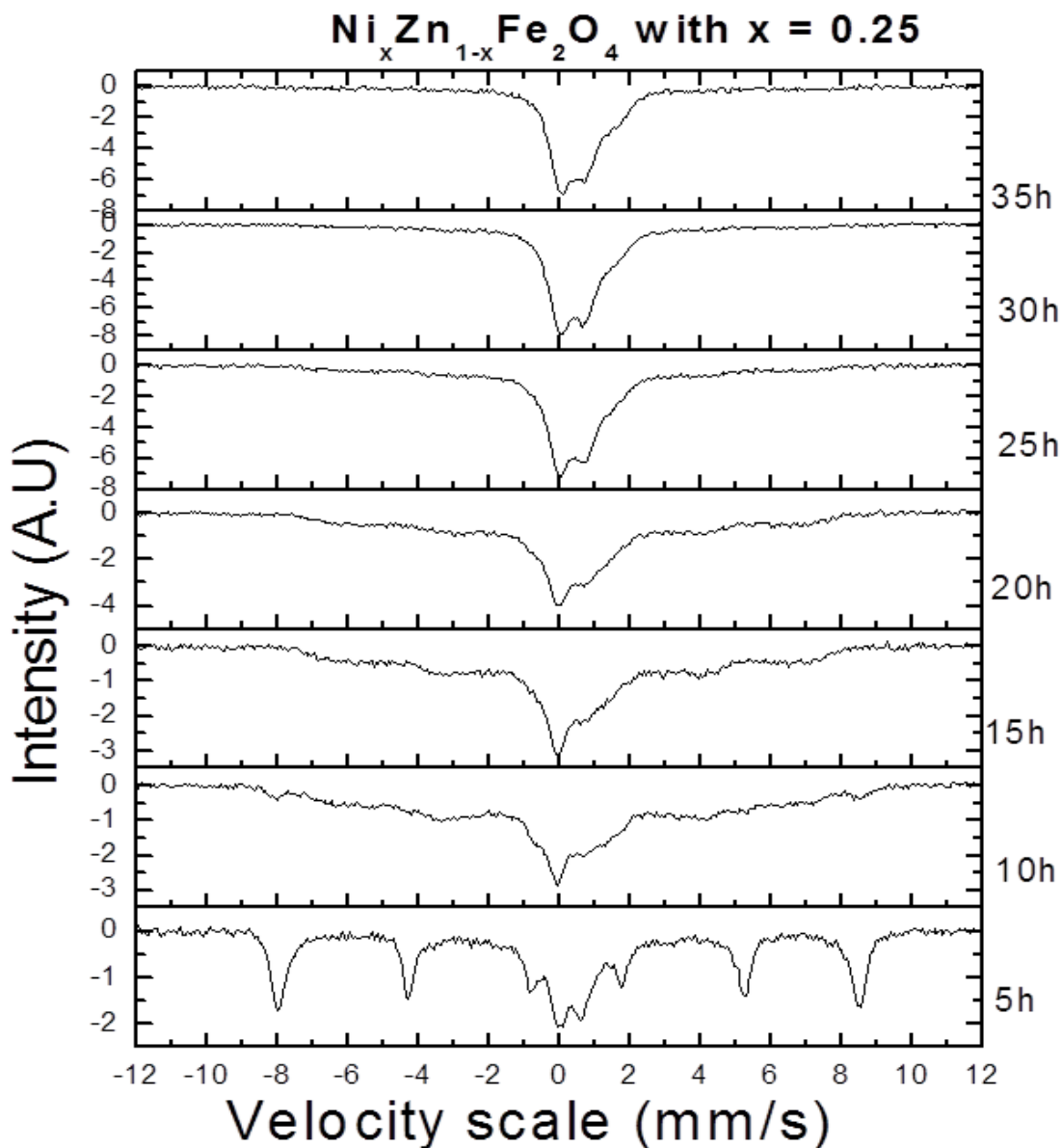
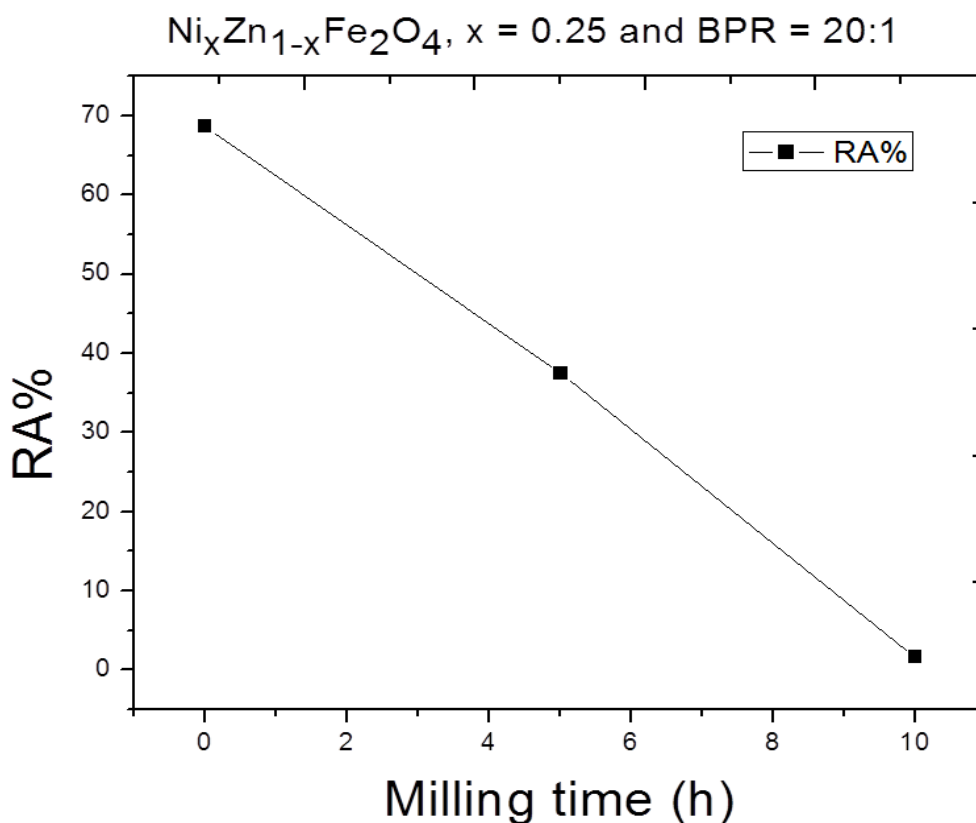


Figure 53: Mössbauer measurements for  $\text{Ni}_x\text{Zn}_{1-x}\text{Fe}_2\text{O}_4$  with  $x = 0.25$  synthesized by HEBM and BPR = 20:1

The Mössbauer spectrum for the 5h of milling time was initially fitted with a site whose internal magnetic field value was of 508.62 kOe. This value for hematite phase was for the first 5h of milling. For the next 5h of milling, the internal magnetic field value was about 512 kOe and relative abundance of about 1.66%, thereby signifying that the mechanochemical reaction neared completion at this stage. We can observe from the above figure that the spectrum consist mainly a central doublet and hematite traces are not visible. The Fig. 54 shows the evolution of hematite phase in a function of milling time. We can see that for 10h of milling the amount of hematite had gone.



**Figure 54: Relative abundance of hematite as a function of milling time during the synthesis of the solid solution of  $\text{Ni}_x\text{Zn}_{1-x}\text{Fe}_2\text{O}_4$  with  $x = 0.25$ , using a BPR of 20:1**

## 5.2. Synthesis of $\text{Ni}_x\text{Zn}_{1-x}\text{Fe}_2\text{O}_4$ for $x = 0.75$

### 5.2.1. XRD measurements

In Figure 55 we display the XRD pattern of the un-milled material together with those after different milling times. As in the previous case, the XRD peaks of NiO, ZnO and hematite exhibited broadening with intensities reduced, during the ball milling. After 30h of milling time, almost all precursor peaks have disappeared and the XRD pattern mainly included the peaks corresponding to the Ni-Zn ferrite. We can observe only traces of ZnO in approximately  $2\theta = 56^\circ$  with the synthesis completed after 35h of milling time. The crystal size was determined by Scherrer's equation using the (311) reflection. The average crystal size was 8.16 nm, while it ranged between 6.14 and 10.18 nm. This value is slightly less than those found in the section 5.1.1. The trend in the crystal size can be observed in the Fig. 56 (A). For 5h of milling time the crystal size was 10.18 nm, while it decreased continuously until 6.14nm after 35h of milling time. In the Fig. 56 (B) we can see the evolution of the precursor materials compared with zinc ferrite phase. While, the crystal size of zinc ferrite phase decreased with the milling time, the other phases showed a trend to decrease but not continuously if not that they showed a slow increase in the first hours of milling time. For example, ZnO phase. Decreased from 5 up to 10h of milling, and for 15h of milling time it showed a slightly increase. After this time it decreased continuously up to 30h of milling. With respect to the hematite phase, only is showed the evolution for the crystal size for the 5 and 10h of milling time, due to that was not possible select the peaks belonging to this phase since they had extremely low intensity to select them and calculate the crystal size corresponding .

The variation of lattice parameter of Ni-Zn ferrite phase with increasing milling time is also observed in the Fig. 56 (A). It can be noted from the figure that lattice parameter vary

nonlinearly. From 5 to 10h the lattice parameter shows large changes in its value. From 10h to 15h the lattice parameter decreased, followed by increasing slowly until 30h and finally decreased for the last five hours of milling time. This variation can be due to accumulation of strain as was mentioned earlier.

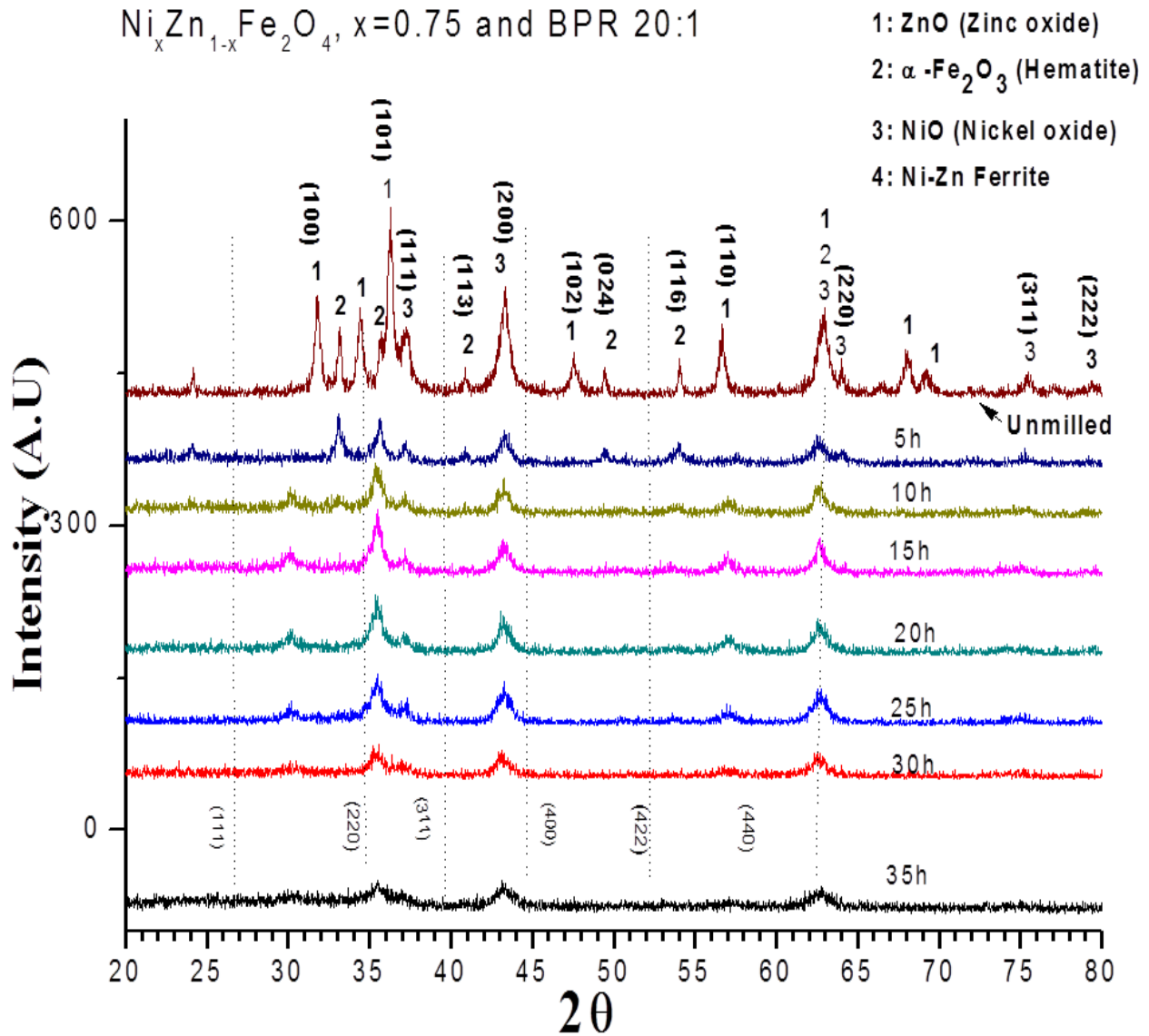


Figure 55: XRD spectra for  $\text{Ni}_x\text{Zn}_{1-x}\text{Fe}_2\text{O}_4$  with  $x = 0.75$  synthesized by HEBM with BPR=20:1

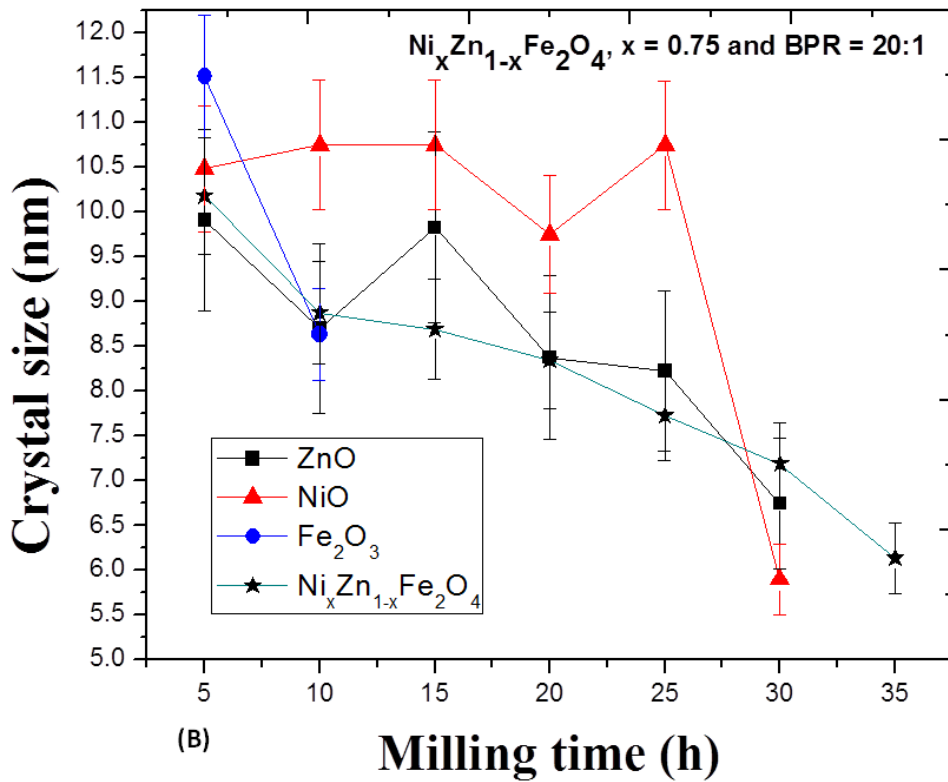
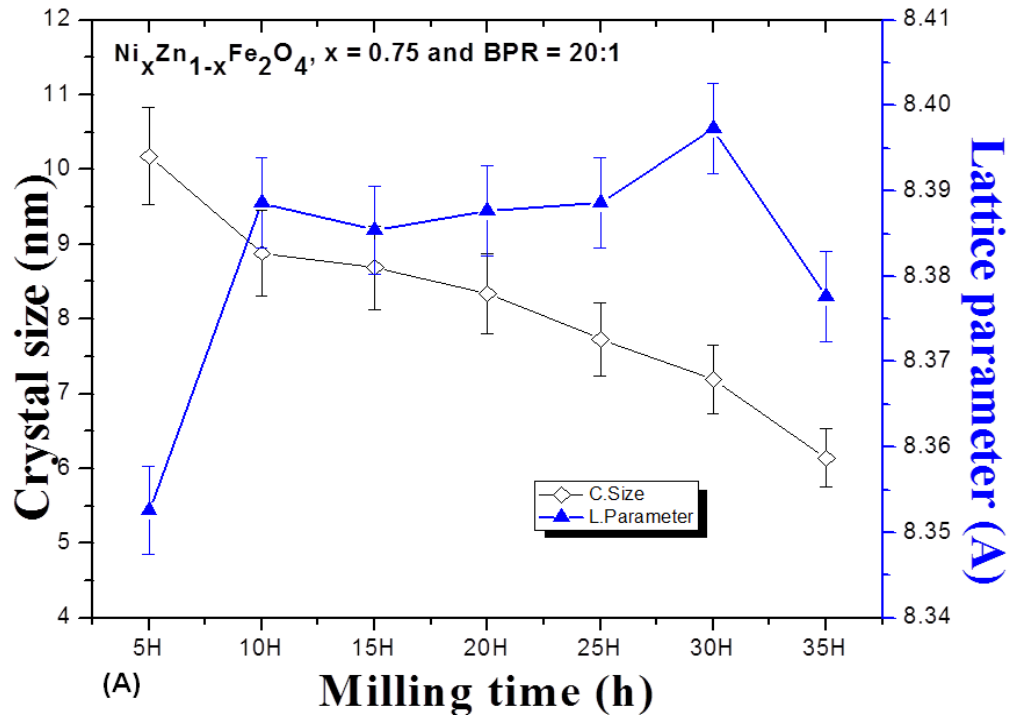


Figure 56: Crystal size and lattice constant as function of milling time during the synthesis of the solid solution  $\text{Ni}_x\text{Zn}_{1-x}\text{Fe}_2\text{O}_4$  with  $x=0.75$  synthesized by HEBM and BPR=20:1

The average strains associated with the formation of single solid solution phase  $\text{Ni}_x\text{Zn}_{1-x}\text{Fe}_2\text{O}_4$  with  $x=0.75$  showed progressive increase from 5h up to 35h of milling time. Together with the evolution of the average particle size, it is evident that decreased particle size was accompanied by overall increase of average strain which is depicted in the Fig. 57. Table 12, summarizes the values for crystal size, lattice parameter and average strain.

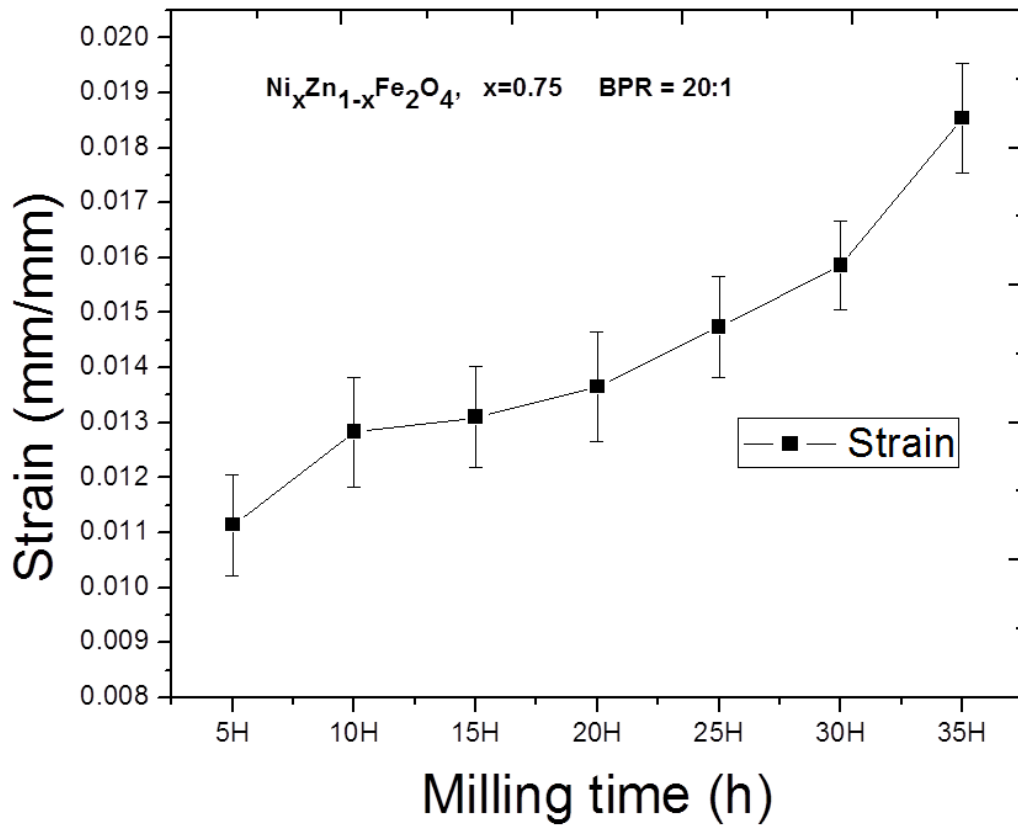


Figure 57: Average strain as a function of milling time for  $\text{Ni}_x\text{Zn}_{1-x}\text{Fe}_2\text{O}_4$  with  $x=0.75$  and BPR=20:1

**Table 12: Average lattice parameter “a”, crystal size “d” and average strain for Ni<sub>x</sub>Zn<sub>1-x</sub>Fe<sub>2</sub>O<sub>4</sub> with x=0.75 and BPR = 20:1.**

Milling time (h)	Ni <sub>x</sub> Zn <sub>1-x</sub> Fe <sub>2</sub> O <sub>4</sub> with BPR=20:1 and x = 0.75		
	Crystal size* “d” (nm)	Lattice parameter (Å)	Average Strain (mm/mm) x 10 <sup>-3</sup>
5	10.18	8.3526	11.14
10	8.88	8.3886	12.83
15	8.69	8.3854	13.10
20	8.34	8.3877	13.65
25	7.73	8.3886	14.74
30	7.19	8.3973	15.86
35	6.14	8.3776	18.54
40			
50			
60			
Average			

\* Determined from (311) ZnFe<sub>2</sub>O<sub>4</sub> reflection with Debye-Scherrer formula.

### 5.2.2. VSM measurements

The results of the VSM measurements at room temperature for all the Ni<sub>x</sub>Zn<sub>1-x</sub>Fe<sub>2</sub>O<sub>4</sub> with x = 0.75 materials milled for different times are depicted in Figure 58 and the Figure 59, where we can observe the behaviors for both coercivity and magnetization properties. The coercivity showed a decreasing trend from 4.2 mT up to 2.43 mT as the milling time evolved from 5 until 35 hours of milling time. We can observe as for 10h of milling time that the coercivity dropped to 3.7 mT, while after this time, it increased to 4.1 mT and thereafter it decreased until after 35h of milling time where the coercivity reached the least value above mentioned. The coercivity in this case followed the general tendency of decrease as it reached the superparamagnetic phase. According to Chicinas [40], this behavior is accompanied by a low permeability. The saturation magnetization showed an increase until the first 15h of milling time. It increased to 5.3 Am<sup>2</sup>/Kg until 43.3 Am<sup>2</sup>/Kg. After this time, the magnetization continuously decreased, and, it reached a value of 12.9 Am<sup>2</sup>/Kg.

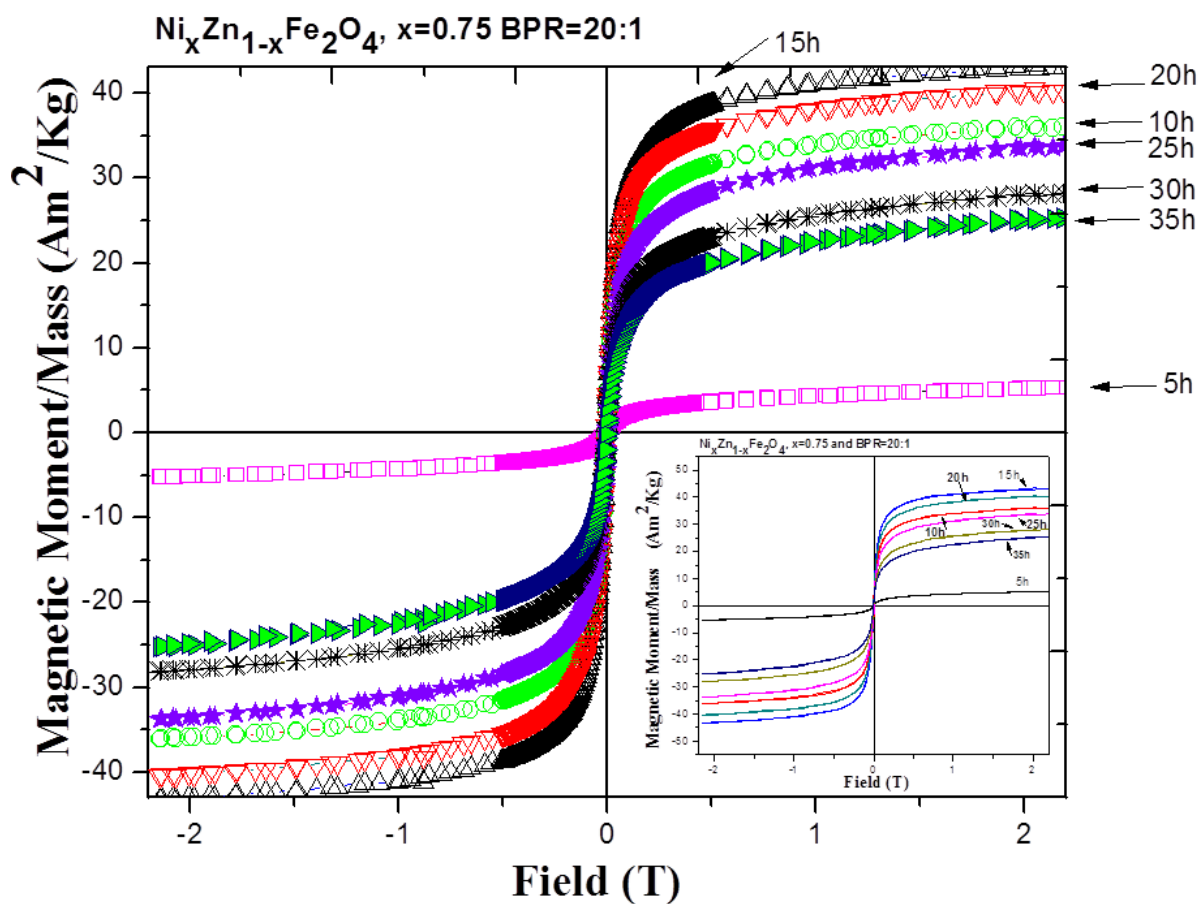
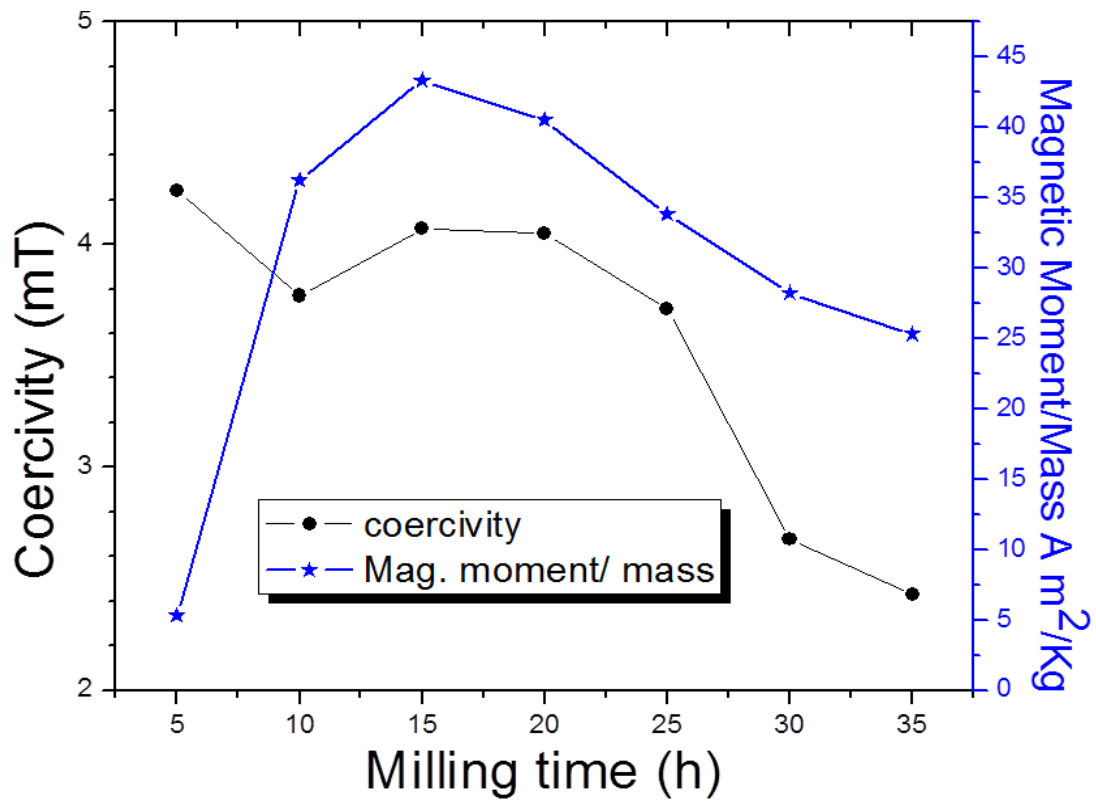


Figure 58: Hysteresis loops associated with the synthesis of  $\text{Ni}_x\text{Zn}_{1-x}\text{Fe}_2\text{O}_4$  with  $x = 0.75$  by HEBM using BPR = 20:1



**Figure 59: Coercivity and saturation magnetization as a function of milling time for  $\text{Ni}_x\text{Zn}_{1-x}\text{Fe}_2\text{O}_4$  with  $x = 0.75$  synthesized by HEBM and BPR = 20:1.**

Table 13 summarizes the results for both coercivity and saturation magnetization values as a function of milling time are displayed. We can observe the minimum and maximum values for coercivity and magnetization which were 2.43 mT and 43.35 Am<sup>2</sup>/ Kg.

**Table 13: Values for coercivity and magnetization as a function of milling time for  $\text{Ni}_x\text{Zn}_{1-x}\text{Fe}_2\text{O}_4$  with  $x = 0.25$  and BPR = 20:1.**

Milling time (h)	$\text{Ni}_x\text{Zn}_{1-x}\text{Fe}_2\text{O}_4$ with BPR=20:1 and $x = 0.75$	
	Coercivity (mT)	Saturation magnetization ( $\text{Am}^2/\text{Kg}$ )
5	4.24	5.29
10	3.77	3.68
15	4.07	4.33
20	4.05	4.05
25	3.71	3.38
30	2.68	2.82
35	2.43	2.52
40		
50		
60		
Average		

### 5.2.3. Mössbauer measurements

The Mössbauer measurement of all material samples for  $\text{Ni}_x\text{Zn}_{1-x}\text{Fe}_2\text{O}_4$  with  $x = 0.75$  and BPR = 20:1 are displayed in the Figure 60. The spectra corresponding to the 5, 10, 15, 20, 25, 30, and 35-hours ball milled states for the solid solution  $\text{Ni}_{0.75}\text{Zn}_{0.25}\text{Fe}_2\text{O}_4$  showed progressive evolution of the spectra based on the identification of the initial starting material hematite ( $\alpha\text{-Fe}_2\text{O}_3$ ) used in the mechanochemical reaction syntheses. The gradual diminution of hematite with ball milling is very evident from five hours of ball milling. Close examination of the 5-hour ball milled material showed that the prominent change was reflected by the formation of non-sextet peaks located in the central portion of the spectrum. The asymmetric doublet peaks are flanked by the well resolved sextet peaks associated with the hematite phase.

The central doublet accounted for about 33.57% in relative abundance of the material mixture.

The sextets were resolved in terms of three sub sites with internal magnetic fields of 446.00 kOe, 511.85 kOe, and the component with 481.43 kOe. The relative abundances of these sites were determined to be 20.92%, 40.34%, and 5.18% respectively.

In contrast to the 5 hour ball milled state, the 10-hour ball milled spectrum, is made of more sextet peaks in addition to the hematite peaks that sandwiched the newly evolved sextets, and the central asymmetric peaks. The broad nature of the newly evolved sextets suggested that they are due to the overlapping peaks arising from different Fe states. The non-sextet central asymmetric peaks accounted for 47.02% of the total spectrum, indicating that the mechanochemical synthesis process was progressive, since the well resolved hematite with the highest internal magnetic field of 511.71 kOe, accounted for about 12.02% as opposed to its abundance of 40.34% in the five hour-ball milled state.

Further, in the 15 hour ball milled state, the hematite phase, while discernible in the spectrum, had decreased to a relative abundant value of 1.95%, thereby signifying that the mechanochemical reaction neared completion at this stage. While the non-hematite sextet peaks increased in broadening, the central asymmetrical portion, increased in relative abundance to a value of 50.54%. The trend observed thus far with the evolution of the hematite material with internal magnetic field of 511.27kOe, and the central doublet can be used to deduce the effect of the progressive ball milling of the material mixture. This more so because, the sextet site with internal magnetic field value of 461.58kOe, remained fairly constant in its relative abundance in the range of 4-5.00%. For the next five hours, i.e., the 20 hours ball milled state, while the hematite site is merely discernible, the spectra was fitted with four sites as in the three previous cases. The slight or marginal difference between the relative abundance of the 511.11 kOe

hematite state which was 1.95%, and 1.39% in the 20 hours state seemed to suggest that the mechanochemical process slowed down, while most of the impact of the ball milling process was centered on the local structural evolution of the synthesized composite mixture. This is because the relative abundance of the central doublet increased to 57.50% from the previous value of 50.54%. Therefore, the change in the relative amount of the hematite did not account for the accompanying change in the relative abundance of doublet.

Following further milling, at 25 hours, the fitting of the spectrum with four-sites clearly showed that the internal magnetic fields of the three sextets clearly were different from the prominent hematite phase that served in tracking the mechanochemical synthesis. This is because, the site with the highest internal magnetic field now stood at 564.63kOe, which was clearly higher than the 511.00-512.00kOe value for the precursor hematite. The relative abundance for the site was 2.22%. The doublet central asymmetric portion accounted for 64.80% in relative abundance. This suggested that the mechanochemical synthesis resulted in the formation of composite materials made of different spinel phases, while on the basis of particle-size distribution; distinction could not be made easily between the super-paramagnetic contributions from the different spinel structured phases.

A marked difference was recorded for the 30-hours milled state, which closely looked like the 25-hours milled state. In this case, the notable difference was in the site with the highest internal magnetic field of 540.67kOe, in contrast to its value of 564.63kOe in the 25 milled state. Its relative abundance remained same at 2.59%. This suggested that local re-structuring of the cations occurred, since a sextet with internal magnetic field of 369.85kOe accounting for 34.29%

of the spectrum in relative abundance was deduced. The relative abundance of the doublet portion was 58.14% from the 64.80% it was in the 25 hours milled state.

Lastly, the 35 hours milled state, showed the spectrum to be largely made up of the doublet, with slight amount of the sextet portions. The large broadened areas of the sextets indicated that structurally, there was not much difference between the materials in the 30 hours and 35 hours milled states. The doublet decreased in intensity or relative abundance to 50.82%, while the a sextet with an internal magnetic field of 333.25kOe accounting for about 39.98% in relative abundance showed that this was  $\alpha$ -Fe substantially (given that the reference Fe had an internal magnetic field of 330kOe). In contrast, the sextet with 568.45kOe accounted for 4.02%, with the sextet with 427.33kOe accounted for 5.17%. The formation Fe could be attributed to surface effects, due to preferential reduction of surface atoms. The figure 61 shows the evolution of hematite as a function of milling time.

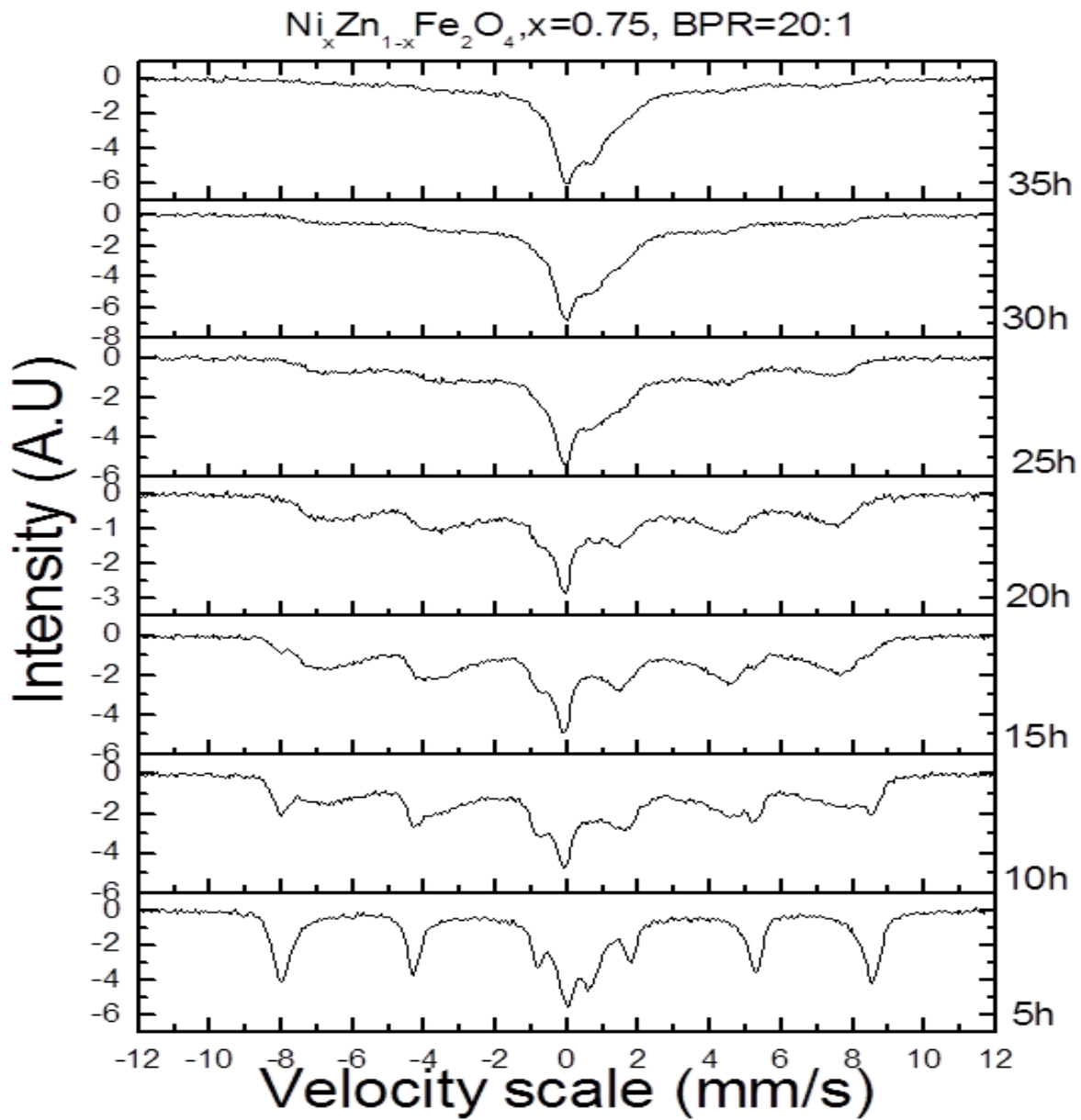
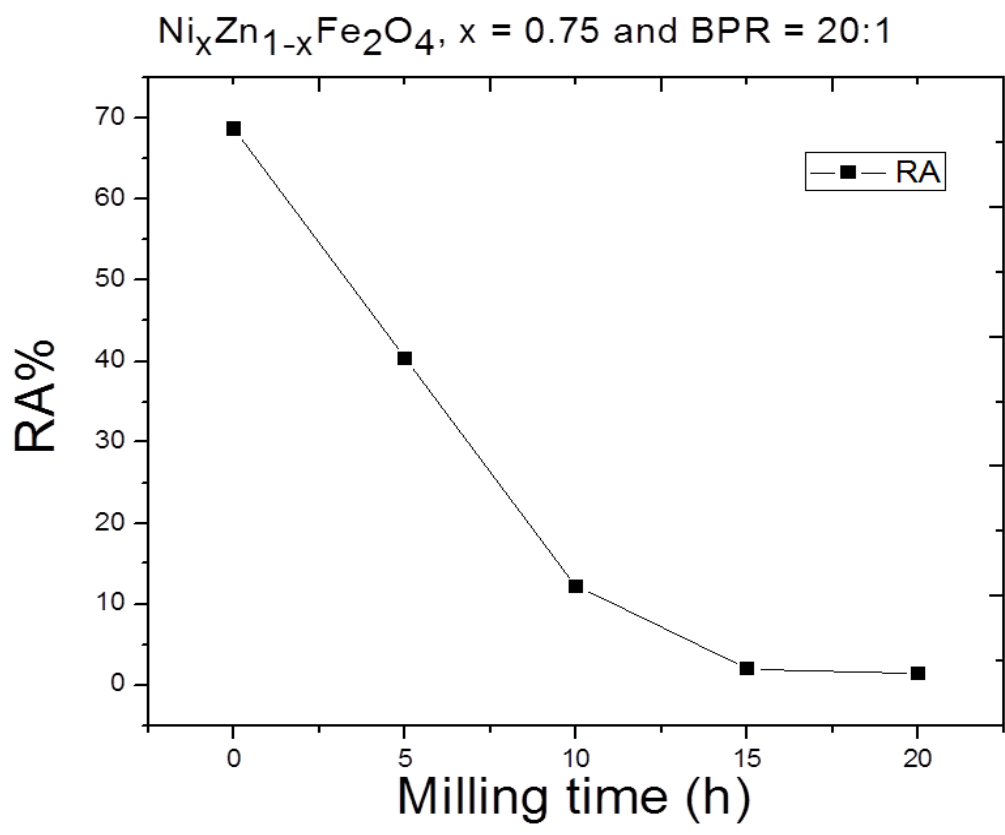


Figure 60: Mössbauer spectra of  $\text{Ni}_x\text{Zn}_{1-x}\text{Fe}_2\text{O}_4$  with  $x = 0.75$ , ball-milled  $\text{ZnO}-\alpha\text{-Fe}_2\text{O}_3$  mixture with BPR=20:1.



**Figure 61:** Relative abundance of hematite as a function of milling time during the synthesis of the solid solution of  $\text{Ni}_x\text{Zn}_{1-x}\text{Fe}_2\text{O}_4$  with  $x = 0.75$ , using a BPR of 20:1

## 5.3. General discussion

### 5.3.1. XRD measurements

In the previous sections we described the structural properties derived from the XRD measurements for the samples of Zinc ferrite and the Ni-Zn ferrite. The first of them,  $\text{Ni}_x\text{Zn}_{1-x}\text{Fe}_2\text{O}_4$ ,  $x = 0$  or simply  $\text{ZnFe}_2\text{O}_4$ , was described in section 4.31 and the second were described in sections 5.1.1, and, 5.2.1 for the cases of  $x = 0.25$  and  $x = 0.75$  respectively. Now, we show in more details some aspects of the syntheses mentioned above. In Figure 62 we can observe the XRD spectra for Ni-Zn ferrite with concentrations of  $x = 0.25$ ,  $x = 0.75$ ,  $x = 0$  and the milling times necessary to achieve the formation of the spinel phases in each case by HEBM. We can observe that the characteristic peaks of the spinel phase for each, namely, with  $x = 0$ ,  $x = 0.25$  and  $x = 0.75$ . We can note different intensities for the peak, as well as, the distinct broadening which is related to the differences in the average crystal, size and, strain accumulation characteristic of HEBM.

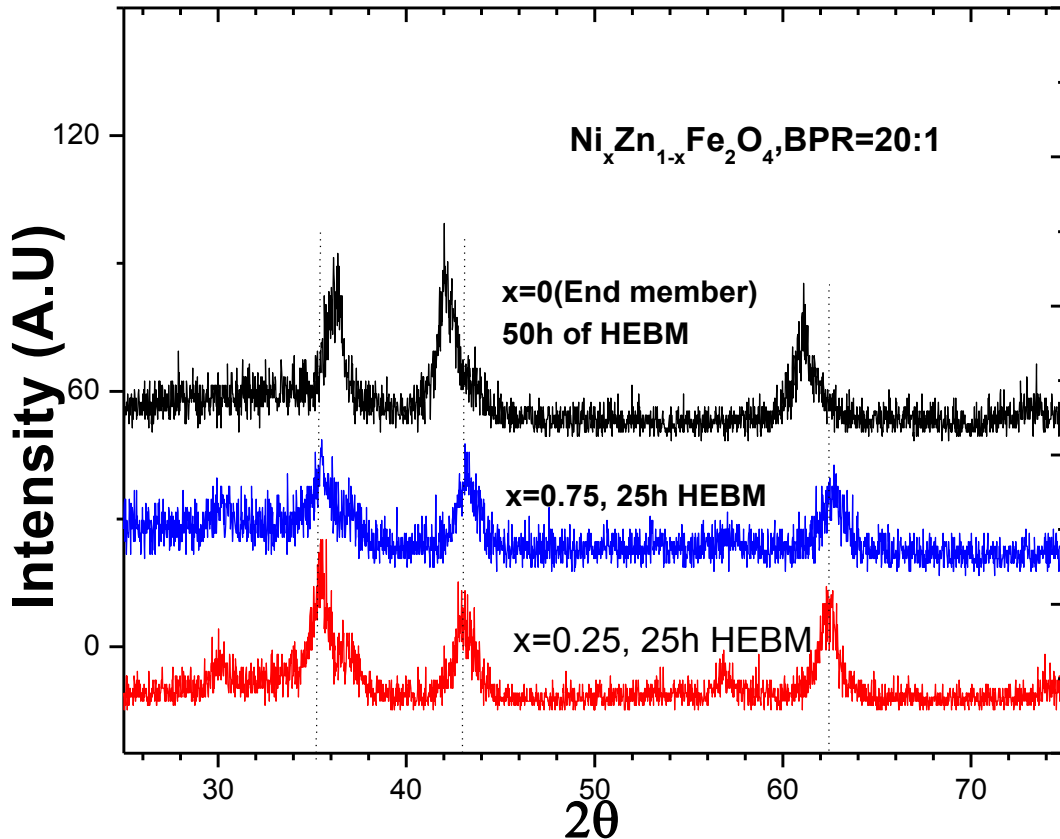
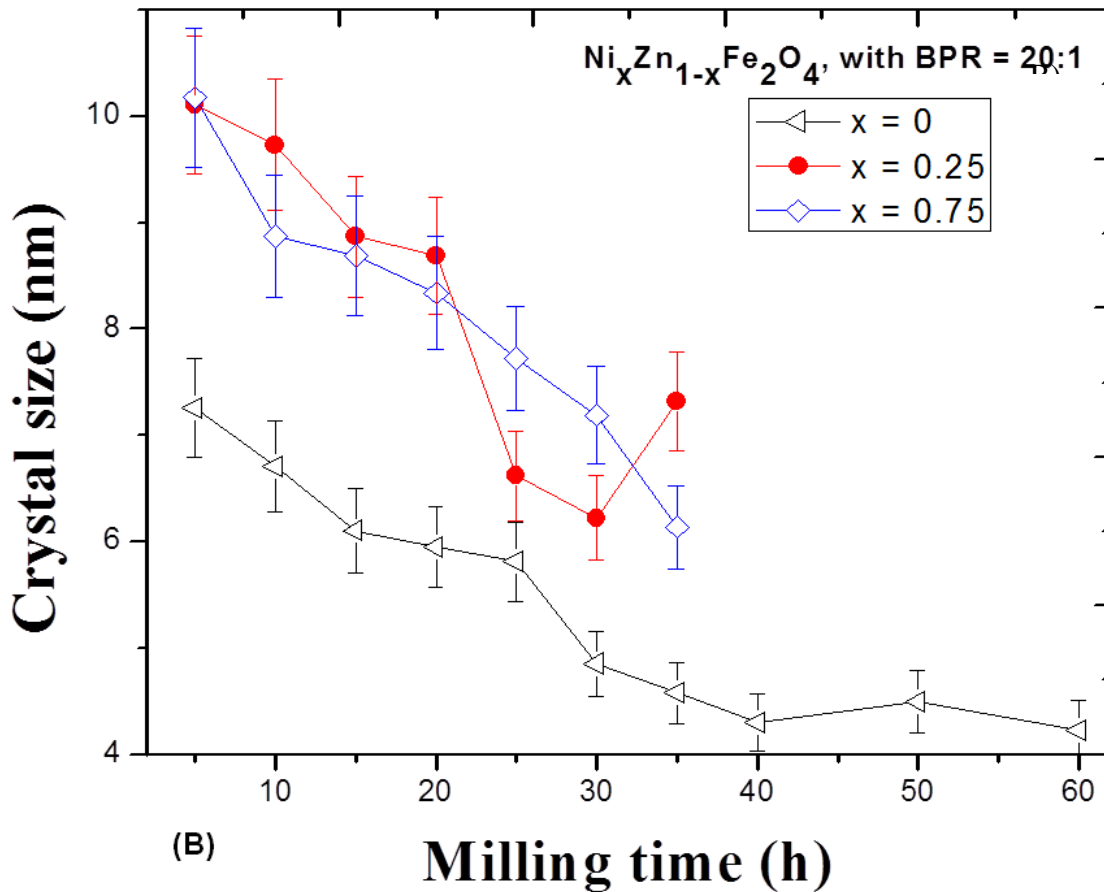


Figure 62: XRD patterns for  $\text{Ni}_x\text{Zn}_{1-x}\text{Fe}_2\text{O}_4$ , BPR = 20:1 and  $x = 0$ ,  $x = 0.25$  and  $x = 0.75$ .

From the XRD patterns, crystal size, lattice parameter, and strain for each sample were determined. The crystal size for each synthesis is shown in the Figure 63 as a function of milling time. We can note the evolution of the crystal size with the milling time for the cases  $x = 0$ ,  $x = 0.25$  and,  $x = 0.75$ . The spinel phases was reached in a lesser milling time for the case  $x = 0.25$  with 25h and a crystal size of 6.6 nm. On the other hand, for the  $x = 0$  case, we got 4.5 nm in crystal size with 50h of milling time employed to reach spinel phase, while for  $x = 0.75$  the crystal size was 6.14 nm for 35h of milling time.



**Figure 63:** The fig shows both, (A). Crystal as a function of milling time and, (B) Strain for the different concentrations, namely,  $x = 0, 0.25$ , and,  $0.75$  for the syntheses of  $\text{Ni}_x\text{Zn}_{1-x}\text{Fe}_2\text{O}_4$  and BPR=20:1.

The study about strain revealed that for the synthesis of  $\text{Ni}_x\text{Zn}_{1-x}\text{Fe}_2\text{O}_4$ , BPR = 20:1, with  $x = 0$ , (end member) exhibited higher values of average strains, than for the cases of  $x = 0.25$  and  $x = 0.75$ . Further, the values for  $x = 0.25$  were generally higher than the values obtained for the  $x = 0.75$  case. From the study of the strain as a function of milling time, we can say that higher average strain was reached for the case  $x = 0$ , and could be directly related to the smaller average crystal size associated with this composition. From figures 63 for the crystal size as a function of

milling time and those seen in the figures 33, 50, 57, and tables 5,10 and 12, we can conclude that the increase in the strain is correlated with the average crystallite reduction. The lattice parameter did not show a clear trend, since its behavior is observed to be random with this due to possible disorder introduced by HEBM. Moreover, according crystal size, we can say that that nickel presence or substitution in  $\text{ZnFe}_2\text{O}_4$  ( $x = 0$ ) seemed to influence to lead to smaller average crystal size when in comparison between  $x = 0.25$  and  $0.75$  composition for the mechanosynthesis of  $\text{Ni}_x\text{Zn}_{1-x}\text{Fe}_2\text{O}_4$ . In relation at this fact, other works have shown that increasing in zinc concentration can influence in the structural properties. For example, one of those works reported that crystallite size reduction was accompanied with increasing Zn concentration for the solid solution  $\text{Ni}_x\text{Zn}_{1-x}\text{Fe}_2\text{O}_4$  carried out by mean of co-precipitation route. [6], and the other one, carried out by sol-gel method reported that increasing zinc concentration was accompanied by increasing, almost linear, of the lattice constant [56]. Evidently, we can see that properties of ferrites are found to be dependent on their chemical composition and microstructure, which in turn are governed by preparation process [56].

### 5.3.2. VSM measurements

In previous sections we reported and assembled the data from the study of the magnetic properties  $\text{Ni}_x\text{Zn}_{1-x}\text{Fe}_2\text{O}_4$  materials with different concentrations corresponding to  $x = 0$ ,  $x = 0.25$ , and  $x = 0.75$ . In the figure 64, we can observe that the coercivity for  $x = 0$  showed a significant reduction compared with the other ones. Coercivity for the  $x = 0.75$  concentration

decrease slightly during the milling process, in other words, coercivity don't shows abrupt change when is compared for the  $x = 0$  case. Contrary to the  $x = 0.75$  case, the coercivity for the  $x = 0.25$  increased from 5h up to 35 of milling time without showing major changes in its value. Also, is important note that after 40h of milling, namely, 50 and 60h the coercivity increased considerably until reach  $120 \times 10^{-4} T$ . With respect to the end member case  $x = 0$ , this increased in the coercivity can be related to the increase in magnetocrystalline anisotropy. Magnetic nanoparticles of cobalt ferrite have been reported to show this behavior. According to the work of Mathew and Juang [32] . On the contrary, the  $x = 0.75$  case showed a decreasing tendency in the coercivity value as the milling time increased to get the superparamagnetic state. With respect to the saturation magnetization property the behavior did not show a similar trend for the different composition studied. For example, for  $x = 0$  the saturation magnetization increased until 40h of milling, and thereafter decreased for the 50h, and finally increased to get to the maximum value. For the case of  $x = 0.25$  the saturation magnetization increased for the 5h to 10h milled states to attain the maximum value. Beyond 10h it decreased continuously until the 35h milled state value of 3.40 mT. Similar behavior was observed for the case  $x = 0.75$ , with the saturation magnetization increasing until 15h of milling and then followed by continuous decrease until 35h, as shown in sections 4.2.2, 5.1.2.and 5.2.2.

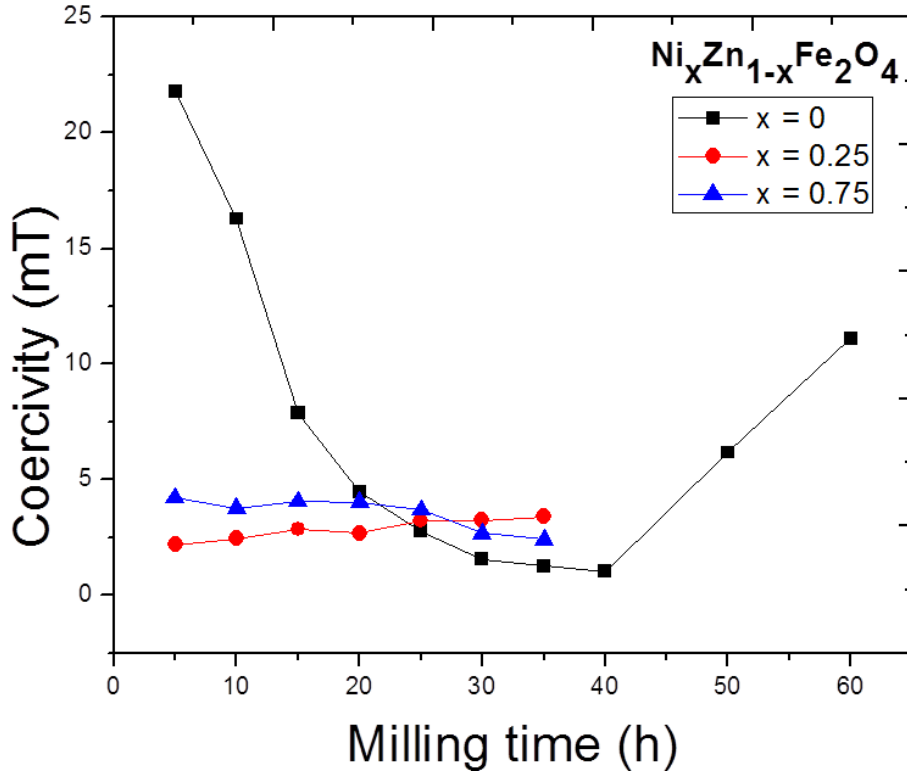
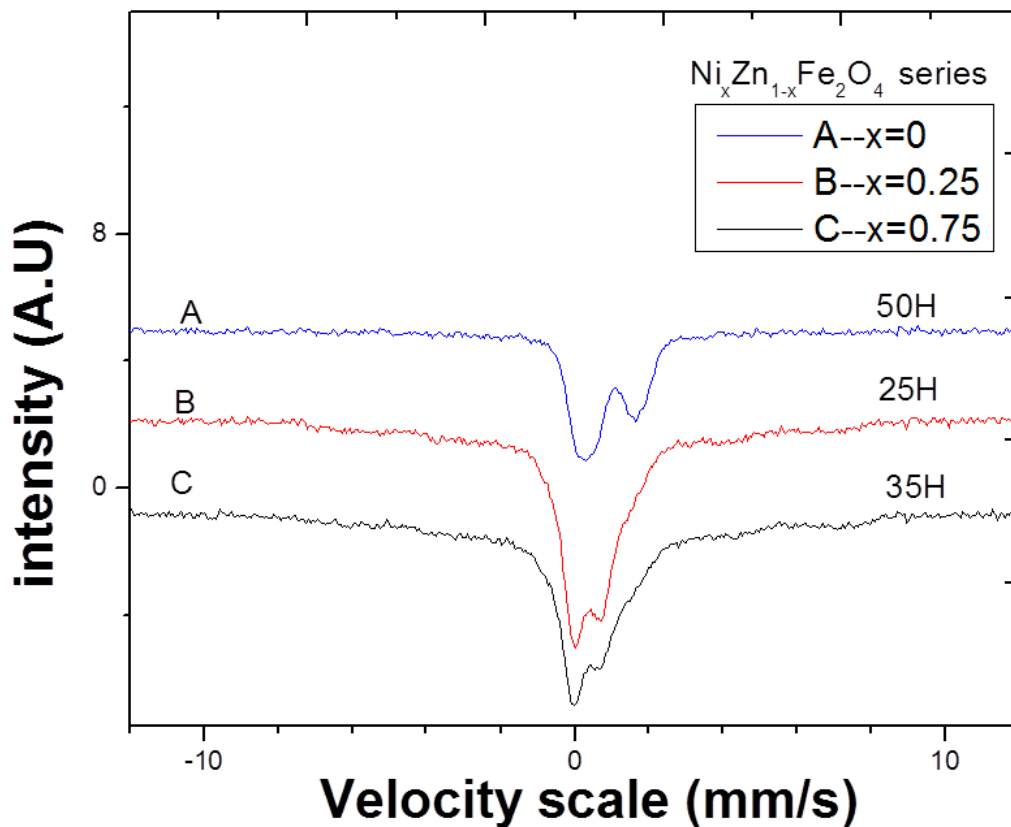


Figure 64: Coercivity variation as a function of milling time for composition of  $x = 0, 0.25$  and  $0.75$ , and BPR = 20:1

### 5.3.3. Mössbauer measurements

Mössbauer spectra for the Ni-Zn ferrite series has been displayed in the figures 36, 53 and 60, where we saw how each spectral evolution from the six-line pattern until collapse into a doublet reaching, signaling the attainment the superparamagnetic behavior. In this section we are going to compare the evolution of the Mössbauer spectra as a function of zinc/ Nickel concentration. Previously we analyzed the evolution for each synthesis with respect to the milling time, with some justifications to the respect of the behavior of the samples. For this reason, in this section, only we are only going to show the doublet obtained got in each synthesis, namely, for  $x = 0$ ,  $x = 0.25$  and  $x = 0.75$ . In the Fig.65, we observe the corresponding Mössbauer spectra, which exhibited the three doublets mentioned earlier. Each doublet signaled the attainment of the

superparamagnetism reached in different milling times, and together with differences in their overall shapes. From the figure we can note that superparamagnetic behavior was reached in the least time for  $x = 0.25$ . The time employed to get this behavior was 25h of milling, and in the  $x = 0$  case the milling time employed was of 50h. According to these results, we can say that the concentration  $x = 0.25$  was more favorable to attain faster the superparamagnetic behavior when is compared to the  $x = 0.75$  and  $x = 0$  cases.



**Figure 65: Mössbauer measurements at room temperatures for  $\text{Ni}_x\text{Zn}_{1-x}\text{Fe}_2\text{O}_4$  series, BPR=20:1 and concentrations of  $x=0$ ,  $x=0.25$  and  $x=0.75$**

For the  $x = 0$  case, the doublet is more broadened than the other ones. This fact can be due to the milling process, and we can say that different forms in the doublet depend on both BPR and Zn concentration. Moreover, the shape of the spectrum depends also on the synthesis method.

For example, Sharma et al [53], carried out a study on the synthesis of nanocomposites of Ni-Zn ferrite in aniline formaldehyde copolymer and studied their pyrolysis products at room temperature route, together with the effect of heat treatment. They found that the relaxation time depended in this case on increasing zinc concentration because it could be observed when the zinc concentration was  $x = 0.2$ . Additional zinc concentration, greater than  $x = 0.6$ , allowed obtaining of a paramagnetic doublet

Ni-Zn ferrite with concentration of  $x = 0.5$  has been carried out by three different methods, namely, Co-precipitation (Washed and Unwashed) and separate precipitation. In these cases was no possible get superparamagnetic behavior of the samples. The Mössbauer spectrum for the samples carried out by co-precipitation consisted of V-shaped spectrums (for the washed and unwashed cases) and a sharp doublet and a well defined sextet for separate precipitation (unwashed). The behavior of such as spectra can result from several effect such as reduction in magnetocrystalline anisotropy, substitution of nickel ions with those of zinc weakening the magnetic interactions due to reductions in the A-B coupling pairs and the nanosize of the sample giving a large distribution in HMF, for the first two cases and, also, can come from either fine particles of Ni-Zn ferrite or Zinc ferrite which is paramagnetic down 10K [54]. Similar system and equal concentration  $x = 0.50$  for Ni-Zn Mössbauer spectra recorded at room temperature with increasing annealing temperature shows also sextets which indicate ferrimagnetic behavior of the compounds [82]. In our cases, was possible get superparamagnetic doublet by HEBM and concentrations of  $x = 0.25$  and  $x = 0.75$  as was seen earlier. Other system of Ni-Zn ferrite with  $x = 0.58$  to Ni have related the broad shape of Mössbauer spectral lines for the nanoparticles in comparison to bulk particles to a wide distribution of magnetic fields acting at the  $\text{Fe}^{3+}$  nuclei in the nanoparticles their spectrum consisted of sextet at 5K [52]. Similar to the zinc ferrite series

as was saw earlier. Table 14 are shows the average crystal size for different synthesis methods for  $\text{Ni}_x\text{Zn}_{1-x}\text{Fe}_2\text{O}_4$  ferrite with  $x = 0.5$  composition.

**Table 14: Comparison of crystallite sizes obtained for  $\text{Ni}_x\text{Zn}_{1-x}\text{Fe}_2\text{O}_4$  for different synthesis methods**

Authors	Synthesis Method	Particle size	Superparamagnetic Phase
Bulat R. Churagulov	Hydrothermal	12-16 nm	OK
D.G. Chen	Co-precipitation	20.8 -53.3 nm	OK
Woo Hyun Kwon	Sol-gel		
Qiaoling Li	Coprecipitation	40 nm	OK

## 6. Conclusions

Different synthesis were carried out by High Energy Ball Milling where the more important parameter studied was the BPR. On the one hand was analyzed the Zinc ferrite synthesis with BPR of 10:1, 20:1 and 40:1, and on the other hand was analyzed the synthesis of  $\text{Ni}_x\text{Zn}_{1-x}\text{FeO}_4$  with concentrations of  $x=0.75$ ,  $0.25$  and  $x=0$  (End member) and BPR=20:1.

The High Energy Ball Milling technique reduced the grain size in  $\text{ZnFe}_2\text{O}_4$  until values less than 10 nm reaching superparamagnetic behavior, with increasing in structural defects which are perceived in the lattice parameters changes and the strain for each one of the samples[1].

XRD Spectrum showed Spinel phase for both samples Zinc and Nickel-Zinc ferrite, and from the analysis carried out were determined crystal size less than 7 nm and about 8,2 nm respectively. Specifically the spinel phase in each case reached crystal size of 6.73, 4.49 and 6.41 nm for BPR of 10:1, 20:1 and 40:1 respectively for the zinc ferrites series. For the Ni-Zn ferrite series the crystal size obtained were 6.14, 6.62 and 4.49 nm for the cases  $x=0.75$ ,  $0.25$  and  $0$  (end member). The changes in the lattice parameter observed are associated with the increasing strain. XRD spectrum showed the low crystallinity of the each sample due at shape of diffraction peaks which showed decreasing in its intensities and an associated broadening. This reflects the formation of the disordered state with small crystallite size and internal strain introduced during the mechanical treatment [57] The crystal reduction is observed as a consequence of broadening and reduction in the diffraction peaks which can be observed chapter 4 and 5.

BPR parameter and concentration resulted in different result in both Mössbauer and XRD measurements. The BPR 40:1 allow us get superparamagnetic phase in a lesser time that the

other ones, namely, 20:1 and 10:1. On the other hand, concentration of  $x=0.25$  for nickel in the  $\text{Ni}_x\text{Zn}_{1-x}\text{Fe}_2\text{O}_4$  allowed us obtain superparamagnetic phase in a lesser time that the  $x = 0.75$  and  $x = 0$  case. The time employed for the first of them was 25h of milling time, and for the second and third of them were 35h of milling time. With respect at these results, we can say that the BPR does not affect the final result but it only controls the speed of the reaction of the synthesis. Other factors can affect the speed of the synthesis and a example is the milling modes which is mentioned in the reference [28]

About the shape of the Mössbauer measurement, we can say that all samples exhibited superparamagnetic state. All spectrums, as was saw earlier, evolved from a six-line pattern until collapse in a superparamagnetic doublet, exhibiting the phenomenon known as superparamagnetic relaxation. This phenomenon has been observed in several work such as the showed in the references [58],[59],[60] and [57] . Also, other factors can affect the shape of Mössbauer spectrum and they have been found in other ferrites or more complex system. Some of this factors are cation distribution [61] induced mechanochemically, changes of nearest-neighbor configurations, Spin canting effects, temperature, electron and polaron hopping and some works can be found in the references [46],[47],[62],[45],[63],[18].

## References

- [1] A. Ahlawat, V. G. Sathe, V. R. Reddy, and A. Gupta, "Mossbauer, Raman and X-ray diffraction studies of superparamagnetic NiFe<sub>2</sub>O<sub>4</sub> nanoparticles prepared by sol-gel auto-combustion method," *Journal of Magnetism and Magnetic Materials*, vol. 323, no. 15, pp. 2049–2054, Aug. 2011.
- [2] O. Caltun, I. Dumitru, M. Feder, N. Lupu, and H. Chiriac, "Substituted cobalt ferrites for sensors applications," *Journal of Magnetism and Magnetic Materials*, vol. 320, no. 20, pp. e869–e873, Oct. 2008.
- [3] S. Yu, T. Fujino, and M. Yoshimura, "Hydrothermal synthesis of ZnFe<sub>2</sub>O<sub>4</sub> ultrafine particles with high magnetization," *Journal of Magnetism and Magnetic Materials*, vol. 256, pp. 420–424, 2003.
- [4] F. F. Powders, "Ferrite Fine Powders," *IEEE TRANSACTIONS ON MAGNETICS*, vol. 31, no. 6, pp. 3808–3810, 1995.
- [5] M. Tadić, D. Marković, V. Spasojević, V. Kusigerski, M. Remškar, J. Pirnat, and Z. Jagličić, "Synthesis and magnetic properties of concentrated  $\alpha$ -Fe<sub>2</sub>O<sub>3</sub> nanoparticles in a silica matrix," *Journal of Alloys and Compounds*, vol. 441, no. 1–2, pp. 291–296, Aug. 2007.
- [6] I. H. Gul, W. Ahmed, and a. Maqsood, "Electrical and magnetic characterization of nanocrystalline Ni–Zn ferrite synthesis by co-precipitation route," *Journal of Magnetism and Magnetic Materials*, vol. 320, no. 3–4, pp. 270–275, Feb. 2008.
- [7] Y. Cedeño-Mattei and O. Perales-Pérez, "Synthesis of high-coercivity cobalt ferrite nanocrystals," *Microelectronics Journal*, vol. 40, no. 4–5, pp. 673–676, Apr. 2009.
- [8] S. Gubbala, H. Nathani, K. Koizol, and R. D. K. Misra, "Magnetic properties of nanocrystalline Ni–Zn, Zn–Mn, and Ni–Mn ferrites synthesized by reverse micelle technique," *Physica B: Condensed Matter*, vol. 348, no. 1–4, pp. 317–328, May 2004.
- [9] R. D. K. Misra, S. Gubbala, a. Kale, and W. F. Egelhoff, "A comparison of the magnetic characteristics of nanocrystalline nickel, zinc, and manganese ferrites synthesized by reverse micelle technique," *Materials Science and Engineering: B*, vol. 111, no. 2–3, pp. 164–174, Aug. 2004.
- [10] a. Kale, S. Gubbala, and R. D. K. Misra, "Magnetic behavior of nanocrystalline nickel ferrite synthesized by the reverse micelle technique," *Journal of Magnetism and Magnetic Materials*, vol. 277, no. 3, pp. 350–358, Jun. 2004.
- [11] K. H. Wu, Y. C. Chang, and G. P. Wang, "Preparation of NiZn ferrite/SiO<sub>2</sub> nanocomposite powders by sol-gel auto-combustion method," *Journal of Magnetism and Magnetic Materials*, vol. 269, no. 2, pp. 150–155, Feb. 2004.

- [12] M. Sinha, H. Dutta, and S. K. Pradhan, "X-ray characterization and phase transformation kinetics of ball-mill prepared nanocrystalline Mg–Zn-ferrite at elevated temperatures," *Physica E: Low-dimensional Systems and Nanostructures*, vol. 33, no. 2, pp. 367–369, Jul. 2006.
- [13] V. Berbenni, C. Milanese, G. Bruni, a. Marini, and I. Pallecchi, "Synthesis and magnetic properties of ZnFe<sub>2</sub>O<sub>4</sub> obtained by mechanochemically assisted low-temperature annealing of mixtures of Zn and Fe oxalates," *Thermochimica Acta*, vol. 447, no. 2, pp. 184–189, Aug. 2006.
- [14] D. Singh, C. Suryanarayana, L. Mertus, and R.-H. Chen, "Extended homogeneity range of intermetallic phases in mechanically alloyed Mg–Al alloys," *Intermetallics*, vol. 11, no. 4, pp. 373–376, Apr. 2003.
- [15] R. Perez Moyet, Y. Cardona, P. Vargas, J. Silva, and O. N. C. Uwakweh, "Coercivity and superparamagnetic evolution of high energy ball milled (HEBM) bulk CoFe<sub>2</sub>O<sub>4</sub> material," *Materials Characterization*, vol. 61, no. 12, pp. 1317–1325, Dec. 2010.
- [16] F. Grasset, N. Labhsetwar, D. Li, D. C. Park, N. Saito, H. Haneda, O. Cador, T. Roisnel, S. Mornet, E. Duguet, J. Portier, and J. Etourneau, "Synthesis and Magnetic Characterization of Zinc Ferrite Nanoparticles with Different Environments: Powder, Colloidal Solution, and Zinc Ferrite–Silica Core–Shell Nanoparticles," *Langmuir*, vol. 18, no. 21, pp. 8209–8216, Oct. 2002.
- [17] P. M. Botta, P. G. Bercoff, E. F. Aglietti, H. R. Bertorello, and J. M. Porto López, "Synthesis and magnetic properties of zinc ferrite from mechanochemical and thermal treatments of Zn–Fe<sub>3</sub>O<sub>4</sub> mixtures," *Materials Science and Engineering: A*, vol. 360, no. 1–2, pp. 146–152, Nov. 2003.
- [18] M. Grigorova, H. J. Blythe, V. Blaskov, V. Rusanov, V. Petkov, V. Masheva, D. Nihtianova, L. M. Martinez, J. S. Mun, and M. Mikhov, "Magnetic properties and Mössbauer spectra of nanosized CoFe<sub>2</sub>O<sub>4</sub> powders," *Journal of Magnetism and Magnetic Materials*, vol. 183, pp. 163–172, 1998.
- [19] M. Sorescu, L. Diamandescu, R. Peelamedu, R. Roy, and P. Yadoji, "Structural and magnetic properties of NiZn ferrites prepared by microwave sintering," *Journal of Magnetism and Magnetic Materials*, vol. 279, pp. 195–201, 2004.
- [20] O. N. C. Uwakweh, R. P. Moyet, R. Mas, C. Morales, P. Vargas, J. Silva, Á. Rossa, and N. López, "Mössbauer spectroscopy study of the synthesis of SnFe<sub>2</sub>O<sub>4</sub> by high energy ball milling (HEBM) of SnO and  $\alpha$ -Fe<sub>2</sub>O<sub>3</sub>," pp. 4–8.
- [21] S. Bid and S. K. Pradhan, "Preparation of zinc ferrite by high-energy ball-milling and microstructure characterization by Rietveld's analysis," *Materials Chemistry and Physics*, vol. 82, no. 1, pp. 27–37, Sep. 2003.

- [22] H. Dutta, M. Sinha, Y. C. Lee, and S. K. Pradhan, "Microstructure characterization and phase transformation kinetics of ball-mill prepared nanocrystalline Mg–Zn-ferrite by Rietveld's analysis and electron microscopy," *Materials Chemistry and Physics*, vol. 105, no. 1, pp. 31–37, Sep. 2007.
- [23] M. Sinha and S. K. Pradhan, "Synthesis of nanocrystalline Cd–Zn ferrite by ball milling and its stability at elevated temperatures," *Journal of Alloys and Compounds*, vol. 489, no. 1, pp. 91–98, Jan. 2010.
- [24] S. Ozcan, B. Kaynar, M. M. Can, and T. Firat, "Synthesis of ZnFe<sub>2</sub>O<sub>4</sub> from metallic zinc and iron by wet-milling process," *Materials Science and Engineering: B*, vol. 121, no. 3, pp. 278–281, Aug. 2005.
- [25] T. Verdier, V. Nivoix, M. Jean, and B. Hannoyer, "Characterization of nanocrystalline Mn-Zn ferrites obtained by mechanosynthesis," *Journal of Materials Science*, vol. 39, no. 16/17, pp. 5151–5154, Aug. 2004.
- [26] T. Verdier, V. Nachbaur, and M. Jean, "Mechanosynthesis of zinc ferrite in hardened steel vials: Influence of ZnO on the appearance of Fe(II)," *Journal of Solid State Chemistry*, vol. 178, no. 11, pp. 3243–3250, Nov. 2005.
- [27] V. Nachbaur, G. Tauvel, T. Verdier, M. Jean, J. Juraszek, and D. Houvet, "Mechanosynthesis of partially inverted zinc ferrite," *Journal of Alloys and Compounds*, vol. 473, no. 1–2, pp. 303–307, Apr. 2009.
- [28] M. Jean and V. Nachbaur, "Determination of milling parameters to obtain mechanosynthesized ZnFe<sub>2</sub>O<sub>4</sub>," *Journal of Alloys and Compounds*, vol. 454, no. 1–2, pp. 432–436, Apr. 2008.
- [29] C. Suryanarayana, "Mechanical alloying and milling," *Progress in Materials Science*, vol. 46, pp. 1–184, 2001.
- [30] H. Yang, X. Zhang, C. Huang, W. Yang, and G. Qiu, "Synthesis of ZnFe<sub>2</sub>O<sub>4</sub> nanocrystallites by mechanochemical reaction," *Journal of Physics and Chemistry of Solids*, vol. 65, no. 7, pp. 1329–1332, Jul. 2004.
- [31] Y. Ahn, E. J. Choi, and S. Kim, "Magnetization and Mossbauer Study of Nanosize ZnFe<sub>2</sub>O<sub>4</sub> Particles Synthesized by Using a Microemulsion Method," *Journal of Korean Physica Society*, vol. 41, no. 1, pp. 0–5, 2002.
- [32] D. S. Mathew and R.-S. Juang, "An overview of the structure and magnetism of spinel ferrite nanoparticles and their synthesis in microemulsions," *Chemical Engineering Journal*, vol. 129, no. 1–3, pp. 51–65, May 2007.
- [33] D. V. Perepelitsa, "Mossbauer Spectroscopy of," vol. 0, no. 4, pp. 0–3, 2007.

- [34] R. . Mossbauer, “Recoilless nuclear resonance absorption of gamma radiation,” 1961.
- [35] R. A. Schumacher, “Mossbauer spectroscopy,” 2011.
- [36] C. N. Chinnasamy, A. Narayanasamy, N. Ponpandian, and K. Chattopadhyay, “The influence of Fe 3 + ions at tetrahedral sites on the magnetic properties of nanocrystalline ZnFe 2 O 4,” *Materials Science and Engineering: A*, vol. 306, pp. 983–987, 2001.
- [37] H. Ehrhardt, S. J. Campbell, and M. Hofmann, “Structural evolution of ball-milled ZnFe 2 O 4,” *Journal of Alloys and Compounds*, vol. 339, pp. 255–260, 2002.
- [38] K. Tanaka, M. Makita, Y. Shimizugawa, K. Hirao, and N. Soga, “Structure and High Magnetization of Rapidly Quenched Zinc Ferrite,” *Journal of Physics and Chemistry of Solids*, vol. 59, no. 9, pp. 1611–1618, Sep. 1998.
- [39] S. Bid and S. . Pradhan, “M,” *Materials Chemistry and Physics*, vol. 84, no. 2–3, pp. 291–301, Apr. 2004.
- [40] I. Chicinas, “Soft magnetic nanocrystalline powders produced by mechanical alloying routes,” vol. 8, no. 2, pp. 439–448, 2006.
- [41] S. Bid, A. Banerjee, S. Kumar, S. K. Pradhan, U. De, and D. Banerjee, “Nanophase iron oxides by ball-mill grinding and their Mossbauer characterization,” *Journal of Alloys and Compounds*, vol. 326, pp. 292–297, 2001.
- [42] L.-L. Wang and J.-S. Jiang, “Preparation of  $\alpha$ -Fe<sub>2</sub>O<sub>3</sub> nanoparticles by high-energy ball milling,” *Physica B: Condensed Matter*, vol. 390, no. 1–2, pp. 23–27, Mar. 2007.
- [43] M. Mozaffari, M. Gheisari, M. Niyafar, and J. Amighian, “Magnetic properties of mechanochemically prepared iron–wüstite (Fe–Fe<sub>3</sub>O<sub>4</sub>) nanocomposites,” *Journal of Magnetism and Magnetic Materials*, vol. 321, no. 19, pp. 2981–2984, Oct. 2009.
- [44] M. Muhammed and T. Tsakalakos, “Nanostructured Materials and Nanotechnology : Overview,” *Journal of Korean Ceramic Society*, vol. 40, no. 11, pp. 1027–1046, 2003.
- [45] B. G. . and H. H. . Bukrey R.R, Keneally P.F, “Mossbauer-effect study of the structure and magnetic properties of Na<sub>2</sub>O-Li<sub>2</sub>O-B<sub>2</sub>O<sub>3</sub>-Fe<sub>3</sub>O<sub>3</sub> glass system,” *Physical Review B*, vol. 9, pp. 1052–1061, 1974.
- [46] I. U. Heilmann, N. B. Olsen, and J. Staun, “Electron Hopping and Temperature Dependent Oxidation States of Iron in Ilvaite Studied by Mossbauer Effect,” vol. 285, 1977.
- [47] B. Ellis, L. K. Perry, D. H. Ryan, and L. F. Nazar, “Small polaron hopping in Li(x)FePO<sub>4</sub> solid solutions: coupled lithium-ion and electron mobility.,” *Journal of the American Chemical Society*, vol. 128, no. 35, pp. 11416–22, Sep. 2006.

- [48] Y. Ahn, E. J. Choi, and E. H. Kim, "SUPERPARAMAGNETIC RELAXATION IN COBALT FERRITE NANOPARTICLES SYNTHESIZED FROM HYDROXIDE CARBONATE PRECURSORS," *Rev. Adv.Mater.Sci.*, pp. 477–480, 2003.
- [49] Y. Ahn, E. Jung, S. Kim, and H. Nam, "Magnetization and Mossbauer study of cobalt ferrite particles," *Materials Letters*, no. August, pp. 47–52, 2001.
- [50] C. Liu, B. Zou, A. J. Rondinone, and Z. J. Zhang, "Chemical Control of Superparamagnetic Properties of Magnesium and Cobalt Spinel Ferrite Nanoparticles through Atomic Level Magnetic Couplings," *Journal of the American Chemical Society*, vol. 122, no. 26, pp. 6263–6267, Jul. 2000.
- [51] M. Jalaly, M. H. Enayati, F. Karimzadeh, and P. Kameli, "Mechanosynthesis of nanostructured magnetic Ni–Zn ferrite," *Powder Technology*, vol. 193, no. 2, pp. 150–153, Jul. 2009.
- [52] S. Thakur, S. C. Katyal, and M. Singh, "Structural and magnetic properties of nano nickel–zinc ferrite synthesized by reverse micelle technique," *Journal of Magnetism and Magnetic Materials*, vol. 321, no. 1, pp. 1–7, Jan. 2009.
- [53] D. R. Sharma, R. Mathur, S. R. Vadera, and N. Kumar, "Synthesis of nanocomposites of Ni–Zn ferrite in aniline formaldehyde copolymer and studies on their pyrolysis products," *Journal of Alloys and Compounds*, vol. 358, pp. 193–204, 2003.
- [54] A. Kundu, C. Upadhyay, and H. C. Verma, "Magnetic properties of a partially inverted zinc ferrite synthesized by a new coprecipitation technique using urea," *Physics Letters A*, vol. 311, no. 4–5, pp. 410–415, May 2003.
- [55] R. S. Devan, Y. D. Kolekar, and B. K. Chougule, "Effect of cobalt substitution on the properties of nickel–copper ferrite," *Journal of Physics: Condensed Matter*, vol. 18, no. 43, pp. 9809–9821, Nov. 2006.
- [56] P. Kumar, P. Mishra, and S. K. Sahu, "Synthesis of Ni-Zn Ferrites Using Low Temperature Sol-Gel Process," *International Journal of Scientific & Engineering Research*, vol. 2, no. 8, pp. 8–11, 2011.
- [57] M. Menzel, V. Sepelak, and K. D. Becker, "Mechanochemical reduction of nickel ferrite," pp. 663–669, 2001.
- [58] D. Sepelak V, Baabe, D. Mienert, D. Schultze, F. Krumeich, F. J. Litterst, and K. D. Becker, "Evolution of structure and magnetic properties with annealing temperature in nanoscale high-energy-milled nickel ferrite," *Journal of Magnetism and Magnetic Materials*, vol. 257, pp. 377–386, 2003.
- [59] K. D. Becker and V. Sepelak, "Mossbauer Studies in the Mechanochemistry of Spinel Ferrites," *Journal of Materials Synthesis and Processing*, vol. 8, pp. 155–166, 2000.

- [60] I. Sepelak V, Bergmann, A. Feldhoff, P. Heitjans, F. Krumeich, D. Menzel, F. J. Litterst, S. J. Campbell, and K. D. Becker, "Nanocrystalline Nickel Ferrite , NiFe<sub>2</sub>O<sub>4</sub> : Mechanosynthesis , Nonequilibrium Cation Distribution , Canted Spin Arrangement , and Magnetic Behavior," *J. Phys. Chem. C*, pp. 5026–5033, 2007.
- [61] A. S. D. Albuquerque, J. D. Ardisson, E. Bittencourt, and W. A. D. A. Macedo, "Structure and magnetic properties of granular NiZn-ferrite - SiO<sub>2</sub>," *Materials Research*, vol. 2, no. 3, pp. 235–238, Jul. 1999.
- [62] P. I. G. Molnar, Z. Homonnay, A. Vertes, J. Borossay, B. Serrano, "È ssbauer spectroscopic and optical study of iron incorporation Mo into alumina powders," *Journal of Physics and Chemistry of Solids*, vol. 62, pp. 619–625, 2001.
- [63] E. Manova, D. Paneva, B. Kunev, E. Rivière, C. Estournès, and I. Mitov, "Characterization of nanodimensional Ni-Zn ferrite prepared by mechanochemical and thermal methods," *Journal of Physics: Conference Series*, vol. 217, p. 012102, Mar. 2010.
- [64] Jiles D., Introduction to magnetism and magnetic materials, First edition, Chapman & Hall, London (1991)
- [65] Kittel C., Introduction to solid state physics, 8<sup>th</sup> Edition, John Wiley & Song, Inc. US 2005.
- [66] Myers H.P, Introductory solid state physics. 2th Edition , CRC Press, London, 1997.
- [67] Gruverman I.J., Mössbauer effect methodology, Vol. 1: Proceedings of the First symposium on Mössbauer effect methodology. Plenum Press, New York, 1965.
- [68] Gruverman I.J., Mössbauer effect methodology, Vol. 2: Proceedings of the Second symposium on Mössbauer effect methodology. Plenum Press, New York, 1966.
- [69] Gruverman I.J, Mössbauer effect methodology, Vol.3: Proceedings of the Third symposium on Mössbauer effect methodology. Plenum Press, New York, 1967.
- [70] Gruverman, Mössbauer effect methodology, Vol.4: Proceedings of the Fourth symposium on Mössbauer effect methodology. Plenum Press, New York, 1968.
- [71] J.C. Anderson, Magnetism and Magnetic Materials, First Edition, Chapman & Hall LTD, London, 1968.
- [72] Lifshin E., X-ray Characterization of Materials, First edition, WILEY-VCH Verlag GmbH, Weinheim (Federal Republic of Germany), 1999.
- [73] Cullity B.D, and Graham C.D. , Introduction to magnetic materials, Second edition, Wiley, New Jersey, 2009.

- [74] Cullity B.D., Elements of X-ray Diffraction, Second edition, Addison-Wesley metallurgical series, Massachusetts, 1956.
- [75] C. Seidel, "The Mossbauer Effect and Its Application in Chemistry", American Chemical Society publications, Washington, 1967.
- [76] Gunser E., Mössbauer Spectroscopy, Spring -Verlag, New York, 1975
- [77] Gruverman I.J, Mössbauer effect methodology, Voll: Proceedings of the Second symposium on Mössbauer effect methodology. Plenum Press, New York, 1966.
- [78] Chikazumi S., Physic of Ferromagnetism, Second edition, Oxford science publications, New York, 1997.
- [79] Gusev A., and Rempel A, Nanocrystalline materials, CISP, Chippenham, Great Britain, 2004.
- [80] Hook & Hall, Solid State Physics, second edition, 1991
- [81] Urcia S., "Synthesis and study of structural and magnetic properties of ferrite nanocrystals for magnetocaloric applications" Master Thesis, University of Puerto Rico, Mayaguez campus, 2011.
- [82] Msomi J. et al. "Heat treatment effects on spinel phase of  $Zn_xNi_{1-x}Fe_2O_4$  and  $MnFe_2O_4$  nanoferrites. Hyperfine Interact. Springer 2010.
- [83] Perez, R. "Study of properties enhancement of Magnesium Diboride ( $MgB_2$ ) by Ta  $B_2$  doping via High Energy Ball Milling" Master Thesis, University of Puerto Rico, Mayaguez campus, 2008.
- [84] O' Handley R., Modern magnetic materials: principles and applications, John Wiley & Sons, New York, 1999.
- [85] Song Q, "Size and shape controlled synthesis and superparamagnetic properties of spinel ferrites nanocrystals", Doctoral Thesis, Georgia Institute of technology, 2005.
- [86] Toledo-Antonio et al., "Correlation between the magnetism of non-stoichiometric Zinc ferrites and their catalytic activity for oxidative dehydrogenation of 1-butene", Applied Catalysis A: General 234 (2002)
- [87] Valenzuela R., "Novel Applications of Ferrites", Physics Research International Volume 2012

- [88] Scherer and Figuereido, “Ferrofluids: Properties and Applications”, Brazilian journal of physics, 2005
- [89] Cedeño-Matei., “Composition-structure and size/shape-controlled synthesis and characterization of high coercivity ferrite nanocrystals” Doctoral Thesis, University of Puerto Rico, Mayaguez campus, 2010.